

Investigation of Protonation Dynamics-Related
Processes in Light-Absorbing and Converting
Proteins by NMR

Inaugural-Dissertation

to obtain the academic degree

Doctor rerum naturalium (Dr. rer. Nat.)

Submitted to the department Biology, Chemistry, Pharmacy
of Freie Universität Berlin

by

Lisa Maria Gerland

Berlin 2022

1st reviewer: Prof. Dr. Hartmut Oschkinat

2nd reviewer: Prof. Markus Wahl, PhD

Date of Disputation: 06.04.2023

The presented work was performed from November 2017 until November 2022 in the ‘Department of NMR-supported structural Biology’ and supervised by Prof. Dr. Hartmut Oschkinat at the *Leibniz-Forschungsinstitut für Molekulare Pharmakologie (FMP)* in Berlin, Germany

Acknowledgements

I would like to thank everybody involved in this work. First of all, I thank Hartmut Oschkinat for giving me the opportunity to become part of his group and trusting me with the two projects I worked on. I enjoyed the scientific cooperation with your group, the fruitful discussions we had and the way you take care of your students after the PhD.

I thank Markus Wahl for reviewing this thesis, and Barth-Jan van Rossum and Dallas Bell for proof-reading it. I want to thank Anne Diehl, Kristina Rehbein, Martina Leidert, Natalja Erdmann and Nils Cremer for all the help in the lab and providing me with samples. A special thanks goes to Stephanie Wendt, who helped me with a dozen broken caps and manufacturing all the filling tools for the group. Andrea Steuer, thanks for dealing with all the administrative work, keeping the coffee machine alive and ready to lend an ear. Thank you, Daniel Friedrich, for being encouraging and teaching me a lot at the spectrometer in the very beginning of my PhD. Thank you, Miguel Arbesú Andrés, for sharing DNP knowledge and maintenance duty at the spectrometer as well as for being a kind and caring person. Thank you, Florian Lindemann, for 5 years of continuous computer assistance, mental support before talks and all the lunch and coffee breaks spent together. Being part of your tipp-kick team was awesome. Thank you, Matthias Herrera-Glomm, for all the help at the spectrometer and DNP-setup, this project would not have worked without you. I want to thank all members of the group for the wonderful lunch break discussions we had: Arndt Wallmann, Andy Niewkoop, Barth-Jan van Rossum, Linus Hopf, Johanna Münkemer, Kelsey Collier, Michel Geiger, Nestor Kamden and Wing Ying Chow it was a pleasure meeting all of you! And finally, I want to thank my family, especially Tayfun, for being supportive and caring throughout my time at FMP.

Declaration / Eidesstattliche Erklärung

I hereby declare that I have written this thesis on my own, marked the sources of any quotations or content obtained otherwise and mentioned any other personal help by name. I also declare that I have not submitted the dissertation in this or any other form to any other institution as a dissertation.

Hierdurch versichere ich, dass ich meine Dissertation selbstständig verfasst und keine anderen als die von mir angegebenen Quellen und Hilfsmittel verwendet habe. Die Dissertation ist in keinem früheren Promotionsverfahren angenommen oder abgelehnt worden.

Lisa Gerland

Summary

Nuclear magnetic resonance spectroscopy (NMR) is a versatile tool for simultaneously studying structure and dynamics of biological systems. Solution and solid-state NMR complement each other, being applicable to small proteins or large assemblies. Exploiting the dual nature of the NMR information by monitoring changes in structure and dynamics is beneficial for understanding functional aspects of biological systems. One way to induce structural changes in proteins is through alterations of the protonation state, a principle which is referred to as ‘protonation dynamics’. The two proteins investigated in this work, PsbO and Cph1, are both involved in processes attributed to protonation dynamics, and are studied by solution and solid-state NMR.

Photosynthesis produces highly reactive compounds, whose concentrations must be strictly monitored and regulated. At the oxygen evolving centre (OEC) of photosystem II (PSII) - a multiprotein complex spanning the thylakoid membrane - the water-splitting reaction takes place and generates a high proton concentration at the proton release site. PsbO, being in close proximity to the OEC and bearing a significant number of surface carboxyl groups, is likely involved in proton storage or translocation to the lumen. This work investigates the protonation state of the surface aspartic and glutamic acid side chain carboxyl groups of the beta-barrel of PsbO to provide information about a possible proton transfer pathway.

Solution NMR experiments were employed to assign the protein backbone NMR signals as well as glutamic and aspartic acid side chain carbon resonances. pK_a values of 21 carboxylate groups, of which 9 are aspartate and 12 glutamate residues, were determined by the application of 2D titration experiments. The determined pK_a values were plotted onto the crystal structure, resulting in an uneven distribution with values below 3.5 clustered on the side of the protein

facing PSII whereas values around 4.9 were located at the luminal side of PsbO. The protein backbone stability was monitored throughout the pH titration by HSQC experiments. Loop regions, exposed to the thylakoid lumen, showed pH dependent backbone chemical shift changes which is an indication for conformational changes in this region. This study shows that the bilateral surface pK_a distribution enables PsbO to serve as a luminal buffer and potential acceptor of protons, generated during PSII activity.

Phytochromes are red and far-red light sensing photoreceptors, present in plants, fungi, and cyanobacteria that control developmental processes such as seed germination and flowering. Phytochromes are activated by far-red light that is able to penetrate tissues, which makes them promising tools for optogenetics. It is essential to specify concomitant structural rearrangements in the protein to understand how the signal is transduced from the light-sensitive chromophore to the histidine-kinase output domain. Here, sedimentation NMR (sedNMR) and dynamic nuclear polarization (DNP) were combined at high field (800 MHz) to study the so-called ‘tongue’ region of the cyanobacterial phytochrome Cph1Δ2, a structural element conserved in all phytochromes. This element is supposed to change its secondary structure from beta-sheet to alpha-helix upon light irradiation, yet this effect has so far only been observed in different types of proteins, bathy and canonical phytochromes. Here, we want to observe the transition in one protein by studying and comparing Cph1Δ2 in the Pr and Pfr state. In addition, the phycocyanobilin (PCB) chromophore was examined for chemical exchange in its binding pocket.

No indication of line broadening due to chemical exchange at the methine carbon signals of PCB was observed in a temperature series. The application of DNP at high fields is not trivial, since enhancements decline and standard measurement conditions can lead to partial unfolding of the proteins investigated. For this

reason, new buffer conditions were tested and two polarizing agents, bctol-M and M-TinyPol, were characterized and compared. The performance of bcTol-M was convincing, showing a similar enhancement but higher stability than M-TinyPol. A reduced glycerol concentration, 10 % (v/v) compared to 60 % used in the standard DNP buffers, was applied without significant loss of enhancement. The combination of a selective amino acid labelling scheme and pulse sequence filtering led to reduced spectral overlap, enabling the assignment of resonances within the 58 kDa cyanobacterial phytochrome Cph1 Δ 2 at DNP measurement conditions. By the comparison of 3D hCaNCOCa spectra, recorded on Pr and Pfr state Cph1 Δ 2, a strong indication for structural rearrangements within the ‘tongue’ region was found. In particular, signals with α -helical shift pattern were appearing after the conversion of Cph1 Δ 2 into the Pfr state. For the first time, changes in this region were observed within a single sample of a cyanobacterial phytochrome.

Zusammenfassung

Die Kernspinresonanzspektroskopie (NMR) bietet die Möglichkeit, gleichzeitig Struktur und Dynamik biologischer Systeme zu untersuchen. Um funktionelle Aspekte biologischer Systeme zu verstehen, ist vorteilhaft diese Dualität der NMR-Information auszunutzen. Hierbei ergänzen sich Lösungs- und Festkörper-NMR, da in Lösungs-NMR hauptsächlich Proteine mit geringem Molekulargewicht und in der Festkörper-NMR vor allem größere Molekülkomplexe untersucht werden. Eine Art, Strukturänderungen in einem Protein hervorzurufen, ist durch die Veränderung seines Protonierungszustands, ein Prinzip das unter den Begriff ‚Protonierungsdynamik‘ fällt. Die zwei in dieser Arbeit untersuchten Proteine, PsbO und Cph1, sind beide an Prozessen beteiligt, die der Protonierungsdynamik zugeschrieben werden. Sie werden mittels Lösungs- und Festkörper-NMR untersucht.

Bei der Photosynthese entstehen hochreaktive Verbindungen, deren Konzentrationen streng überwacht und reguliert werden müssen. Am sauerstoffproduzierenden Komplex (OEC) des Photosystems II (PSII) – einem Multiproteinkomplex, der die Thylakoidmembran durchzieht – findet die Wasserspaltungsreaktion statt. Das führt zu einer erhöhten Protonenkonzentration am Ort der Protonenfreisetzung. PsbO befindet sich in unmittelbarer Nähe des OEC und trägt eine beträchtliche Anzahl an Oberflächencarboxylgruppen. Es ist daher wahrscheinlich, dass PsbO als Protonenspeicher dient oder an dem Transport der Protonen ins Thylakoidlumen beteiligt ist. In dieser Arbeit wurde der Protonierungszustand der Asparaginsäure- und Glutaminsäure-Seitenkettencarboxylgruppen von PsbO untersucht um Informationen über einen möglichen Protonentransferweg zu erhalten. Lösungs-NMR Experimente wurden verwendet, um die NMR Signale des Proteinrückgrats sowie die Kohlenstoffresonanzen der Glutaminsäure- und

Asparaginsäure-Seitenketten zuzuordnen. pK_s – Werte von 21 Carboxylatgruppen, darunter 9 Aspartat- und 12 Glutamatreste, konnten durch 2D-Titrationsexperimente bestimmt werden. Die ermittelten pK_s – Werte wurden auf die Kristallstruktur von PsbO übertragen, wobei sich eine ungleichmäßige Verteilung ergab. Auf der, dem PSII zugewandten Seite des Proteins, nehmen die Carboxylatgruppen pK_s – Werte unter 3,5 an, wohingegen auf der luminalen Seite pK_s – Werte um 4,9 beobachtet wurden. Die Stabilität des Proteinrückgrats wurde während der gesamten pH-Titration durch HSQC Experimente überwacht. Unstrukturierte Bereiche, sogenannte ‚Loop-Regionen‘, die in das Thylakoidlumen reichen, zeigten pH-abhängige Änderungen der chemischen Verschiebung, was ein Hinweis auf Konformationsänderungen in dieser Region ist. Mit dieser Studie konnte gezeigt werden, dass die zweiseitige Verteilung von pK_s – Werten auf der Oberfläche von PsbO dazu führt, dass das Protein als luminaler Puffer fungieren kann und ein potenzieller Akzeptor von Protonen ist, die während der PSII-Aktivität entstehen.

Phytochrome sind Photorezeptoren, die Licht aus dem roten und infraroten Bereich wahrnehmen. Sie kommen in Pflanzen, Pilzen und Cyanobakterien vor und steuern Entwicklungsprozesse wie Samenkeimung und Blüte. Da Phytochrome durch Infrarotlicht aktiviert werden können, welches in der Lage ist Gewebe zu durchdringen, sind sie vielversprechende Werkzeuge für die Optogenetik. Um zu verstehen, wie das Signal vom lichtempfindlichen Chromophor zur Histidinkinase-Domäne weitergeleitet wird, hilft es strukturelle Veränderungen im Protein zu untersuchen, die während der Signalweitergabe auftreten. In dieser Arbeit wurden Sedimentations-NMR (sedNMR) und dynamische Kernspinpolarisation (DNP) bei hohen Magnetfeldstärken (800 MHz) kombiniert um die sogenannte ‚Zungen‘-Region des cyanobakteriellen Phytochroms Cph1Δ2 zu untersuchen, ein Strukturelement welches in allen

Phytochromen konserviert ist. Es wird angenommen, dass dieses Element bei Lichteinstrahlung seine Sekundärstruktur von einem β -Faltblatt zu einer α -Helix ändert. Dieser Effekt konnte allerdings nur in verschiedenen Typen von Phytochromen gezeigt werden, Bathy-Phytochrome zeigen eine α -Helix im Pfr Zustand und kanonische Phytochrome ein β -Faltblatt im Pr Zustand. In dieser Arbeit soll die Strukturänderung in einem einzigen Protein beobachtet werden, indem Cph1 Δ 2 im Pfr und Pr Zustand untersucht und verglichen wird. Darüber hinaus wird der Chromophor Phycocyanobilin (PCB) in seiner Bindungstasche hinsichtlich eines chemischen Austausches untersucht. In einer Temperaturmessreihe konnte keine Linienverbreiterung aufgrund eines chemischen Austausches an den Methin-Kohlenstoff-Signalen von PCB beobachtet werden. Der Einsatz von DNP bei hohen Feldstärken ist nicht trivial, da die Signalverstärkung im Vergleich zu geringeren Magnetfeldern reduziert ist, außerdem kommt es unter den Standardmessbedingungen zur teilweisen Entfaltung der zu untersuchenden Proteine. Aus diesem Grund wurden neue Pufferbedingungen getestet und zwei Radikale, bcTol-M und M-TinyPol, charakterisiert und verglichen. bcTol zeigte eine ähnliche Signalverstärkung wie M-TinyPol, aber eine höhere Stabilität. Die Glycerinkonzentration im DNP-Puffer konnte, ohne eine merkliche Reduzierung der Signalverstärkung, von 60 % (v/v) auf 10 % verringert werden. Durch die Kombination eines spezifischen Aminosäuremarkierungsmusters mit einer selektiven Pulssequenz konnte die Überlappung von Signalen verringert werden. Dadurch wurde die Zuordnung von Resonanzen des 58 kDa cyanobakteriellen Phytochroms Cph1 Δ 2 unter DNP Messbedingungen ermöglicht. Der Vergleich von 3D hCaNCOCa Spektren, aufgenommen von Cph1 Δ 2 im Pr und Pfr Zustand, deutete auf strukturelle Umlagerungen im Bereich der ‚Zungen‘-Region hin. Genauer gesagt traten nach der Beleuchtung des Proteins Signale mit chemischen Verschiebungen im α -

helikalen Bereich auf, die dieser Region zugeordnet wurden. In dieser Arbeit konnten Strukturänderungen in der ‚Zungen‘-Region zum ersten Mal innerhalb einer einzigen Probe eines cyanobakteriellen Phytochroms beobachtet werden.

Table of Contents

ACKNOWLEDGEMENTS	IV
DECLARATION / EIDESSTATTLICHE ERKLÄRUNG	VI
SUMMARY	VIII
ZUSAMMENFASSUNG	XI
TABLE OF CONTENTS	XV
LIST OF ABBREVIATIONS	XVII
LIST OF FIGURES	XIX
LIST OF TABLES	XX
<u>1 GENERAL INTRODUCTION</u>	<u>1</u>
1.1 BIOPHYSICAL CONCEPTS	2
1.1.1 BASIC PRINCIPLES OF (SOLID STATE) NMR	2
1.1.2 DYNAMIC NUCLEAR POLARISATION	13
1.1.3 SEDIMENTATION NMR	21
1.1.4 CHEMICAL EXCHANGE AND 1D NMR SPECTROSCOPY	24
1.1.5 PRINCIPLES OF pK_a TITRATION IN NMR	26
1.1.6 CONCEPTIONAL IDEA OF PROTONATION DYNAMICS IN PROTEINS	29
1.2 BIOLOGICAL SYSTEMS	31
1.2.1 PSBO: A PHOTOSYSTEM II ASSOCIATED PROTEIN INVOLVED IN PROTON TRANSPORT	31
1.2.2 ANALYSING LIGHT-INDUCED MOLECULAR CHANGES IN PHYTOCHROME CPH1 Δ 2	36
1.3 OBJECTIVE AND SCOPE OF THE THESIS	41
<u>2 MATERIAL AND METHODS</u>	<u>44</u>
2.1 SOLUTION NMR OF PsBO	45
2.1.1 PROTEIN EXPRESSION, PURIFICATION AND SAMPLE PREPARATION	45
2.1.2 RECORDING OF ASSIGNMENT AND pK_a TITRATION SPECTRA	46
2.1.3 PROPKA PREDICTION TOOL	47
2.1.4 CALCULATION OF CHEMICAL SHIFT PERTURBATIONS (CSP)	48
2.2 SOLID STATE AND DNP EXPERIMENTS OF PHYTOCHROME CPH1Δ2	48
2.2.1 EXPRESSION AND PURIFICATION OF SELECTIVELY LABELLED CPH1 Δ 2 PHYTOCHROME	48
2.2.2 PREPARATION OF PROLINE STANDARD AND RADICAL ROTORS	50

2.2.3	PREPARATION OF PR/PFR-STATE CPH1Δ2 ROTORS	50
2.2.4	ACQUISITION OF DNP SPECTRA	51
2.2.5	CHARACTERIZATION OF BCTOL-M AND M-TINYPOL AT 18.8 T	51
2.2.6	ACQUISITION OF DNP ASSIGNMENT SPECTRA	53
2.2.7	ACQUISITION OF DQ-SQ SPECTRA	56
2.2.8	ACQUISITION OF 1D HC-CP AND 2D CC-DARR SPECTRA FOR TEMPERATURE COMPARISON	57
3	RESULTS AND DISCUSSION	58
3.1	CHARACTERIZATION OF PSBO SURFACE PROTONATION BY SOLUTION NMR	59
3.1.1	ASSIGNMENT OF BACKBONE AND SIDECHAIN RESIDUES	59
3.1.2	PK _a VALUES OF GLUTAMIC AND ASPARTIC ACID CARBOXYLATE GROUPS SCATTER WIDELY AROUND THE MODEL VALUES	62
3.1.3	CHEMICAL SHIFT PERTURBATIONS OF BACKBONE AMIDE GROUPS REVEAL FLEXIBILITY IN THE LUMINAL PART OF THE BETA-BARREL	65
3.1.4	PSBO IS EQUIPPED WITH A BUFFERING CAPACITY AROUND PH 5 AND PH- INDUCED STRUCTURAL CHANGES ARE ACCOMPANIED BY SURFACE CHARGE ALTERATIONS	67
3.2.	DEFINING NMR MEASUREMENT CONDITIONS FOR CPH1Δ2	73
3.2.1	PHYCOCYANOBILIN ¹³ C RESONANCES ARE NOT SUBJECT TO CHEMICAL EXCHANGE PROCESSES AT 800 MHZ AND THE APPLICATION OF SEDNMR IS OPTIMAL AT 261 K	74
3.2.2	ENHANCEMENTS OF M-TINYPOL AND BCTOL-M ARE SIMILAR AT 18.801 T	80
3.3	STRUCTURAL TRANSITIONS IN PHYTOCHROMES UPON LIGHT ABSORPTIONS	88
3.3.1	EFFICIENT LABELLING REDUCES PEAK OVERLAP IN CPH1Δ2 SPECTRA	89
3.3.2	SIGNALS WITH A-HELICAL CHEMICAL SHIFT PATTERN ASSIGNED TO THE ‘TONGUE’ IVR TRIPLET ARE PRESENT IN 3D hCANCoca PFR CPH1Δ2	90
4	CONCLUSION AND FUTURE PERSPECTIVES	101
4.1	VERIFICATION OF STRUCTURAL REARRANGEMENTS OF THE ‘TONGUE’ REGION USING A RV-LABELLED CPH1Δ2	102
4.2	CHARACTERIZATION OF PROTONATION DYNAMICS IN THE BINDING-POCKET OF CPH1Δ2	104
	BIBLIOGRAPHY	107
	LIST OF PUBLICATIONS	121

List of Abbreviations

Å	Ångström
ATP	Adenosintriphosphate
BDPA	1,3-bisdiphenylene-2-phenylallyl
Bsh-CP	Band-selective homonuclear cross polarization
CE	Cross effect
CP	Cross polarization
Cph1Δ2	Photosensory module of cyanobacterial phytochrome 1
CW	Continuous wave
DARR	Dipolar assisted rotational resonance
DNP	Dynamic nuclear polarization
DQ	Double Quantum
EPR	Electron paramagnetic resonance
FID	Free induction decay
HFI	Hyperfine interaction
INADEQUATE	Incredible natural abundance DQ transfer experiment
INEPT	Insensitive nuclei enhancement by polarisation transfer
IPTG	Isopropyl β-D-1-thiogalactopyranoside
LT-MAS	Low temperature magic angle spinning unit
NMR	Nuclear magnetic resonance spectroscopy
MAS	Magic angle spinning
mM	Milli-molar
OE	Overhauser effect
PA	Polarizing agent
PCB	Phycocyanobilin
PDB	Protein data bank
pK _a	Protein dissociation constant

PSI	Photosystem I
PSII	Photosystem II
PsbO	Photosystem II bound protein O
rf	Radiofrequency
rpm	Revolutions per minute
SE	Solid effect
SedNMR	Sedimentation NMR
SNR	Signal-to-noise-ratio
SQ	Single quantum
VT	Variable temperature
ZQ	Zero quantum

List of Figures

FIGURE 1: RELATIVE ZEEMAN SPLITTINGS OF PROTON (^1H), CARBON (^{13}C) AND NITROGEN (^{15}N) ISOTOPES ACCORDING TO THEIR GYROMAGNETIC RATIO.....	3
FIGURE 2: SIMPLIFIED DESCRIPTION OF THE GENERATION OF AN NMR SIGNAL USING THE VECTOR MODEL.	5
FIGURE 3: CHEMICAL SHIFT ANISOTROPY, POWDER PATTERN AND MAGIC ANGLE SPINNING.....	8
FIGURE 4: HCC DARR PULSE SEQUENCE.	10
FIGURE 5: L-PROLINE HC-CP SPECTRA.	14
FIGURE 6: DNP SETUP.....	15
FIGURE 7: MESOMERIC STRUCTURES OF BDPA.....	17
FIGURE 8: EPR SPECTRA AND ENHANCEMENT PROFILE OF SOLID EFFECT, CROSS EFFECT AND OVERHAUSER EFFECT MODIFIED AFTER THANKAMONY ET AL.	18
FIGURE 9: COMPARISON OF PROTEIN SEDIMENTATION IN THE ROTOR WITH A MICROCRYSTALLINE PROTEIN PREPARATION.	21
FIGURE 10: THE DIFFERENT SEDIMENTATION APPROACHES IN NMR.....	22
FIGURE 11: PsbO IN PHOTOSYSTEM II DIMER.....	32
FIGURE 12: COMPARISON OF FULL-LENGTH PROTEIN AND THE SHORT CONSTRUCT USED IN OUR STUDIES.	34
FIGURE 13: FEATURES OF CYANOBACTERIAL PHYTOCHROME Cph1.....	37
FIGURE 14: hCANCoca PULSE SEQUENCE.	54
FIGURE 15: SCP5 PULSE SEQUENCE USED FOR THE ACQUISITION OF CARBON DQ-SQ SPECTRA.	56
FIGURE 16: HSQC SPECTRUM OF PsbO-B WITH ASSIGNED NH CORRELATIONS.	59
FIGURE 17: BACKBONE WALK.	60
FIGURE 18: 2D PROJECTION OF THE 3D CbCACo SPECTRUM RECORDED AT PH 6.6.....	61
FIGURE 19: TITRATION EXPERIMENTS AND ANALYSIS.	63
FIGURE 20: SUPERPOSITION OF ^{15}N - ^1H HSQC TITRATION SPECTRA OF PsbO-B RECORDED AT PH VALUES RANGING FROM 7.9 IN DARK BLUE TO 3.1 IN PURPLE.	65
FIGURE 21: CHEMICAL SHIFT PERTURBATIONS OF PsbO BACKBONE AMIDE GROUPS MEASURED BY 2D ^1H - ^{15}N CORRELATION SPECTROSCOPY.	67
FIGURE 22: OVERALL pK_a TITRATION CURVE OF PsbO SHOWS AN INFLECTION-POINT AT 4.1.	70
FIGURE 23: ELECTROSTATIC PROPERTIES AND DISTRIBUTION OF pK_a VALUES OF PsbO-B IN THE CONTEXT OF PSII.....	71
FIGURE 24: COMPARISON OF Cph1 Δ 2 U- ^{13}C , ^{15}N]-PCB AT 400 MHZ IN BLUE AND SELECTIVELY ^{13}C -WIRV U- ^{15}N LABELLED Cph1 Δ 2 U- ^{13}C , ^{15}N]-PCB AT 800 MHZ IN RED.	75
FIGURE 25: 1D HC-CP SPECTRUM OF Cph1 Δ 2 Pr STATE WITH U- ^{13}C , ^{15}N]-LABELLED PCB, AT 800 MHZ AND 261 K.	77
FIGURE 26: TEMPERATURE COMPARISON AT 800 MHZ.	78
FIGURE 27: SUPERPOSITION OF 1D HC-CP IN GREEN WITH 2D ^{13}C - ^{13}C DARR SPECTRUM IN BLUE.....	79
FIGURE 28: STRUCTURE (A) AND X-BAND DERIVATIVE EPR SPECTRA (B) OF M-TINYPOL AND bcTOL-M AT 100 K.....	80
FIGURE 29: DNP FIELD PROFILES OF CARBON DIRECT EXCITATION SPECTRA OF bcTOL-M (A) AND M-TINYPOL (B).	82
FIGURE 30: ALIPHATIC REGION OF PROLINE SAMPLE bcTOL-M DOPED. CARBON DIRECT EXCITATION SPECTRA RECORDED AT DIFFERENT FIELD STRENGTHS WITHOUT MICROWAVE IRRADIATION.	83

FIGURE 31: ALIPHATIC REGION OF M-TINYPOL DOPED PROLINE SAMPLE. CARBON DIRECT EXCITATION SPECTRA RECORDED AT DIFFERENT FIELD STRENGTHS RECORDED WITHOUT MW IRRADIATION.	83
FIGURE 32: FIELD PROFILES OF bcTOL-M AND M-TINYPOL.	84
FIGURE 33: COMPARISON OF bcTOL-M AND M-TINYPOL ON BIOLOGICAL SAMPLE CPH1Δ2 AT 18.789 T.....	86
FIGURE 34: CHEMICAL SHIFT DISTRIBUTION OF ARGININE, ISOLEUCINE AND VALINE C _A AND C _B RESONANCES.	90
FIGURE 35: UV-VIS SPECTRA OF PR SAMPLE IN (A) AND PFR SAMPLE IN (B).	91
FIGURE 36: SPECTRA OF CPH1Δ2 IN THE PR STATE RECORDED UNDER DNP CONDITIONS.	92
FIGURE 37: COMPARISON OF 2D PROJECTIONS OF hCANCOCa SPECTRA RECORDED ON CPH1Δ2 IN THE PR STATE IN BLUE AND IN THE PFR STATE IN PINK.	94
FIGURE 38: ASSIGNMENT OF THE IVR REGION.....	95
FIGURE 39: COMPARISON OF TRYPTOPHAN RESIDUES IN PR AND PFR STATE.	98
FIGURE 40: BINDING-POCKET OF CPH1.	105

List of tables

TABLE 1: ISOTOPES AND THEIR SPIN AND MAGNETIC QUANTUM NUMBERS.	2
TABLE 2: hCANCOCa PULSE SEQUENCE PARAMETER.	55
TABLE 3: pK _A VALUES OF ASPARTIC ACID AND GLUTAMIC ACID RESIDUES.	64
TABLE 4: DNP ENHANCEMENT AND SENSITIVITY FACTOR OF PROLINE bcTOL-M.....	85
TABLE 5: DNP ENHANCEMENT AND SENSITIVITY FACTOR OF PROLINE M-TINYPOL	85

1 General Introduction

1.1 Biophysical Concepts

1.1.1 Basic principles of (solid state) NMR

This chapter will provide an overview of the basic principles of NMR. It covers the parts needed to understand the content of this thesis but does not strive for completeness. For a detailed introduction to NMR Spectroscopy the reader is referred to the educational books of Malcolm Levitt (1) and James Keeler (2) that cover solution NMR and Melinda Duers excellent work highlighting solid state NMR principles (3).

NMR is an atom specific technique that exploits the feature that many nuclei possess a property called spin, which depends on the specific number of protons and neutrons in the nucleus. Nuclei with a half-integer or integer spin quantum number I are so-called NMR active. A selection of nuclei and their respective spin quantum number are displayed in Table 1.

Table 1: Isotopes and their spin and magnetic quantum numbers.

Isotope	Spin Quantum number I	Magnetic Quantum Number m
^{12}C , ^{18}O	0	-
^1H , ^{13}C , ^{15}N , ^{19}F , ^{29}Si , ^{31}P	1/2	-1/2, +1/2
^2H , ^{14}N	1	-1, 0; +1
^7Li , ^{23}Na , ^{37}Cl , ^{87}Ru	3/2	-3/2; -1/2, 1/2, 3/2
^{17}O , ^{25}Mg , ^{27}Al	5/2	-5/2, -3/2, -1/2, 1/2, 3/2, 5/2

It is convenient to work with nuclei of spin $\frac{1}{2}$. Since the magnetic quantum number m goes with $2I+1$, it can only take on two values $+\frac{1}{2}$ and $-\frac{1}{2}$ for spin $\frac{1}{2}$ nuclei, which facilitates the description of interaction between nuclei and magnetic field. Moreover, spin $\frac{1}{2}$ nuclei do not experience quadrupolar couplings, as these are only present between nuclei with a spin higher than $\frac{1}{2}$. The energy levels of a nucleus with different magnetic quantum numbers m are degenerate in the absence of an external magnetic field. Under the influence of an external

magnetic field these energy levels split up according to the magnetic quantum number m . This is called the Zeeman effect. The higher the spin quantum number the more energy levels arise. For a nucleus with a spin $\frac{1}{2}$ we get a splitting of energy in two populations parallel α ($+\frac{1}{2}$) and antiparallel β ($-\frac{1}{2}$) to the B field. The alpha state is energetically favourable and has the lowest energy of the two levels. The difference between the energy levels is described by the following equation:

$$\Delta E = \hbar\gamma B_0 \quad (1)$$

With ΔE being the energy difference, \hbar the reduced Planck constant, γ the gyromagnetic ratio of the nucleus and B_0 the magnetic field strength. The higher the gyromagnetic ratio of the nucleus the bigger the energy difference and the more sensitive the nucleus is for NMR. The gyromagnetic ratio and relative Zeeman splittings of proton ^1H , carbon ^{13}C and nitrogen ^{15}N , the three most important isotopes in biomolecular NMR, are shown in Figure 1.

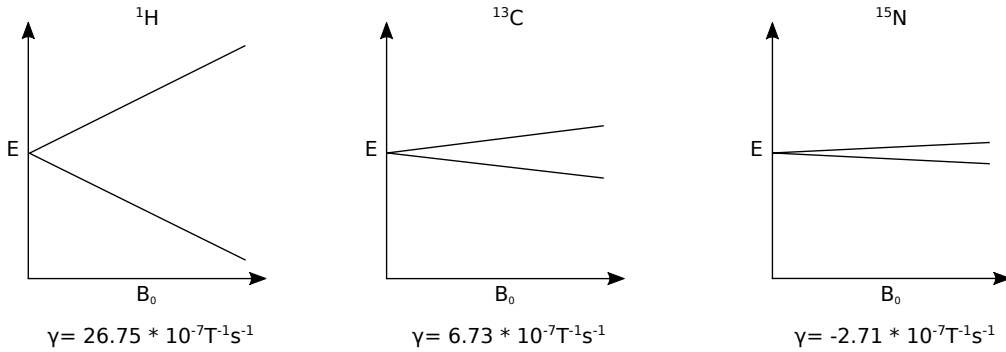


Figure 1: Relative Zeeman splittings of proton (^1H), carbon (^{13}C) and nitrogen (^{15}N) isotopes according to their gyromagnetic ratio.

Transitions between the energy levels can be induced at the resonance frequency ν which is known as the Larmor frequency of the nucleus and is described using the relationship $\Delta E = h\nu$ with:

$$\nu = \frac{\gamma B_0}{2\pi} \quad (2)$$

In angular frequency units ω , this can be rewritten as follows:

$$\omega = \gamma B_0 \quad (3)$$

The difference in population of the two states at ambient temperature is in general very small, which makes NMR a relatively insensitive technique since the intensity of an NMR signal is proportional to the population difference. The Boltzmann distribution describes the population difference at thermodynamic equilibrium as follows:

$$\frac{N_{\beta}}{N_{\alpha}} = e^{-\frac{\Delta E}{kT}} \quad (4)$$

Here, N is the occupation number of the two energy levels α and β , k the Boltzmann constant and T the temperature. From this can be understood that the ‘the ideal measurement conditions’ (i.e., yielding the highest sensitivity) are thus provided at high magnetic field strengths, a nucleus with high gyromagnetic ratio and a low temperature. A technique that exploits these conditions is dynamic nuclear polarisation (DNP), a hyperpolarisation method that works at cryogenic temperatures. The basic principles of DNP are described on page 13.

The population difference results in a macroscopic net magnetization M_0 along the B_0 field, which is per definition the z component in a three-dimensional coordinate system. The magnetisation is thus called longitudinal. A common conception is the vector model, which describes the net magnetisation as vector precessing with the Larmor frequency around B_0 . This concept will be used to describe the processes taking place during an NMR experiment. In Figure 2 the basic steps are illustrated.

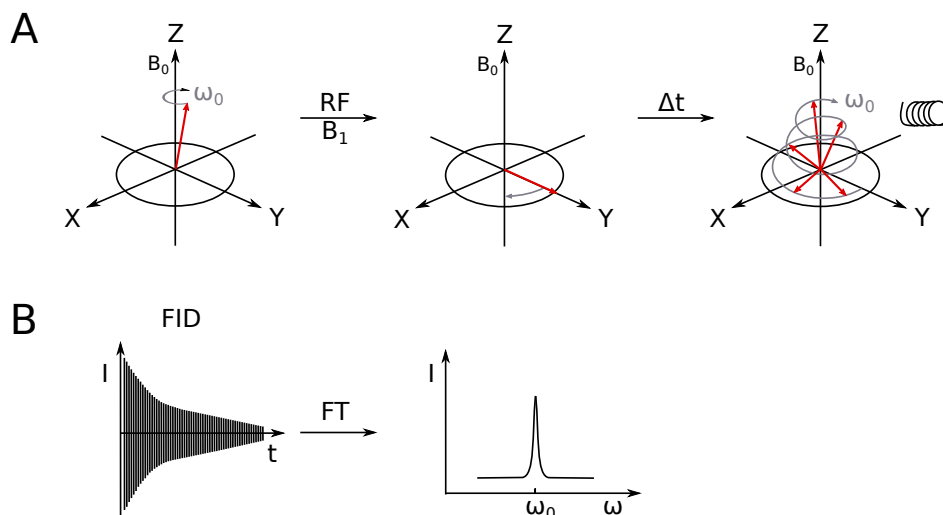


Figure 2: Simplified description of the generation of an NMR signal using the vector model. (A) The magnetisation vector (red) is precessing around B_0 with the Larmor frequency ω_0 . When a radiofrequency pulse (rf) is applied, the vector is tilted into the XY-plane. It precesses in the XY-plane and returns after time back to the initial equilibrium state. The precession is detected by a coil along X. (B) The time dependent signal is detected as Free Induction Decay FID. Fourier transformation (FT) of the FID results in an NMR frequency dependent spectrum.

By applying a radiofrequency (rf) pulse along X, also referred to as B_1 field, along X the magnetisation vector is tilted in the XY-plane leading to transverse magnetization. The rf pulse is usually generated by inducing a current in a coil surrounding the sample and needs to be on resonance, which means equal or close to the Larmor frequency of the nuclei of interest. As the magnetization vector precesses in the XY-plane it induces a current in the detection coil. This is how the Free Induction Decay (FID) is recorded. The signal is decaying as the magnetization vector returns to its longitudinal equilibrium state (T_1 relaxation) and due the loss of coherence within the bulk magnetization (T_2 relaxation). A Fourier transformation (FT) of the FID leads to a signal at the Larmor frequency in the NMR spectrum.

In a homogeneous magnetic field, the resonance frequency of a nucleus strongly depends on its chemical environment. Electrons that interact with the magnetic field generate small local fields that have a shielding effect. This shielding effect can be large or small, which is often (relatively) referred to as shielding and

deshielding. An example are aromatic ring structures which we find for example in the phenylalanine side chain. The delocalized electrons induce an aromatic ring-current, which shields nuclei above the ring (an effect also known as ‘ring-current shift’), whereas the protons that are located outside the ring are deshielded, granting them a particular resonance frequency. The resulting frequency shift in the NMR spectrum is called chemical shift. The local electronic environment thus determines the chemical shift of a nucleus and since every nucleus in a molecule is in a unique chemical environment, and hence experiences different electrostatic interactions, the chemical shift is a unique property of a nucleus in a specific molecular position.

Since the chemical shift correlates linearly with the magnetic field strength one must use a reference system to make the chemical shift values independent of B_0 and thus comparable. In equation 5 we see that this is achieved when the chemical shift δ is given relative to a reference compound with a resonance frequency of ν_{ref} .

$$\delta(\text{ppm}) = \frac{\nu - \nu_{\text{ref}}}{\nu_{\text{ref}}} 10^6 \quad (5)$$

These usually very small values are commonly multiplied by a factor of 10^6 and referred to as parts per million (ppm). The higher the magnetic field the larger the ratio Hz/ppm and the better the resolution of a spectrum. Resolution is essential, especially when working with large molecules such as proteins. A protein consists of amino acids which share the same functional groups such as carbonyl- or amide groups that constitute the protein backbone. Even though their chemical shifts differ, peak overlap inevitably occurs in crowded spectra of large proteins; one possibility to reduce overlap is to acquire the NMR data at higher field strengths or to record multidimensional spectra.

To improve resolution in solid state NMR one makes use of a technique called magic angle spinning (MAS). A major difference between solid state and solution

NMR is the chemical shift anisotropy (CSA), which can be neglected in isotropic solutions due to the rapid isotropic molecular tumbling which averages the effect to zero. In solids, however, the CSA is not averaged and can significantly broaden the NMR lines. In addition, the rapid tumbling in solution also averages out the dipolar couplings. Both CSA and dipolar couplings can seriously compromise the resolution in solids. The chemical shift of a nucleus is described as a tensor (3x3 matrix) with the three principle axes being X, Y, and Z and the corresponding principal values δ_{xx} , δ_{yy} and δ_{zz} . The isotropic part of the chemical shift, which is usually meant when speaking of a chemical shift, arises from the trace of the matrix, which equals the mean of the three principle values as follows:

$$\delta_{iso} = \frac{1}{3}(\delta_{xx} + \delta_{yy} + \delta_{zz}) \quad (6)$$

In solution the rapid motion of the molecules averages the chemical shift to the isotropic chemical shift (δ_{iso}), which is independent of the orientation of the molecule with respect to the external B_0 field. In a solid each molecule of a sample can have a slightly different orientation as shown in Figure 3A. Since the anisotropic chemical shift is dependent on the orientation of the molecule, this leads to substantial signal broadening and the resulting NMR spectrum is the superposition of the shifts from all molecular orientations. The pattern has a typical shape shown in Figure 3B, which is also referred to as ‘powder spectrum’.

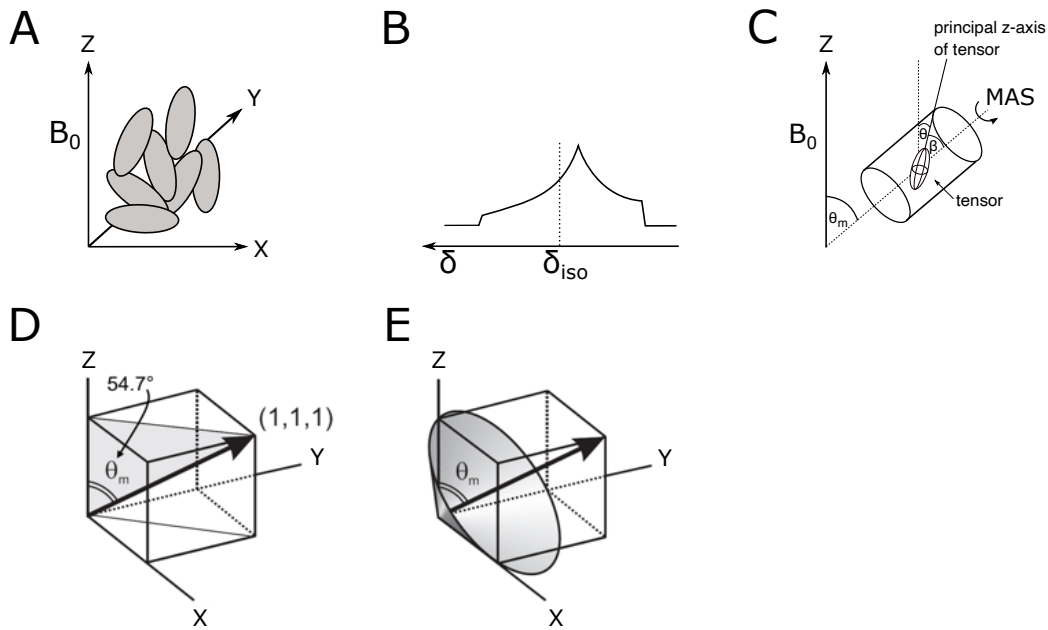


Figure 3: Chemical shift anisotropy, powder pattern and magic angle spinning. (A) Orientation of molecules within a solid powder in the principle axes system. (B) Example of a powder pattern spectrum. (C) Spinning of a rotor at the magic angle of 54.74° with respect to the B_0 field. (D) The magic angle shown as the body diagonal of a cube. (E) A cone precession is described when rotating around the body diagonal, comprising x , y and z -axis.

The CSA broadening can be eliminated by using a small sample tube (rotor) that is rotating around an axis which is inclined at an angle of 54.74° with respect to the external B_0 field, as shown in Figure 3C. This angle is the so-called magic angle, and equals the angle of the body diagonal of a cube with respect to the z -axis (Figure 3D). By rotating a molecule around this axis, the three spatial orientations are averaged, since the three axes X , Y and Z are converted into one another during each rotation (Figure 3E) and the resulting isotropic chemical shift can be measured.

When working with solids other interactions that have to be cancelled manually are dipolar couplings. At high magnetic field dipolar interactions are described by the following secular approximation of the dipole-dipole coupling spin Hamiltonian, in this case for a homonuclear spin pair j and k :

$$\widehat{\mathcal{H}}_{jk}^{DD}(\theta_{jk}) = b_{jk} \frac{1}{2} (3 \cos^2 \theta_{jk} - 1) (3 \widehat{I}_{jz} \widehat{I}_{kz} - \widehat{I}_j \widehat{I}_k) \quad (7)$$

b_{jk} being the coupling constant $\frac{-\mu_0 \gamma_j \gamma_k \hbar^2}{16 \pi^3 r^3}$ with μ_0 being the magnetic constant, γ_j and γ_k the gyromagnetic ratios of the nuclei, \hbar the Planck constant, r the distance between the nuclei and θ_{jk} the angle between the vector of the dipolar coupling and the external B_0 field (1).

To eliminate the dipolar coupling, one of the two terms has to become zero. The average of the term $(3\cos^2 \theta_{jk} - 1)$ when rotating around an axis at an angle θ_m is shown in the following equation (3):

$$\langle 3\cos^2 \theta_{jk} - 1 \rangle = \frac{1}{2} (3\cos^2 \theta_m - 1)(3\cos^2 \beta - 1) \quad (8)$$

The angles are defined in Figure 3C. θ_m is the angle between B field and rotor axis, θ_{jk} (equals θ in Figure 3C) is the angle between the B field and the principal z axis of the tensor and β the angle between the principal axis of the tensor and the rotor axis. By setting the angle θ_m to $54,74^\circ$ the dipolar interactions are averaged at fast spinning speeds:

$$3\cos^2 \theta_m - 1 = 0 \quad (9)$$

Another solution for the equation would be an angle of $\pi - 54,74^\circ = 125,26^\circ$, which is generally not used as it is non-practical.

In multidimensional NMR experiments the magnetization is transferred between spins via scalar or dipolar coupling, depending on the pulse sequence. A large amount of pulse sequences has been developed over the last decades and is accessible in dedicated libraries. The building blocks of a typical 2D NMR sequences are preparation, evolution, mixing time, and detection. Figure 4 explains this concept by means of the 2D hCC-DARR (Dipolar Assisted Rotary Resonance (4)) pulse sequence. The pulses are shown for proton and carbon independently.

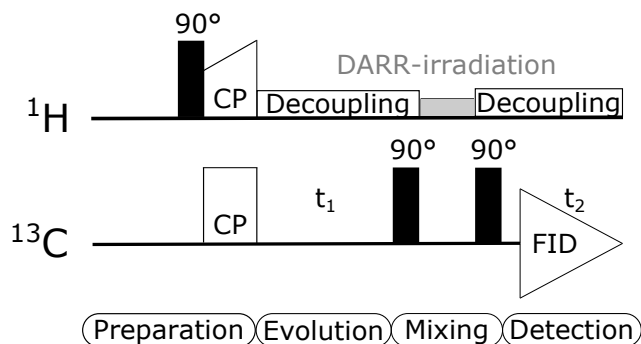


Figure 4: hCC DARR pulse sequence. Classification of the different stages during a two-dimensional experiment. Pulses of the proton channel on the top and of the carbon channel at the bottom. 90° pulses shown as filled rectangles, the cross-polarisation pulse labelled as CP. The two acquisition times are t_1 in the indirect dimension (evolution) and t_2 in the direct dimension (detection).

During the preparation period XY-magnetisation is generated on proton and transferred via a cross-polarisation (CP) step to carbon.

A multidimensional experiment can comprise several time evolution periods, during which the magnetisation is labelled with the chemical shift of the respective nucleus. This is denoted as indirect acquisition. In the 2D DARR sequence the carbon magnetisation evolves during t_1 time. The 2D experiment is recorded as a series of 1D's, where for each 1D experiment t_1 is incremented. Throughout the mixing period, magnetisation is exchanged between the carbon nuclei, driven by the DARR-pulse on proton. In the subsequent direct detection period t_2 the FID is recorded on carbon resulting in a carbon-carbon correlation spectrum. The dimensionality of pulse programmes depends on the number of indirect acquisition times, the higher the dimension the better the resolution but the more time consuming the experiment becomes. To avoid this, one can implement other sampling methods such as non-uniform sampling (NUS). This way of spectral acquisition is not linear. A specific sampling schedule is used, defining which data points are recorded or omitted, and the spectrum needs to be reconstructed (5,6).

The transfer of magnetisation can occur through-bond, using scalar couplings (J-couplings) or through-space exploiting either dipolar couplings or the nuclear

Overhauser effect (NOE), which is a cross-relaxation effect. In solution NMR coherence transfers are mainly based on J-couplings or NOE since the dipolar couplings are averaged to zero due to the rapid isotropic molecular tumbling of the molecules in solution. Scalar couplings arise, as opposed to dipolar couplings, from bonding electrons between two nuclei and are thus exclusively intramolecular. The J-coupling between nucleus I and S is characterized by the coupling constant J_{IS} which is field independent and usually given in Hertz. J-couplings can span several bonds and their strength is independent of the orientation of the interacting spins. They are significantly weaker than the dipolar couplings. One distinguishes between homo- and heteronuclear transfer and short- or long-range interactions.

One of the prominent building blocks in solution NMR exploiting the J-couplings is the Insensitive Nuclei Enhancement by Polarisation Transfer (INEPT), which is generally applied to transfer magnetisation from a nucleus with a high gyromagnetic ratio for example ^1H to an insensitive nucleus with a lower gyromagnetic ratio, like ^{15}N . The INEPT sequence consists of a series of synchronised 90° and 180° pulses on the I (^1H) and S (*e.g.* ^{15}N) spin. Magnetisation is exchanged during the delay τ between the pulses. This process is denoted as evolution of J-coupling and readily described by the product operator formalism, which will not be further discussed in this work. τ correlates with the coupling constant J_{IS} of the nuclei as follows: $\tau = 1/2J_{IS}$.

In solid-state NMR magnetisation is often enhanced by using cross polarisation (CP), which exploits transfer from a high- γ spin (*e.g.* ^1H) to a low- γ spin (*e.g.* ^{13}C or ^{15}N). CP is based on the dipolar couplings. During a CP transfer two on-resonance pulses (the so-called ‘spin-lock pulses’) are applied simultaneously on both types of nuclei as shown in Figure 4. During the contact time one can imagine the two spin populations in their respective rotating frame stationary

along the Y axis. The population difference of the spin X is zero at the beginning of the pulse. To allow a magnetisation transfer from I to X the spin-lock pulses have to fulfil the Hartman-Hahn (HH) matching conditions. Without MAS, the HH-condition is fulfilled when the energy splittings due to the two spin-lock pulses are equalled (7).

$$\gamma_I B_1(I) = \gamma_X B_1(X) \quad (10)$$

Here γ_I and γ_X are the gyromagnetic ratios of the nuclei I and X, respectively, and B_I and B_X the applied spin-lock pulses. Under MAS the HH-condition also incorporates the spinning frequency:

$$(\omega_1^I - \omega_1^X) = n(\pm\omega_r) \quad (11)$$

Here ω_1^I and ω_1^S are the amplitudes of the spin-lock pulses of the nuclei I and S in angular units, respectively, and ω_r is the MAS spinning frequency. If this requirement is satisfied, magnetisation can be exchanged between the two spin baths since the energy differences of the I and X spin splittings during the spin-lock pulses are equalized, which guarantees that the net energy of the system is conserved during the transfer process. The underlying mechanism is linked to the dipolar coupling between the two spins, whose strength determines rate of magnetisation transfer (3).

In principle the CP transfer can be applied to any pair of nuclei, though it is rather unspecific and not quantitative. With a short contact time, efficient transfer generally only takes place between nuclei at a relatively short distance. CP works best for rigid systems as local motions effectively reduce the dipolar couplings. Due to the absence of strong dipolar couplings in liquids, CP is mainly used in solid state NMR.

1.1.2 Dynamic Nuclear Polarisation

The insensitivity of NMR is one of its biggest drawbacks. This can partly be compensated by the construction of magnets with higher magnetic field strengths. Following an entirely different approach, signal enhancement by dynamic nuclear polarisation (DNP) has been pursued since the 1950s with the discovery of the polarisation transfer from electrons to nuclei in metals under microwave (MW) irradiation by Albert Overhauser (8). He proposed that the enhancement of nuclear polarisation could be a breakthrough for NMR insensitivity, forasmuch as technical issues such as high-power MWs and very low temperatures could be solved. It took half a century, with the development of gyrotrons as stable high-power MW source and the continuous effort of the group of Robert Griffin, till DNP was ready to be used for biological applications. Instead of starting with the polarisation of protons as it is the case in conventional ssNMR, in DNP the electron polarisation is exploited. For this, mono- or bi- radicals with unpaired electrons are added as polarising agents to the sample. The unpaired electrons have a much larger gyromagnetic ratio, thus the Zeeman level splitting at the same field strength and temperature, is several orders of magnitude larger (in the GHz range) than that of nuclei (MHz range). When matched with the right MW frequency, the electron polarisation is propagated to the surrounding protons. The proton magnetisation in turn gets distributed throughout the entire sample via spin diffusion and can be transferred to the low- γ nuclei of interest using cross polarisation. The theoretical signal enhancement ε is calculated as the ratio of the gyromagnetic ratio of the electron spin S , and respective nuclear spin I , under the precondition $\gamma_S \hbar B_0 \ll k_B T$ as follows (9):

$$\varepsilon_{max} = \frac{P_S}{P_I} \approx \frac{\gamma_S}{\gamma_I} \quad (12)$$

Here P_S is the polarization of the electron spin, P_I the nuclear spin polarisation, γ_S and γ_I are the gyromagnetic ratios of the electron and nucleus. For the polarisation transfer from electrons to protons, from the γ 's a theoretical ε_{max} of 660 can be calculated. For nuclei with a smaller gyromagnetic ratio ε_{max} is even higher. Depending on the external magnetic field strength and the composition of the sample itself, experimental enhancement factors of around 10 to 250 have been reported on biological samples (10–13). To experimentally determine the enhancement of a sample, one records an experiment twice, once with MWs turned off and once with MWs switched on, and calculates the ratio of the signal intensities. As an example, the superposition of two hC-CP spectra of L-proline with and without MWs under DNP conditions is shown in Figure 5.

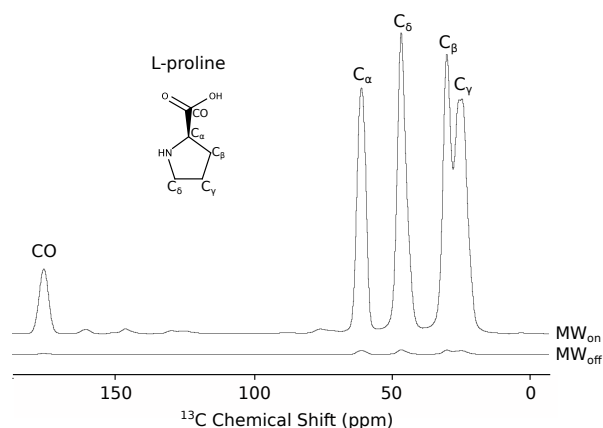


Figure 5: L-proline hC-CP spectra. Superposition of two hC-CP spectra recorded with the polarising agent *M-TinyPol* on L-Proline with (MW_{on}) and without (MW_{off}) microwaves at 100K. Signals are assigned to the respective carbon atom of the analyte.

DNP differs from conventional solid-state NMR in the instrumentation, a general schematic overview of the setup is shown in Figure 6. In addition to the console and the magnet, DNP requires a stable MW source, in our case a gyrotron (9.7 T, 527 GHz) as well as a low temperature (LT) MAS unit with a heat exchanger inside. A pressurized external liquid nitrogen tank is connected to constantly refill the N_2 bath of the heat exchanger. The bearing, drive and variable temperature gas is cooled down to the desired cryogenic temperatures in the heat

exchanger, each gas has its own pipeline and the temperature and gas flow is thus controlled separately. A transfer line connects the heat exchanger with the probe. In order to maintain the cryogenic temperatures, the transfer line and probe need to be evacuated. Only at temperatures below 180 K MWs are allowed to be emitted by the gyrotron to the probe via a corrugated waveguide. This protects the sample and probe from heat damage. With this system sample temperatures between 90 and 100 K can be reached, a further drop in temperature to values below 30 K can be achieved with a closed cycle helium cooling system (14–16).

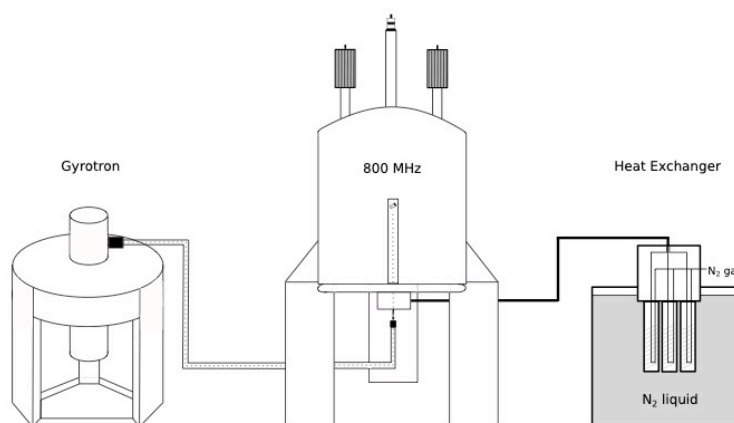


Figure 6: DNP setup. A gyrotron as stable microwave source provides microwaves of a particular frequency via a corrugated waveguide to the NMR probe. The special evacuated probe inside the NMR magnet has three separate inlets for precooled bearing, drive and VT gas. A heat exchanger enables controlled cooling of nitrogen gas to cryogenic temperatures of 100 K.

The source of the electron polarisation is a polarising agent (PA) with unpaired electrons. A common DNP sample consists of the analyte of interest which is dissolved in a glass-forming matrix doped with a PA. As matrix, a 60 % d8-glycerol, 30 % D₂O and 10 % H₂O mixture is often used, which prevents ice crystal formation within the sample at the cryogenic temperatures applied during the measurement. The deuterons reduce the number of bulk protons, which provides a more efficient spin diffusion to spread the nuclear hyperpolarisation through the sample during MW irradiation. A variety of PAs has been developed in the past, amongst them are diverse monomeric radicals and nitroxide

biradicals (17–19). Paramagnetic metal ions can be used as well if contained in or introduced to the analyte molecule (20). Depending on the type of radical a different initial polarisation transfer mechanism is exploited.

In the next section the three major mechanism, Overhauser-effect (OE)(8), solid effect (SE)(21) and cross effect (CE)(22,23) and their application will be explained in detail. Thermal mixing (TM)(24,25), a fourth DNP mechanism, solely contributes to the polarisation transfer at very low temperatures ($T < 10$ K)(9) and will be omitted in the discussion. The observation of the Overhauser-effect in the 1950s was the vital spark of DNP. Initially the electron paramagnetic resonance (EPR) single quantum transition of the PA has to be excited by a matching MW irradiation. Fluctuations in the amplitude of the hyperfine interaction (HI) between an electron-nucleus spin pair can then cause cross-relaxation events between the nuclear and the electron spin, which are described as zero quantum (‘flip-flop’) and double quantum (‘flop-flop’) transitions (26). If these spontaneous transitions are imbalanced a hyperpolarization of the nuclear spins is obtained.

Fluctuations of the HI are primarily induced by solvent dynamics and it thus has been assumed for a very long time that the Overhauser-effect is only evident in liquids and conducting solids with mobile electrons (26). Very recent studies have demonstrated the Overhauser-effect with BDPA (1,3-bisdiphenylene-2-phenylallyl) radicals in insulating solids (27,28). Here the effect similarly relies on fluctuations in hyperfine couplings, though their origin is a different one than in solution. Vibrations at low frequencies in the BDPA radical, which are still present at very low temperatures, have been proposed as possible HI source in insulating solids. Taken together with the specific composition of BDPA, comprising a large delocalized electron network as well as many protons (see Figure 7), strong variations of the hyperfine couplings can be induced (28).

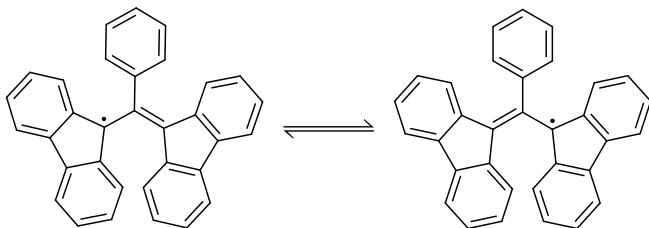


Figure 7: Mesomeric structures of BDPA. The position of the radical is delocalized and stabilized through the biphenyl moieties.

In contrast to the solid effect (SE) and the cross effect (CE) the OE scales favourably with the magnetic field strength in non-conducting solids, meaning that at a higher field larger the enhancements are observed at the electron resonance frequency (27). With an enhancement of 80 at 120 K, one of the highest enhancements measured at 18.8 T has been reported by Lelli *et al.*, via the OE, with BDPA as radical of choice (29). In their work, it was furthermore shown that at a field of 9.4 T the OE didn't decay significantly with the increase of temperature until the glass-forming temperature T_g is reached at 240 K. This opens up possibilities for using DNP at higher temperatures, which reduces the effect of heterogeneous broadening and allows the study of dynamic processes with DNP. So far, the Overhauser effect has only been observed with BDPA in rotating solids, hence enforcing the development of radicals to exploit this mechanism would be especially beneficial for the development of high field DNP. Since the production of stable high-power gyrotron sources for high fields is difficult, the DNP technique was mostly developed on for NMR magnets operating at low B_0 fields (5 – 9.4 T) and as a consequence a plethora of radicals exists that are optimized to work at low field. Suitable radicals for biological applications at higher field strengths (14.1 – 21.1 T) need to be developed/improved (19,30).

The solid effect is a two-spin mechanism between an electron spin and a dipolar coupled nucleus, which becomes the dominant effect in a system where the EPR linewidth of the polarising agent is smaller than the nuclear Larmor

frequency (31,32). The interactions between electron and nucleus are described by H_{en} , a part of the spin Hamiltonian, as follows:

$$H_{en} = H_{en}^{iso} + H_{en}^{aniso} \quad (13)$$

For the SE to occur the spatial parts of H_{en} have to be time-independent. The pseudo-secular hyperfine coupling terms ($S_z I^+$ and $S_z I^-$) of H_{en}^{aniso} then lead to mixing of nuclear spin states (33). Due to the presence of mixed spin-states, forbidden ZQ or DQ transitions can be excited by MW irradiation, provided that the following matching condition $\omega_{0S} \pm \omega_{0I} = \omega_{\mu w}$ is fulfilled, where ω_{0S} is the electron resonance frequency and ω_{0I} the nuclear resonance frequency and $\omega_{\mu w}$ the MW frequency. A comparison of the enhancement profiles and corresponding EPR spectra of the Overhauser, solid and cross effect is shown in Figure 8. The probability of the occurrence of ZQ and DQ transitions is described by a mixing factor that is proportional to ω_{0I}^{-2} and inherently small (34). SE is thus most effective at low magnetic field strengths ($\epsilon \sim B_0^{-2}$) and requires high MW powers as well as mono-radicals or paramagnetic metal ions with a small EPR linewidth

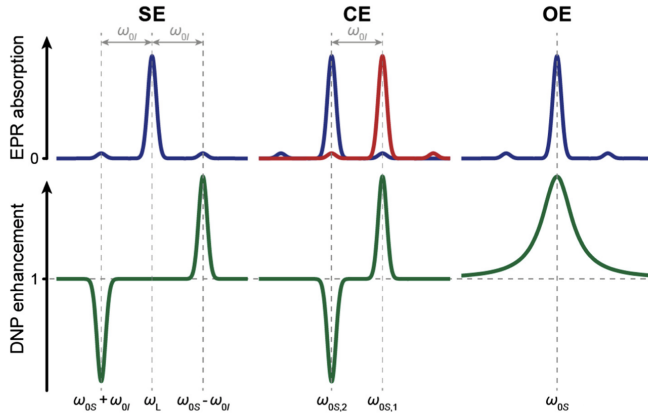


Figure 8: EPR spectra and enhancement profile of solid effect, cross effect and Overhauser effect modified after Thankamony et al.(9). Here $\omega_L = \omega_{0S}$ is the electron Larmor frequency and ω_{0I} the nuclear Larmor frequency. Two electrons are involved in CE and their respective EPR absorption line is shown in red and blue, the corresponding DNP enhancement is maximal at the two electron Larmor frequencies $\omega_{0S,1}$ and $\omega_{0S,2}$.

as polarising agents. The cross effect is the most efficient polarisation transfer mechanism that has been described so far. It shows a more favourable field dependency of $\epsilon \sim B_0^{-1}$, which makes the CE more suitable for higher magnetic

field strengths than SE (35). In biological DNP experiments at high magnetic fields CE is the dominant mechanism, provoking the highest enhancements (31). It requires a three-spin system of two electron spins with the resonance frequencies ω_{e1} and ω_{e2} coupled to a nuclear spin with a Larmor frequency of ω_{0I} . The demanded matching condition for a polarisation transfer via cross effect is satisfied when the difference of the electron frequencies equals the nuclear Larmor frequency: $|\omega_{e1} - \omega_{e2}| = \omega_{0I}$ (36). To fulfil this condition the PA can either be a biradical that provides two electron resonance frequencies with optimal difference, or a mono-radical with a large g anisotropy, *e.g.* the EPR line of the PA is broader than ω_{0I} . The two interacting electrons can derive from different radical molecules or PA types. When the MW irradiation matches one of the two EPR transitions, the coupled nuclear spin gets hyperpolarised. This hyperpolarisation is then transferred via spin diffusion throughout the sample to other nuclei. To reach a maximal hyperpolarisation, it is important that the PA is uniformly distributed throughout the sample. Assuming complete saturation, the spin polarisation of the nuclei (I) equals that of the electron spin polarisation (S) leading to a theoretical enhancement of $\frac{\gamma_S}{\gamma_I}$ (37).

In a rotating sample the generation of hyperpolarisation is described with periodically arising level anti-crossing (LAC) events (38). CE rotor events where the matching condition is fulfilled and MW rotor events during which irradiation of the EPR resonance frequency is accomplished are the driving force of nuclear hyperpolarisation and can occur independently from another (9). A third LAC event is the dipolar event, where the resonance frequencies of the two electron spins are equal, thus allowing the exchange of polarisation between them. If the dipolar coupling between those electron spins is small, a loss of electron polarisation will be generated during these events (37). Hence high radical concentrations can lead to an inefficient hyperpolarisation of the sample.

In this context it is important to mention that the paramagnetic effects caused by the PA's lead to an initial depolarisation of the sample (39). This implicates that the nuclear polarisation is smaller than that of the Boltzmann thermal equilibrium, which would have been reached in the absence of a PA. The determination of the enhancement factor by comparing the MW on/off signal intensities is thus an insufficient means to characterize a PA. For this reason, several alternative methods for the assessment of a PA's quality have been developed within the DNP community. Among others, the '10-minute signal to noise measurement', has been established as quality test. It is used in this work and will be explained in section 2.2.5.

1.1.3 Sedimentation NMR

Sedimentation NMR (SedNMR) (40,41) approach offers a possibility to study soluble proteins using ssNMR. This approach is particularly valuable for proteins that exceed the molecular weight limit for solution NMR and are not suitable for crystallization. The transient immobilisation of an analyte by sedimentation mimics a solid state which enables the application of ssNMR techniques. Protein sedimentation is a reversible process (see Figure 9).

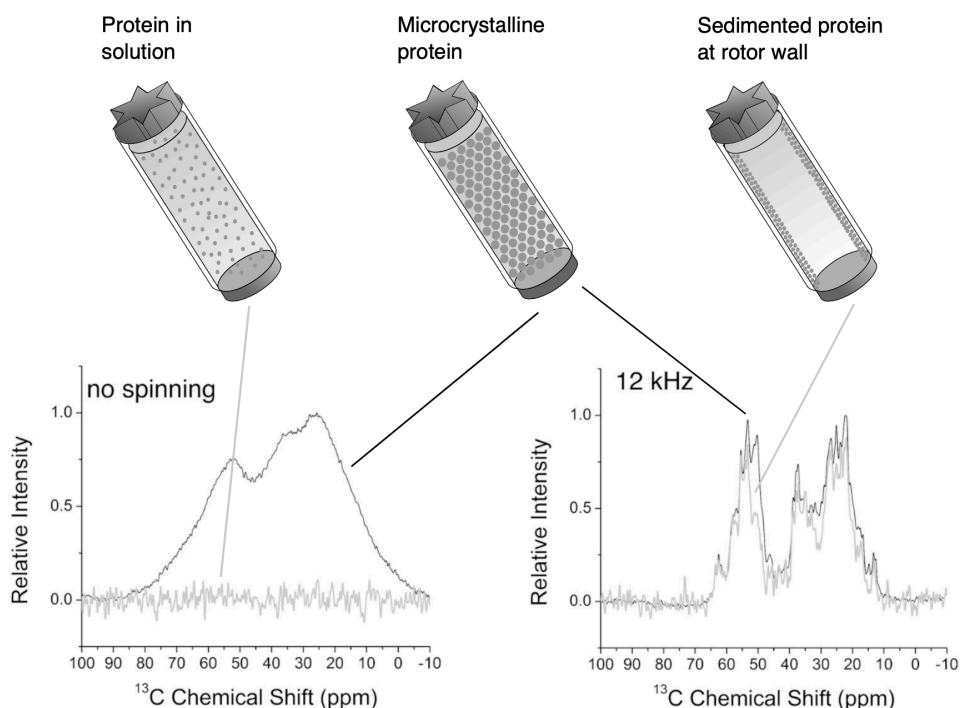


Figure 9: Comparison of protein sedimentation in the rotor with a microcrystalline protein preparation. Spectra shown without spinning and at 12 kHz MAS spinning speed.

Compared to other methods that rigidify proteins such as precipitation or freezing, sedimentation is considered to be a mild treatment that preserves the native state of a protein (42). While it has been recently shown that ssNMR samples prepared by sedimentation tend to be stable over several years regarding signal intensity and spectral similarity (43), sample homogeneity is one of the drawbacks in sedNMR as sediments are mostly amorph. The microscopic effects of sedimentation on the free diffusion of a molecule can be described by molecular crowding. The molecular dynamics of a protein in solution depend on its

translational and rotational diffusion rates, which are described by the Brownian motion (44). Molecular crowding induces volume exclusion and increases protein-protein as well as hydrodynamic interactions, which reduce the translational and rotational diffusion (45). It is thus important to discriminate sedimentation from a simple increase of viscosity by the addition of a co-solute, which simply reduces the translational correlation and is often not sufficient for effective immobilization on an NMR timescale.

Sedimentation can be achieved by MAS directly in the NMR rotor during the measurement (in situ) or by the use of ultracentrifugation during sample preparation prior to NMR acquisition (ex situ) (40) as shown in Figure 10. The latter can be used for proteins with low molecular mass, to concentrate the protein solution to a level that allows sedimentation onto the rotor walls when subjected to MAS.

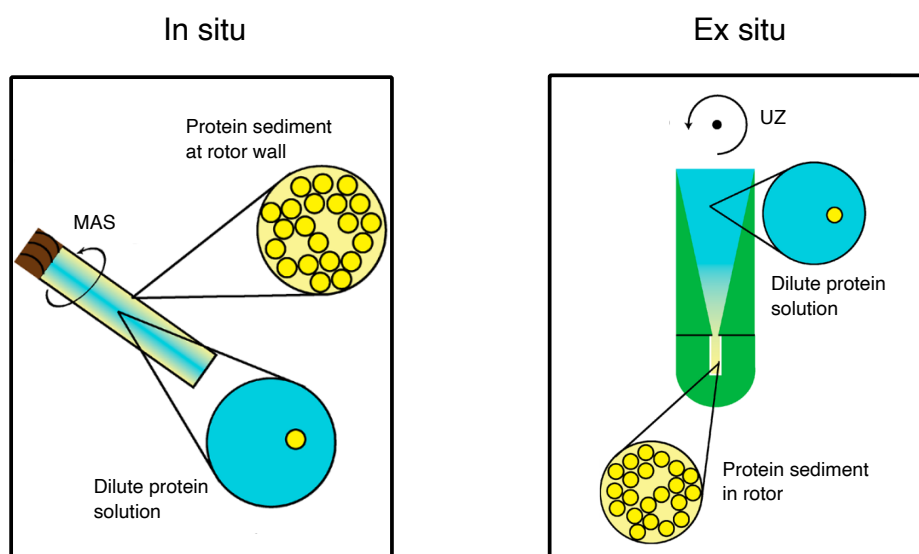


Figure 10: The different sedimentation approaches in NMR. In situ sedimentation on the left and ex situ sedimentation on the right. Figure modified after Bertini et al. (40).

The amount of sediment generated by in situ sedimentation depends on the spinning speed and rotor diameter as well as the protein concentration and molecular weight. A description of the protein concentration in relation to the distance r from the rotor axis is given by the following equations (42).

$$c(r) = \frac{c_{limit}}{1 + A \exp\left[\frac{M(1-\rho_{solvent}/\rho_{protein})\omega_r^2 b^2}{2RT}\right]} \quad (14)$$

with the integration constant A specified as:

$$A = \frac{\exp\left[\frac{M(1-\rho_{solvent}/\rho_{protein})\omega_r^2 b^2}{2RT}\left(1 - \frac{c_0}{c_{limit}}\right)\right] - 1}{1 - \exp\left[\frac{M(1-\rho_{solvent}/\rho_{protein})\omega_r^2 b^2}{2RT} \frac{c_0}{c_{limit}}\right]} \quad (15)$$

In these equations c_{limit} is the maximal protein concentration (around 700 mg/mL for a globular protein), M is the molecular weight (kg/mol, kDa), ρ ist the density (kg/dm³) ω_r the angular rotor speed (rad/s), b is the rotor inner-radius (m), R the universal gas constant, T the temperature (K) and c_0 is the initial protein concentration in the static rotor. With the use of these equations, it is possible to determine the required protein concentration for the sedimentation of a protein with a specific molecular weight for a specific rotor diameter at a specific spinning speed. For instance, in a 1.9 mm Bruker rotor at 42 kHz spinning speed, the concentration for the sedimentation of a 50 kDa protein should exceed 164 mg/mL (40).

1.1.4 Chemical exchange and 1D NMR spectroscopy

One of the largest advantages of NMR compared to other structural biology techniques, such as cryo-EM or X-ray crystallography, is the possibility to acquire data at physiological temperatures, which preserves dynamic processes. We can study a system in a macroscopic equilibrium while chemical exchange processes can happen on a microscopic level. The term chemical exchange or dynamic NMR (DNMR)(46,47) applies to processes that affect specific nuclei on-site without changing the overall constitution of the sample. Examples are the rotation around a bond, ring flipping events, the fluxionality of ligands or proton exchanges with the solvent at -NH or -OH groups with weakly attached protons. These reactions happen on a timescale between nanoseconds to seconds and they can be described at chemical equilibrium with equation 16.



The reaction rate k can be described by equation 17.

$$k = \frac{k_B T}{h} e^{-\Delta G^\ddagger / RT} \quad (17)$$

Here k_B is the Boltzmann's constant, h the Planck constant, ΔG^\ddagger the Gibbs free energy of activation and R the gas constant. The reaction rate and thus chemical exchange is temperature sensitive (46).

In a one-dimensional NMR spectrum, we have two different sources of information, which are the line position (chemical shift) and the line width of the signal. The line width contains information about the transverse relaxation rate R_2 and in the chemical shift we find the precession frequency of the nucleus (48). The influence of chemical exchange on such an NMR spectrum depends on its timescale. We normally distinguish between slow, intermediate and fast exchange. The largest effect is observed in the intermediate exchange regime, where the timescale of the exchange is of the same order as the difference in precession frequencies $\Delta\nu$ between the two states, $k \sim \Delta\nu$. As the frequencies are

used in units of Hertz, the chemical exchange is field dependent and varies for different types of nuclei as well. In the intermediate exchange regime, we expect short relaxation times which lead to a significant line broadening that can even result in the complete loss of a signal. The signal merges into one broad resonance for the two states. When the line shape has a flat top we speak of coalescence, which occurs when reaction rate k satisfies the following equation.

$$k = \frac{\pi\Delta\nu}{\sqrt{2}} \quad (18)$$

In the slow exchange regime, chemical exchange has only a small influence on the line shape. When the exchange reaction rate $k \ll \Delta\nu$, we expect two separated peaks for the two states with line broadening similar to field inhomogeneities.

When the exchange reaction rate is much higher than the frequency difference between the two states ($k \gg \Delta\nu$) we are in the fast exchange regime. Here we observe almost no line broadening and the line width resembles the natural peak width (46). Instead of two distinct resonances we expect one sharp line as the NMR timescale is too slow to distinguish between the two states.

NMR spectroscopy is a useful method to study chemical exchange and for the accurate determination of rate constants related to changes in the magnetic environment of a nucleus. On the other hand, the influence of the chemical exchange itself on an NMR spectrum is often unfavourable, since it leads to line broadening and transverse relaxation processes.

1.1.5 Principles of pK_a titration in NMR

Ionizable groups on the protein surface contribute significantly to the electrostatic properties and thus determine molecular interaction and function of a protein. The determination of protein acid dissociation constant (pK_a) values is an instrument to characterize titratable groups. It is often used to gain information about the protein stability and solubility regarding the pH dependency of these properties.

The equilibrium reaction between an acid HA and the corresponding base A^- is described as $HA \xrightleftharpoons{K_a} A^-$ with equilibrium constant $K_a = \frac{[A^-][H^+]}{[HA]}$, where [HA] is the concentration of the non-dissociated acid and $[A^-]$ and $[H^+]$ of the dissociated ions. Until today the Henderson-Hasselbalch equation (19), proposed in 1916 (49), is used to describe the correlation between pH, equilibrium constant K_a and the ratio of the concentrations $[A^-]$ and [HA]:

$$pH = pK_a + \log \left(\frac{[A^-]}{[HA]} \right) \quad (19)$$

It is important to note that the Henderson-Hasselbalch equation only accounts for dilute solutions of a weak acid, which is the case when regarding amino acid side chains on the protein surface.

The pK_a value itself, opposing to its name, is not constant but depends on several parameters such as temperature, dielectric constant of the solvent and ionic strength within the system (50). Keeping these conditions constant is a requirement for a proper determination of pK_a values, independent from the biophysical technique used. NMR has become one of the standard methods for the site-specific pK_a determination of protein ionizable groups as the chemical shift of a nucleus is very sensitive towards changes in the chemical environment (51). The choice of the nucleus monitored, usually 1H , ^{13}C or ^{15}N , depends on the functional group of interest and is rarely the ionizable proton itself, as it is not

continuously present over the whole range of pH titration. The reporter nucleus should be close to the ionizable group, unambiguously assignable and its chemical environment sensitive to the de-/protonation event. The chemical shift change is monitored in dependence of the pH, which is only possible if the equilibrium reaction is fast on the NMR timescale (see section 1.1.4 fast exchange). The respective signal has to be isolated and resolved. To avoid ambiguities, it can be advantageous to combine the information of all possible reporter groups for one titration event.

Standard titration experiments are 2-dimensional ^1H - ^{15}N HSQC spectra for histidine side chain titrations or $\text{H}_2(\text{C})\text{CO}$ for carboxyl groups of glutamic and aspartic acid side chains (52). The HSQC spectra are additionally used to monitor protein stability and folding, which is of particular importance when defining the range of the pH titration. Protein unfolding or local conformational changes can be triggered by pH titration. The chemical shift of a reporter nucleus close by is sensitive to these rearrangements and the titration curve would no longer exclusively reflect the ionisation reaction.

Titration curves observed by NMR are usually analysed using the modified Hill equation for a one-step titration as described in (53):

$$\delta_{obs}(pH) = \frac{\delta_{AH} + \delta_{A^-} \cdot 10^{n(pH - pK_a)}}{1 + 10^{n(pH - pK_a)}} \quad (20)$$

with δ_{HA} and δ_{A^-} being the chemical shift of the fully protonated and deprotonated form of the titratable group and n the Hill coefficient as means for the quantification of cooperativity within the de/protonation reaction which is reflected in the steepness of the curve. The pK_a value is read out at the reflection point of the curve.

The pK_a determination by NMR is in general a very precise method, systematic errors mainly result from inaccurate pH adjustments during sample preparation or local temperature fluctuation due to rf induced heating. A general accuracy is

estimated with ± 0.05 log units (50). One of the biggest challenges is the interpretation of the data. The assignment of a titration curve to an ionisation site has to be accurate. Difficulties result from groups which share a proton and titrate together leading to multiphasic titration curves, or so called ‘ghost titrations’ where a reporter nucleus senses a second titration event in close proximity which then superimposes the proper titration curve (54). In these cases, it is crucial to apply a suitable model to fit the titration curve and to distinguish between the titration events (55).

1.1.6 Conceptual idea of protonation dynamics in proteins

Cellular processes are highly dynamic and need to be tightly regulated at the same time. A fast and energetically favourable way to control cellular processes and protein function is via non-covalent interactions. Proteins consist of a network of non-covalent interactions such as hydrogen-bonds, coulomb interactions, dipole-dipole and hydrophobic interactions, which stabilize the protein structure (56). A change in these interactions can thus induce structural rearrangements and, acting on the assumption that form follows function, regulate protein activity (57). Protonation dynamics in this context is a means to control and coordinate protein function by spatial and temporal variations in the hydrogen-bond network. At this point, residues with protonatable side chains such as histidine, cysteine, arginine as well as glutamic and aspartic acid are of special interest. There several examples in the literature where a proteins function is controlled by the protonation state of a single residue. MD simulations of the trypsin-benzamidine binding pathway have shown that the protonation state of a histidine residue, which is not part of the trypsin catalytic triad, regulates binding of benzamidine (58). Another example is EmrE, a transmembrane protein of *E.Coli*, which couples the import of two protons with the extrusion of hydrophobic cations. The protonation of a glutamic acid side chain induces functional relevant conformational changes that modulate the substrate affinity of the transporter (59). It is thus not surprising that protonation has been considered as a posttranslational modification (60) and that the proton transport mechanism is intensively studied regarding the energetic requirements and dynamic of a proton transfer.

An explicit definition of the term protonation dynamics is given by the collaborative research centre 1078 (CRC1078, Sonderforschungsbereich SFB 1078) (sfb1078.de). It includes:

-
- (1) the displacement of protons by less than 1 Å, which is described by a proton shift within a hydrogen bond,
 - (2) the delocalisation of protons in aqueous solution (formation of Zundel and Eigen cations) and at the protein-water interface when protonatable side chains are present,
 - (3) long-distance proton transfer mediated by the interaction of cluster of protonatable groups at the protein surface with surrounding water molecules, which are often accompanied by
 - (4) the rearrangement of hydrogen-bonded networks in the protein core and at the surface involving de-/protonation reactions, changes in positioning of water molecules and amino acid residues (side chains rotations),
 - (5) induced global structural changes in the protein backbone and rearrangement of secondary structural motifs,
 - (6) long-range electrostatic interactions.

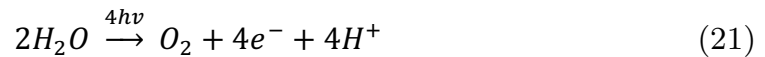
We are working with two systems (as introduced in section 1.2), that show protonation dynamics in the sense of (4) and (5) (phytochrome) and (3) and (6) (PsbO), which will be analysed and discussed in this thesis.

1.2 Biological Systems

1.2.1 *PsbO: A Photosystem II associated Protein involved in Proton transport*

Photosynthesis is one of the biological processes to render life on earth possible, with the fixation of carbon dioxide and the release of oxygen by plants and bacteria. The latter is generated during the light reaction in special compartments of the plant's thylakoid membrane of chloroplasts, harbouring many copies of the required set of proteins: the two Photosystem complexes PSI and PSII with the associated light harvesting complexes LHCI and LHCII, Cytochrome b_6f and ATP synthase (61).

Photosystem II, also known as water plastoquinone oxidoreductase, is the site where photolysis takes place, a process in which photons are absorbed and the energy is used to catalyse the oxidation of water as shown in the subsequent equation (62).



PSII is a complex system of more than 40 subunits of low molecular weight composing a homomeric dimer in the thylakoid membrane as shown in Figure 11. PsbO, highlighted in green, is one of the membrane-associated proteins that reach into the luminal space of the thylakoids. It is conserved across cyanobacteria, algae and plants and essential for the generation of oxygen which is significantly reduced in PSII mutants lacking PsbO (63).

PsbO is located in close proximity to the oxygen evolving centre (OEC), a Mn_4Ca -oxo cluster which is the catalytic centre where the water oxidation takes place. Until now PsbO is identified as manganese stabilising protein, executing its function by adjusting the calcium and chloride concentration to an optimal level for water oxidation and protecting the manganese centre against reducing

agents (64). Being close to the site of proton release, PsbO has some noticeable features that suggest an additional function in proton transport. As illustrated in equation 21, two protons are released per molecule of oxidised water during photosynthesis. Thus, a fast proton removal needs to be assured to prevent acidification of the part of PSII surrounding the

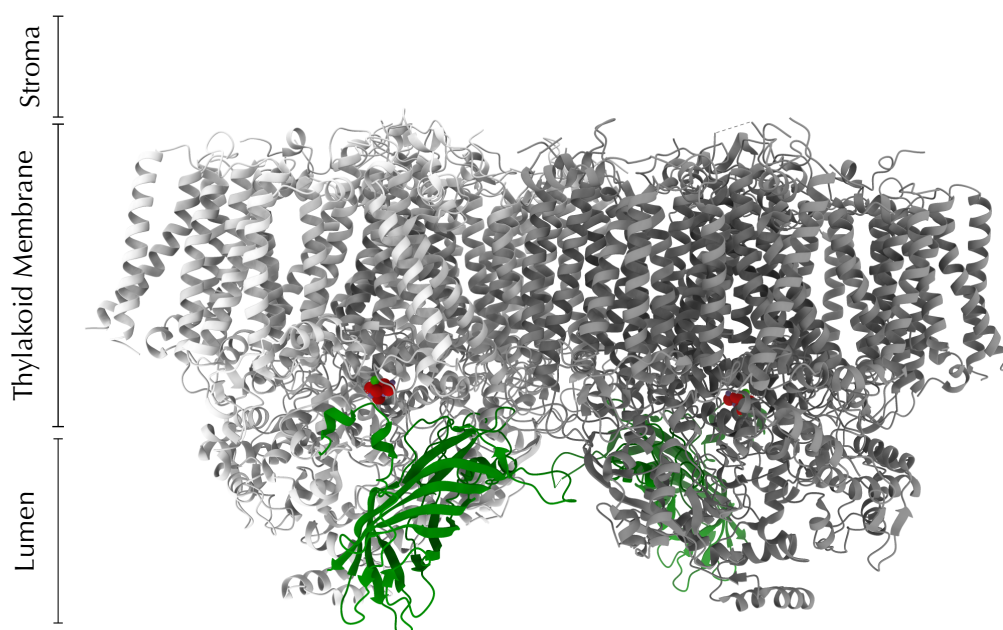


Figure 11: PsbO in Photosystem II dimer. Full length PsbO protein in green, Oxygen Evolving Center coloured by element in spheres, all other PSII Subunits and associated proteins in shades of grey.

OEC. PsbO harbours 34 amino acids with a protonatable side chain, 19 glutamic and 15 aspartic acids, of which roughly 90 % are surface exposed and accessible from the luminal part of the thylakoid. A proton transport from the OEC towards the luminal space along the surface of the beta barrel structure of PsbO involving these amino acids seems to be likely. Additionally, several so-called proton exit-channels have been proposed and residues of PsbO are involved in all of them (65). These channels allow a guided proton transport over long distances by providing water molecules or protonatable amino acid side chains along which proton hopping comparable to the Grotthuss mechanism (66) can occur. The amino acids involved in this proton transport need to be electrostatically stabilised by the environment and possess titratable groups

within the right pK_a range. Such a stabilisation can occur when several carboxylate groups are in close proximity to another and form a cluster. The negative charge is delocalized within the cluster and enables a fast proton transfer. A series of carboxylate clusters can form a proton conducting network granting the proton transport an explicit direction.

Besides the release of protons at the OEC, the pH of the thylakoid lumen plays a crucial role for the functionality of photosynthesis. While the light reaction takes place, additional protons are transported from the stroma into the thylakoid lumen and generate a proton driving force which is necessary for the formation of ATP by ATP-synthase. Contrariwise it is known that at pH values below 5 an inactivation of PSII occurs (67) leading to an inhibition of the O_2 formation. Thus, the pH of the thylakoid lumen needs to be tightly regulated. A fast mechanism to prevent over-acidification of the lumen during periods of permanent light irradiation in plants is energy-dependent quenching (qE)(68), the major component of the process of non-photochemical quenching (NPQ) (69). qE is directly linked to the luminal pH and induced by the protonation of PSII proteins (70,71). The PsbO protein could also have a small buffer capacity, assisting the incipient NPQ mechanism to prevent the acidification of the lumen at periods of fluctuating light intensities. The surface carboxylate groups can get transiently protonated on a fast timescale and therefore store part of excess light energy in the form of chemical energy for a certain amount of time.

To investigate the role of PsbO in photosynthesis-related proton management and to add some experimental data to the computational work, we were interested in the determination of pK_a values of the many glutamic and aspartic acid side chain carboxylate groups on the surface of PsbO.

PsbO consists of a rigid beta barrel core structure reaching far into the luminal space and long hydrophilic, flexible loop regions that mediate interactions with

other proteins of PSII (72). The inside of the barrel is blocked by bulky hydrophobic residues which prevent potential water or proton transport directly through the core of PsbO (73).

We worked with a short (33 kDa) construct in solution, that lacks the flexible loops which are presumed to be unstructured for the isolated protein in solution, because the stabilising contacts to PSII are absent. However, the protein fold is similar to the one of the full-length PsbO within PSII with only minor exceptions (64). For comparison, the structures of the full-length protein and the short construct are superimposed in Figure 12A. The positions of the aspartic and glutamic acid residues and the orientation of their carboxylate side chains (depicted as red sticks) are highly similar in both proteins and the beta strands that compose the barrel structure are on top of each other.

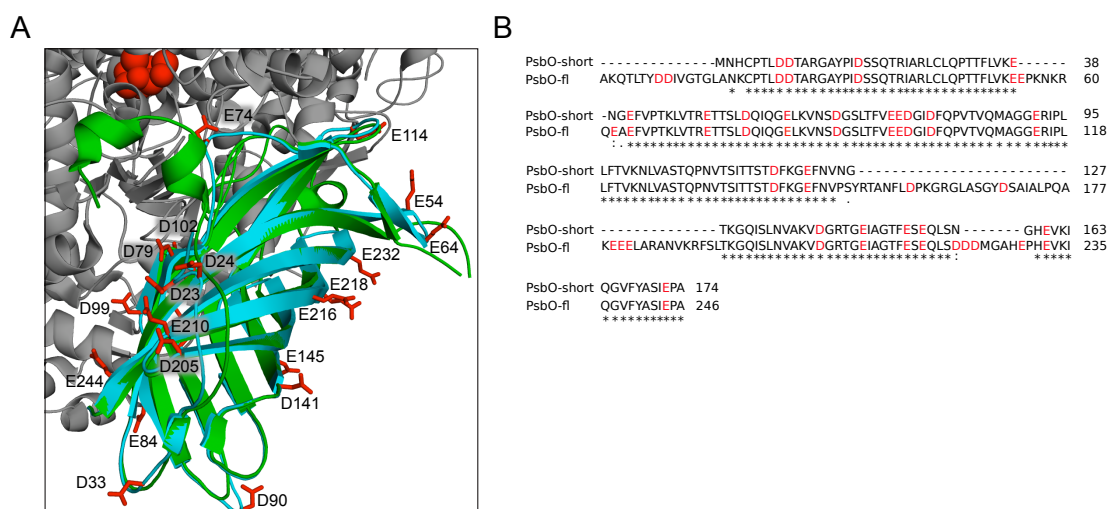


Figure 12: Comparison of full-length protein and the short construct used in our studies. (A) Superposition of full-length (green) and short PsbO (cyan) in PSII (grey). Glutamic and aspartic acid residues are highlighted in red and numbered according to the full-length construct. OEC is depicted with red spheres. (B) Sequence alignment of short and full-length protein. Glutamic and aspartic acid residues are highlighted in red, asterisks indicate consensus between the sequences.

The sequence alignment of both constructs in Figure 12B illustrates that the short variant is lacking 15 N-terminal amino acids, as well as three loop regions (55 – 63, 149 – 192 and 220 – 231) which were replaced by short Asp-Gly β -hairpins to fill in the gaps of the deleted loops. Additionally, the N-terminus of

the short construct starts with a tripeptide (Met-Asn-His) that does not belong to the full-length PsbO sequence of *Thermosynechococcus elongatus*.

With trimming the flexible loops, we also removed 13 glutamic and aspartic acid residues of the PsbO sequence. Among them are Asp158, Asp169, Glu179-Glu181, Asp223 and Asp224, which are supposed to be part of the proton exit pathways (72,74). Since these residues are part of the loops interacting with the proteins D1 and D2 of PSII, they would be in a different environment when working with the isolated protein in solution, thus show a modified pK_a value.

The 22 glutamate and aspartate residues of the short construct are conserved to a high degree (75), solvent accessible and surrounded by a comparable electrostatic environment when isolated from PSII. They are numbered accordingly to the full-length sequence for easier comparison and were characterized regarding to pK_a values measured by solution NMR.

1.2.2 Analysing light-induced molecular changes in *Phytochrome Cph1Δ2*

Phytochromes comprise another example for light regulated systems in plants, algae and bacteria. They belong to the photoreceptor family and control important growth and development processes such as germination, flowering and senescence (76). Phytochromes are molecular switches that absorb red and far-red light, between 600 and 750 nm, and convert between two states: an active state, which is for canonical phytochromes the far-red absorbing state Pfr, and an inactive red absorbing state, Pr (77). Pfr is induced upon light absorption. It is thermally unstable and the reversion to Pr is favoured at high temperatures, in the dark or by absorption of far-red light (76). The forward reaction of the Pr/Pfr conversion has been studied intensively over the past decades and is thus well described in the literature (78–81). Phytochromes are located in the cytosol and translocate after activation to the nucleus where they interact with different transcription factors of the phytochrome interacting factor family (82) and thereby activate downstream processes.

They are dimeric proteins and each protomer is equipped with a bilin chromophore, which is responsible for the light absorption (83). In higher plants phytochromobilin (PΦB) serves as chromophore, whilst in algae and bacteria phycocyanobilin (PCB) is responsible for light absorption. Both PΦB and PCB are heme derivatives which are covalently bound to the phytochrome at a cysteine residue (84). The PCB chromophore structure and the absorption spectra of the Pr and Pfr state are shown in Figure 13. Phytochromes share a common organization that is independent from the descending organism. They consist of two different modules, the N-terminal photo sensory model (PSM) which is involved in light absorption and signalling and bears the chromophore, and the C-terminus that is responsible for localisation and dimerization (85,86).

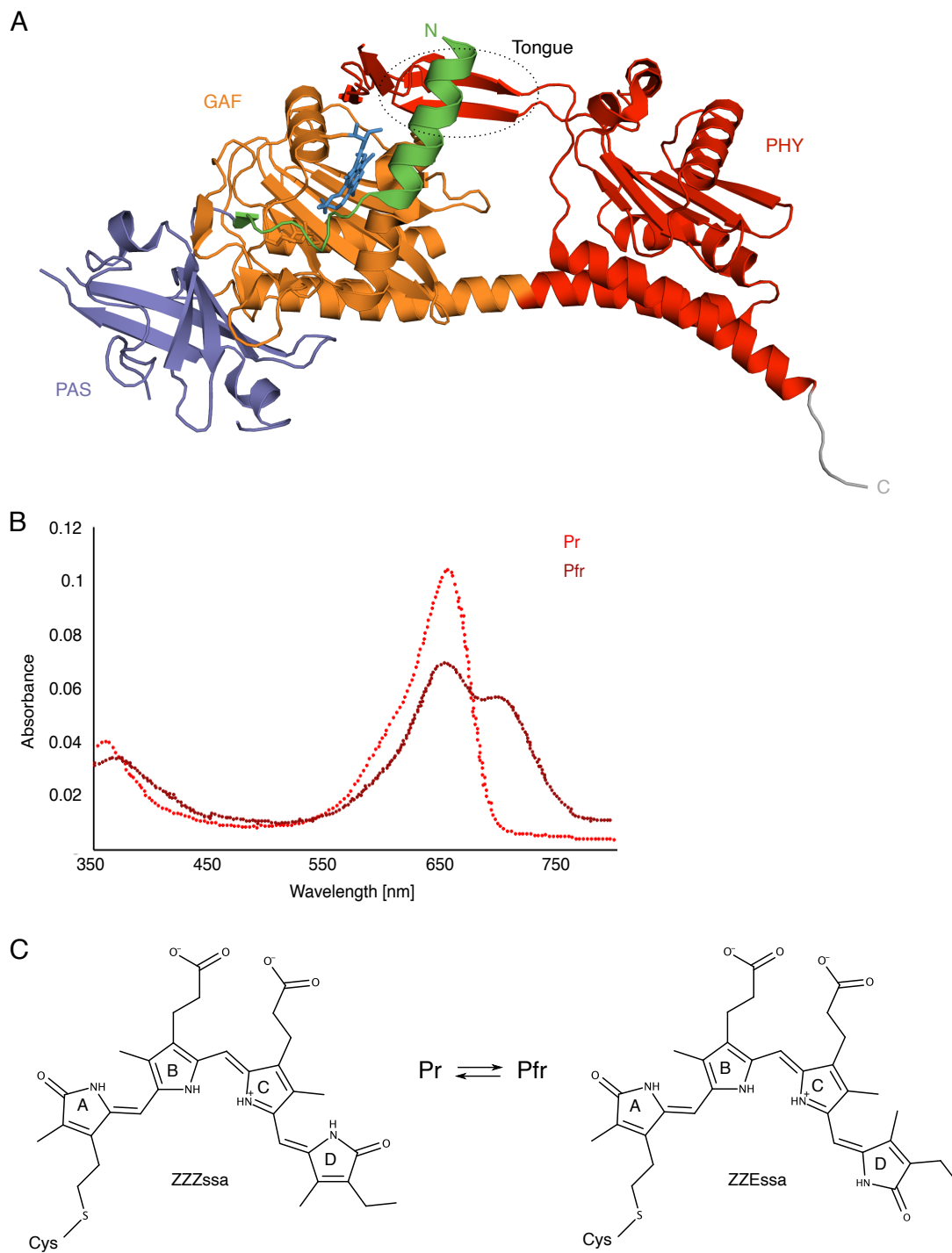


Figure 13: Features of cyanobacterial phytochrome Cph1. (A) Ribbon model based on the crystal structure 2VEA, showing the photo sensory module of Cph1 in the Pr-state presented as monomer. PAS, GAF and PHY domains are shown in violet, orange and red, respectively, the N-terminus in green and C-terminus in grey. The 'tongue' region is encircled. Light-blue shaded chromophore PCB is covalently attached to the GAF domain. (B) UV-Vis spectra of Cph1 in Pr (red) and Pfr (dark red) state showing absorption maxima at 660 and 730 nm respectively. Pfr state is not pure. (C) Phycocyanobilin in two conformations, ZZZssa in the Pr state and ZZEssa in the Pfr state. The main difference is the flip of ring D around the methine bridge.

In prokaryotic phytochromes a histidine kinase domain (HK) is located at the C-terminus in control of signal transduction. In plants the HK is replaced by a histidine kinase-related domain (HKRD) (81). Kinase activity has been shown for various prokaryotic and plant phytochromes (80,87,88), which is supposed to be an additional signal transduction mechanism of the phytochrome family besides the nuclear translocation and interaction with PIFs. Further components of the plant phytochrome domain architecture are the tandem PAS domains, located between the PSM and the C-terminus, and the N-terminal extension (NTE) (81).

The PSM comprises a Period-ARNT-single-minded domain (PAS), a cGMP phosphodiesterase/adenylyl cyclase/FhlA domain (GAF) and a phytochrome (PHY) domain (85). In Figure 13A the crystal structure of the Cph1 PSM is shown. The PAS-GAF domains are tightly interconnected, with the GAF domain bearing the chromophore at a cysteine residue. The PHY domain is separated thereof by a long alpha helix. As additional connection between the domains serves the so-called 'tongue' region, a short structural motif that sits on top of the chromophore binding pocket (89). It seals the binding pocket and thereby guarantees solvent exclusion (79). Existing PAS-GAF structures of prokaryotic phytochrome have shown that these two domains alone are insufficient to enable photo conversion, a requirement to obtain a stable and active Pfr state is thus the PHY domain (89). Though experiments with plant phytochrome B in *Arabidopsis* have suggested that conversion to Pfr and signal transduction is possible in an N-terminal construct without PHY, but the stability of the Pfr state is significantly reduced resulting in a quick dark reversion (90). The PHY domain - and with it, the 'tongue' region - seems to be an important factor for the conversion of phytochromes into their stable signalling state. Interestingly, the 'tongue' region can adopt two different secondary structural motifs, an alpha

helix or a beta strand, which was initially observed while comparing crystal structures of phytochromes Cph1 and *Pa*BphP (81). With the two structures of the bacteriophytochrome *Dr*BphP in the resting Pr and active Pfr state, it became clear that the ‘tongue’ region is likely to undergo a structural change during photo conversion. The authors observed a beta sheet structure of the ‘tongue’ region in the dark-adapted Pr state, that converts to an alpha helix in the crystal structure of the illuminated protein, which goes along with a shortening of this region (91).

The photo conversion is described as follows: upon light absorption, the D ring of the chromophore flips as a result of an Z to E isomerisation at the C15,16 methine bridge (92). This leads to the redirection of contacts between the chromophore and the residues of the chromophore binding pocket and the surrounding water network. These variable interactions are proposed to translate in the two distinct structural elements of the ‘tongue’. It is unknown if the ‘tongue’ refolding is a unique feature of bacteriophytochromes or if it applies to the whole family.

A better understanding of the aspects of structural changes during the photoactivation of phytochromes would aid to improve their application in optogenetics. Phytochromes bear several features which render them promising candidates for optogenetic tools (93): the absorption of light in the far-red range that can penetrate tissues without harm, the two distinct and relatively stable states, the spectral properties of the two states, e.g. having non-overlapping absorption maxima and their general structure being composed of a sensing and a signalling unit which can be replaced by other output modules and/or modified with engineering techniques (94). One example for an optogenetic tool is the fusion of a Cph1 variant with murine fibroblast growth factor receptor 1 (mFGFR1) which was transfected into HEK293 cells. Light illumination leads to

dimerization of the protein which then activates the MAPK/ERK pathway. The activation was still measurable when the light stimulus passed through 10 mm thick mouse tissue (94). Phytochromes as optogenetic tools have a high potential for the application in the pharmaceutical industry. The obvious method of choice to monitor dynamic processes that are accompanied by structural changes within a protein is NMR spectroscopy. In the current study, we want to observe changes in the ‘tongue’ region within a single sample of the cyanobacterial phytochrome Cph1.

1.3 Objective and scope of the thesis

In plants or other light-sensitive organisms energy conversion or biological signalling is accomplished via a complex sequence of events. Hereby, the absorption of photons often leads to an alteration of protonation pattern, either directly in the excited protein or subsequently at other subunits. In this work, the primary events upon light absorption or the proton exchange pattern in affected domains are investigated by means of two examples, a phytochrome and a photosystem subunit. In both cases ‘protonation dynamics’, which describes the regulation of protein function by spatial and temporal rearrangements in the hydrogen-bond network, plays a significant functional role.

The PSII associated protein PsbO is located in the thylakoid lumen close to the Oxygen Evolving Centre (OEC). PsbO is known as manganese-stabilising extrinsic subunit of PSII and bears a large hydrogen-bond network on its surface. We aim to characterize the proton affinities of all glutamic and aspartic acid carboxyl groups in PsbO by solution NMR, towards the idea of surface carboxylate cluster operating as proton antenna for the evacuation of protons from the OEC.

The numerousness of charged groups on the surface of PsbO together with the sequence-specific conservation of these residues from cyanobacteria to plants raise the question of a functional relevance and an auxiliary role of PsbO in PSII.

With our experiments we want to:

- 1) understand if the carboxylate network on PsbO’s surface permits a directed transport of protons from the OEC to the thylakoid lumen,
- 2) determine the pK_a values of aspartic and glutamic acid residues, and
- 3) elaborate if or to what extent structural rearrangements in the protein backbone accompany pK_a titration events.

In detail, the analysis of PsbO surface pK_a by solution NMR requires the complete assignment of protein backbone as well as the side chain carbon resonances of glutamic and aspartic acid residues. pH titration experiments will be employed to determine surface pK_a values and monitor the stability of the protein backbone. A Henderson-Hasselbalch fit will be employed to evaluate the data and subsequently calculate the pK_a values.

The second model system is the cyanobacterial phytochrome Cph1, that ignites a signal transduction chain upon light reception. Phytochromes are a class of photoreceptor proteins which are prevalent in many organisms ranging from bacteria and cyanobacteria to fungi and plants. They regulate seed germination, plant growth and flowering. A covalently bound chromophore is responsible for the light-reception, and signal transduction involves changes in the interaction between chromophore and protein.

Cph1 and its covalently bound chromophore phycocyanobilin is one of the many phytochrome systems examined over the last decades. One of the questions addressed thereby is how the signal is transduced from the chromophore to the protein. Studies that employed solution (95) and solid-state NMR (78,79,92,96,97) have mainly focussed on the structure of the chromophore and its interactions within the binding pocket. An interesting structural element sealing the binding pocket is called the ‘tongue’ region. Upon light irradiation, rearrangements of the hydrogen-bond network in the binding pocket are transmitted to the ‘tongue’ region, which is then supposed to change its secondary structure as part of the signal transduction pathway. While this region shows a beta-sheet fold in crystal structures of canonical phytochromes in the Pr state (89,98), crystal structures of bathy phytochromes in the Pfr state reveal an alpha-helical fold of the ‘tongue’ region (99–101). In bathy phytochromes Pr and Pfr state are reversed, rendering Pfr the stable dark-adapted state. This work

will focus on the ‘tongue’ region of the photo-sensory module of Cph1 (Cph1 Δ 2) and monitor its structure in the inactive Pr state as well as the active Pfr state within one sample. Different NMR techniques will be applied, which benefit from a reduced labelling scheme of Cph1 Δ 2. Conventional solid-state NMR at high field (18.8 T) will be combined with sedimentation NMR and DNP. SedNMR enables the study of soluble proteins such as Cph1 Δ 2 by ssNMR. For the application of high-field DNP experiments, the two nitroxide radicals bcTol-M and M-TinyPol will be characterized regarding their field profile, enhancement and stability. This study will be among the firsts to analyse a biological system by recording 3D spectra under DNP conditions, at 18.8 T (800 MHz proton frequency).

The two projects have been done in collaboration within the collaborative research centre 1078 (SFB1078) with the groups of Ana-Nicoleta Bondar, Holger Dau, (Free University of Berlin), Holger Dobbek, Athina Zouni (Humbolt University of Berlin) and Jon Hughes (University of Gießen).

2 Material and Methods

2.1 Solution NMR of PsbO

2.1.1 Protein expression, purification and sample preparation

Detailed information about the design and cloning process of the short *Thermosynechococcus elongatus* β -barrel construct (PsbO- β) can be found in Bommer *et al.*(64). A standard heat-shock protocol was used for the transformation of the PsbO- β construct in PET28a in *Escherichia Coli* BL21(DE3) cells. The cells were plated and grown over night at 37 °C on lysogeny broth (LB) agar with kanamycin (40 $\mu\text{g mL}^{-1}$). A LB preculture with kanamycin was then inoculated by the transformants (25 °C, 180 rpm, overnight). To obtain a uniform ^{13}C and ^{15}N labelling of PsbO- β the cells were centrifuged (10 min, 2000 g, RT) and the pellet was washed and resuspended in ^{13}C and ^{15}N M9 Medium (2 L). The cells were grown at 37 °C and 170 rpm, protein expression was induced with isopropyl β -D-thiogalactopyranoside (IPTG, 1 mM) when an OD_{600} of 0.4 was reached and cells were harvested after 5h.

After resuspending the cell pellets (2 g) in ice-cold 2-morpholin-4-ylethanesulfonic acid (MES) buffer (pH 6.6, 30 mM, 30 mL) with MgCl_2 (2 mM), HS nuclease (250 units μL^{-1} , 15 μl) was added and cells were disrupted by using a microfluidizer (15000 psi). To digest the DNA sufficiently the cell debris was spun down (30 min, 48000 g, 25 °C) and the supernatant was incubated for 4h at RT. As PsbO originates from a thermophilic cyanobacterium and thus exhibits a large heat stability, we could apply a purification protocol that includes an incubation step at 75 °C for 30 min. While most of the *E. Coli* proteins denatured and precipitated, PsbO remains in the supernatant after centrifugation (20 min, 48000 g, 8 °C)

Amicon Ultra 4ml filters with a molecular weight cut-off of 3kD were used to concentrate the supernatant to 1.2 mL, which were subsequently added through

a 0.45 μM filter onto a size exclusion chromatography column (120 mL Superdex 75). A MES buffer (pH 6.6, 30 mM) was used for the chromatographic purification. The fractions were analysed by SDS-PAGE and fractions containing PsbO were combined and concentrated to a final concentration of 35 mg mL⁻¹ by using an Amicon Ultra 4 mL filter (3 kDa MWCO).

The expression of uniformly ²H, ¹³C, ¹⁵N labelled PsbO- β was carried out as described in Marley *et al.* (102) with some adaptations. Cells were grown in a preculture in LB medium, pelleted, washed and resuspended in LB medium (1 L) as described above. When reaching an OD₆₀₀ of 1.0 the cells were harvested (2000 g, 15 min, RT) washed and resuspended in ²H, ¹³C and ¹⁵N M9 Medium (1 L). The induction of protein expression was started after 1h with IPTG. Cells were harvested after 5h (6000 rpm, 30 min, 4° C).

To use comparable amounts of PsbO- β in the NMR titration experiments the sample concentration was adjusted for each pH experiment to a final concentration between 9 and 14 mg mL⁻¹. The samples were dialysed over night to adjust the pH, which causes small differences in sample concentration. For the pH range between 5 and 8, a sodium phosphate buffer was used, for lower pH values 20 % phosphoric acid was added and for higher pH values 1 M NaOH was used. 10 % D₂O was added to all samples prior to the measurement of pH and final protein concentration. All samples were analysed by NMR immediately after the above-described preparation steps.

2.1.2 Recording of assignment and pK_a titration spectra

All NMR spectra were recorded on AV-III-600 spectrometers and with cryogenically cooled probes (Bruker Biospin, Karlsruhe, Germany) at 300 K. For the backbone assignment, 3D HNC(O), HNCaCb, HN(CO)CaCb and HN(COCaCb)Cg transverse relaxation optimised spectra (TROSY) were employed. The HNC(O) was acquired with spectral widths of 10 000 (¹H), 3012

(^{15}N) and 2500 Hz (^{13}C) in the direct and indirect dimensions, an acquisition time of 51 ms in F_3 (^1H), 15.9 ms in F_2 (^{15}N) and 19.2 ms in F_1 (^{13}C), four scans and 512x48x48 complex points. HNCaCb, HN(CO)CaCb, and HN(COCaCb)Cg were acquired with spectral widths of 10000 Hz (^1H), 3012 Hz (^{15}N) and 10000 Hz (^{13}C) in the direct and indirect dimensions, an acquisition time of 51 ms for Proton in F_3 , 16.6 ms for Nitrogen in F_2 and 5.5 ms for Carbon in F_1 , eight scans and 512x50x55 complex points. The 2D $^{15}\text{N}, ^1\text{H}$ HSQC spectra were acquired with spectral width of 10000 Hz in the direct dimension (^1H) and 3012 Hz in the indirect dimension (^{15}N). To obtain side chain assignments, three-dimensional CbCaCO spectra were recorded. They were acquired with spectral widths of 10000 Hz (^{13}C), 7042 Hz (^{13}C) and 10000 Hz (^{13}C) in the direct and indirect dimensions, an acquisition time of 51 ms in F_3 (^{13}C), 9.1 ms in F_2 (^{13}C) and 7 ms in F_1 (^{13}C), four scans and 512x64x70 complex points. All assignment related experiments were recorded with triply labelled protein (^2H , ^{13}C , ^{15}N).

For the titration experiments, two-dimensional CbCaCO spectra were acquired for 24h at each pH value. The spectral widths were 10000 Hz for the direct and indirect dimensions, the acquisition time was 51 ms in F_2 (^{13}C) and 6.4 ms in F_1 (^{13}C) and 220 scans and 512x64 points were used. In contrast to the assignment spectra, $^{13}\text{C}/^{15}\text{N}$ labelled PsbO was used for the titration and HSQC spectra. The processing was done using Bruker Topspin 3.2 software and the program CcpNmr Analysis 2.4 was used for the assignment of the protein.

2.1.3 ProPka prediction tool

ProPka is an empirical pK_a prediction tool based on the protein structure. Considered are electrostatic interactions such as hydrogen bonding, coulomb interactions and intrinsic electrostatics (i.e. van der Waals interactions) as well as desolvation effects (103–105). It is a fast method for pK_a prediction that has been constantly improved and is easily accessible via github and different servers.

We used the PDB2PQR (106) tool at the poissonboltzmann.org webserver to calculate the pK_a values of PDB file 5G39 at pH 6. PARSE (parameters for solvation energy) was chosen as forcefield and the additional options “remove waters from the output file”, “optimize the hydrogen bonding network” and “ensure that new atoms are not rebuilt too close to existing options” were activated.

2.1.4 Calculation of chemical shift perturbations (CSP)

Data for the CSP calculation was extracted from the pH dependent chemical shift differences of the two-dimensional ¹H, ¹⁵N HSQC spectra. We decided to only use spectra with pH values between 3.1 and 7.9 since most of the peaks were visible and trackable within this range. The CSP were calculated using the following equation:

$$CSP = \sqrt{[\Delta\delta(ppm)^{1H}]^2 + [0.156 \times \Delta\delta(ppm)^{15N}]^2} \quad (22)$$

This considers, that the chemical shift of the backbone ¹⁵N covers a broader range than the one of backbone ¹H, which is expressed in the factor of 0.156 (107).

2.2 Solid State and DNP experiments of Phytochrome Cph1Δ2

2.2.1 Expression and Purification of selectively labelled Cph1Δ2 phytochrome

We are working with a phytochrome-like Cph1Δ2 construct from cyanobacterium *Synechosystis sp. (strain PCC 6803)*, comprising the PAS/GAF/PHY domains of phytochrome. It is a 514 aa construct with a molecular mass of 60 kDa.

```

      10      20      30      40      50      60      70
MATTVQLSDQ SLRQLETLAI HTAHLIQPHG LVVVLQEPDL TISQISANCT GILGRSPEDL LGRTLGEVFD
      80      90     100     110     120     130     140
SFQIDPIQSR LTAGQISSLN PSKLWARVMG DDFVIFDGVF HRNSDGLLVC ELEPAYTSDN LPFLGFYHMA
      150     160     170     180     190     200     210
NAALNRLRQQ ANLRDFYDVI VEEVRRMTGF DRVMLYRFDE NNHGDVIAED KRDDMEPYLG LHYPESDIPQ
      220     230     240     250     260     270     280
PARRLFIHNP IRVIPDVYGV AVPLTPAVNP STNRAVDLTE SILRSAYHCH LTYLKNMGVG ASLTISLIKD
      290     300     310     320     330     340     350
GHLWGLIACH HQTPKVIPFE LRKACEFFGR VVFSNISAQE DTETFDYRVQ LAEHEAVLLD KMTTAADFVE
      360     370     380     390     400     410     420
GLTNHPDRLL GLTGSQGAAI CFGEKLILVG ETPDEKAVQY LLQWLENREV QDVFFTSLSL QIYPDAVNFK
      430     440     450     460     470     480     490
SVASGLLAIP IARHNFLWF RPEVLQTVNW GGDPNHAYEA TQEDGKIELH PRQSFDLWKE IVRLQSLPWQ
      500     510
SVEIQSALAL KKAIVNLILR QAEE

```

Cloning, expression and initial purification was done by Natalja Erdmann and Anne Diehl. Cph1Δ2 sequence in pSE 111 was transfected in *E. coli* BL21 DE3 cells using a standard heat shock protocol. A 400 ml preculture was grown overnight at 30 °C, 170 rpm on LB medium containing kanamycin (40 µg mL⁻¹) and carbenicillin (60 µg mL⁻¹). Cells were spun down (RT, 10 min, 2000 g) and resuspended in 2 L 2x M9 medium (D₂O, D7-glucose, ¹⁵N-NH₄Cl). Cells were grown for 5h at 37° C, 170 rpm before addition of 30 mg ¹⁵N, ¹³C labelled mix of arginine, isoleucine, tryptophan, and valine (4,57 mg/ml in D₂O). After 1h at 18 °C, 160 rpm, and an OD₆₀₀ of 0.6, protein expression was induced with 100 µM IPTG. During expression D7-glucose, ¹⁵NH₄Cl and ¹³C ¹⁵N labelled amino acid mix (115 mg total) were added when fully consumed, a lack of nutrients was detected by measuring glucose and ammonium chloride levels. Cells were harvested after 48 h at 18 °C, 160 rpm, washed in 150 mM NaCl and stored at -80°C.

The biomass was sent for the final purification steps such as chromophore binding (phycocyanobilin) and conversion into a distinct light-absorbing state to the group of Jon Hughes in Giessen. A uniformly ¹⁵N labelled and deuterated Cph1Δ2 sample with arginine, isoleucine, tryptophan and valine ¹H,¹³C and ¹⁵N labelled (WIRV) was assembled with ¹H PCB.

2.2.2 Preparation of proline standard and radical rotors

A 0.5 M stock solution of ^{15}N - ^{13}C proline in GDH (60 % glycerol/30 % D_2O /10 % H_2O) was prepared. M-TinyPol and bcTol-M were dissolved in GDH at 20 mM concentration. To fully dissolve, M-TinyPol was subjected to sonication for 10 minutes. To prepare the standard proline rotor, proline stock solution and GDH juice were mixed in a 1:1 ratio, 10 μl of this mixture were pipetted into a 1.9 mm rotor. For the radical containing samples bcTol-M and M-TinyPol were mixed each 1:1 with the proline stock solution and filled in two separate rotors. The final concentration of bcTol-M and M-TinyPol was 10 mM, proline concentration was 0.25 M and 10 μl were filled into each rotor. With this preparation all rotors should contain similar amounts of proline. The rotors were stored at - 20 °C before and after usage.

2.2.3 Preparation of Pr/Pfr-state Cph1 Δ 2 rotors

Before filling into the rotor, the Cph1 Δ 2 sample was irradiated with 730 nm red light for 1.5 h on ice. An UV-Vis spectrum was recorded with a Beckman DU520 spectrometer to review the conversion of the protein in the Pr-state. All following steps were executed under light exclusion.

15 mg of Cph1 Δ 2 in 50 mM Na/PO_4 buffer (pH 7.8, 20 % D_2O) were filled into 1.9- or 3.2-mm rotors via ultracentrifugation for 62-68 h, 4 °C, 71000 x g.

For the preparation of the DNP Cph1 Δ 2 samples, 40 mM bcTol-M and M-TinyPol stock solutions in GDH were made. M-TinyPol did not dissolve well until sonicated for 20 minutes. 2.2 μl of the respective radical solution were added to the ultra-centrifuged Cph1 Δ 2 rotor, leading to a final radical concentration of 10 mM and ~10 % glycerol. Rotors were stored at -20 °C in the dark.

To convert the packed sample into the Pfr state the rotor was opened and irradiated for 2h on ice with a 650 nm light source. The solution was stirred

periodically and conversion monitored by UV-Vis spectra. After closing the rotor under light irradiation, it was plunged frozen in liquid nitrogen and immediately inserted into the spectrometer.

2.2.4 Acquisition of DNP spectra

DNP spectra were recorded at Bruker 18.8 T (800 MHz) and 9.7 T (400 MHz) wide bore spectrometers with connected 527 GHz and 263 GHz gyrotrons, respectively. All spectra were recorded on triple resonance cryo-MAS probes with Avance III NMR consoles. At the field strength of 18.8 T, 1.9 mm zirconium rotors were used, spinning at $20 \text{ kHz} \pm 50 \text{ Hz}$ MAS if not stated otherwise, at 9.7 T 3.2 mm zirconium rotors were used, spinning at $8.89 \text{ kHz} \pm 50 \text{ Hz}$. A Bruker LT-MAS system provided cryogenic temperatures in the range of 100 - 110 K. Sample temperatures were determined using KBr- T_1 (108). As measured in previous works, we corrected the sample temperature with 6 - 7 K to a slightly higher temperature for samples when MW irradiation is turned on. Temperature equilibration after sample insertion was monitored with KBr, sample temperature was stable immediately after insertion. Turning MWs on was accompanied by a ten-minute sample equilibration period.

2.2.5 Characterization of bcTol-M and M-TinyPol at 18.8 T

One dimensional direct carbon excitation spin-echo spectra as well as hC-CP spectra were recorded for ten minutes signal-to-noise ratio measurements ($^{10\text{min}}\text{SNR}$) with a spectral width of 200 kHz. An optimal recycle delay of $1.3 \times {}^1\text{H-}T_1$ was used and the number of scans was adjusted accordingly to have a constant experiment time of $10 \text{ min} \pm 10 \text{ s}$.

Direct excitation spectra were recorded with an acquisition time of 10.2 ms, 4 dummy scans and 2048 complex points. A 78 kHz Spinal64 sequence was employed for heteronuclear decoupling during acquisition. hC-CP spectra were

recorded with an acquisition time of 5.1 ms, 4 dummy scans and 1024 complex points. The CP contact time was 2 ms for both samples, the amplitude of the ^1H spin-lock pulse was ramped from ~ 59 to ~ 74 kHz and the ^{13}C spin-lock rf-field was kept constant with 37 kHz and 43 kHz for bcTol-M and M-TinyPol, respectively. A 78 kHz Spinal64 heteronuclear decoupling was employed during acquisition. All spectra were processed using the same wave function (EM, LB = 100 Hz). A magnetic field range of from 799.867 MHz (18.787 T) to 800.621 MHz (18.804 T) was covered. The NMR magnet is equipped with sweep coils to change the field strength for matching the NMR and electron irradiation frequency. After changing the magnetic field value, the ^1H water signal was monitored until the drift of the signal was linear and considered neglectable. Depending on the strength of the applied current, the magnetic field was stable after 2 to 8 hours. The MW irradiation was controlled with a Bruker 9.7 T cryogen-free gyrotron operating at 527 GHz frequency. The collector current was set to 130 mA and measurements were started when this value was steadily reached. At the same time the cathode voltage was kept at 16400 V.

Enhancements can be calculated from the signal intensities by comparing spectra recorded under similar conditions but with and without MW irradiation, according to the following equation: $\varepsilon = \frac{I_{on}}{I_{off}}$. To account for the initial depolarisation and signal quenching, we additionally compared signal intensities of radical samples with a proline-only sample of similar concentration and solvent.

The determined enhancement factors give an initial hint of the quality of a PA, but to consider the different relaxation times and number of scans as well as DNP built-up times, the $^{10\text{min}}\text{SNR}$ was determined and the sensitivity factor κ calculated by the Ernst equation (109) as follows:

$$\kappa = \frac{^{10\text{min}}\text{SNR}}{c \cdot \sqrt{nS \cdot 1.3 \cdot ^1H - T_1}} \quad (23)$$

Here c is the radical concentration, ns the number of scans and ${}^1\text{H-T}_1$ the longitudinal relaxation time. ${}^1\text{H-T}_1$ times were determined for each field value with and without MW irradiation at a time, using an inversion recovery experiment. The ${}^{10\text{min}}\text{SNR}$ of the carbon direct-excitation spectra was determined for the ring carbon resonances $C_\alpha - C_\delta$ in the range from 10 to 73 ppm in the MW off spectra (11 to 81 ppm with MW on). The noise region was chosen from -287 to -350 ppm for the MW-off spectrum (-280 to -350 ppm for the MW on spectrum). The signal to noise ratio was then calculated within the Topspin 4.1.3 software. The proper definition of a noise region was not possible for the MW irradiated hC-CP spectra, as signals were covering the whole spectral width. We nevertheless calculated the ${}^{10\text{min}}\text{SNR}$ for the hC-CP spectra of bcTol-M and M-TinyPol. We defined the signal region from 10-85 ppm for the bcTol-M sample and 6.5-84 ppm for M-TinyPol. The noise region was chosen from 500-575 ppm for bcTol-M and 500-577.5 ppm for M-TinyPol.

We further calculated the reduced Boltzmann enhancement $\varepsilon_B = \frac{I_{\text{on}}}{I_{\text{off}}} \varepsilon_{\text{depo}}$, where ε_B considers the depolarisation and quenching effects of the employed PAs (given with 0.5 for bcTol-M (110) and 0.65 for M-TinyPol (111)). The enhancements were determined using the proline C_α peak.

2.2.6 Acquisition of DNP assignment spectra

For the assignment of the residues within the ‘tongue’ region we recorded carbon detected 3-dimensional hCaNCOCa spectra with 16 scans, 16 dummy scans and 512x48x96 complex points. Acquisition times were 6 ms in F1 (${}^{13}\text{C}$), 7.2 ms in F2 (${}^{15}\text{N}$) and 8.3 ms in F3 (${}^{13}\text{C}$), respective spectral widths 8000 Hz (F1), 3333 Hz (F2) and 61729 Hz (F3). The recycle delay was set to 4 s. The pulse sequence is shown in Figure 14. All parameter used for the two different samples, Pr and Pfr Cph1Δ2, can be found in Table 2.

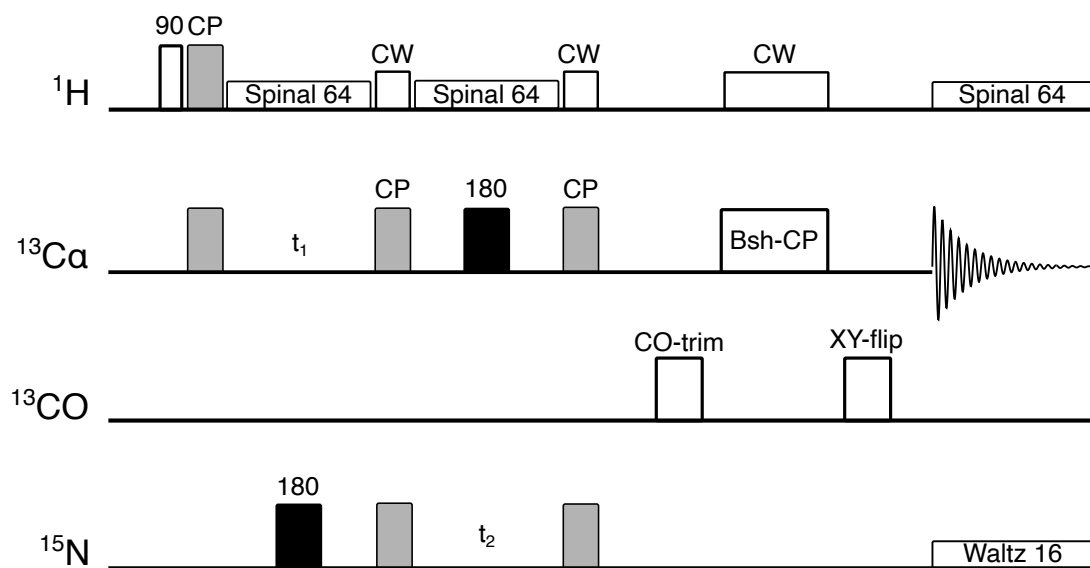


Figure 14: $hCaNCOCa$ pulse sequence. 90-degree pulse in white, CP pulses in grey and 180-degree pulses in black. CW proton decoupling is used during CP and Spinal64 during t_1, t_2 and acquisition. CO-trim and XY-flip pulse are used to bring carbonyl magnetization along the Bsh-CP field and back onto the X-axis, respectively.

The CO-trim pulse, an 58° and 54° hard pulse for Pr and Pfr sample, is used to flip the CO magnetization along the Bsh-CP rf-field. The XY-flip, a 98° hard pulse, brings the carbonyls back to the X-axis shortly before detection. Both pulses are surrounding the band-selective homonuclear cross polarization (Bsh-CP) which is used for the CO-Ca transfer in this sequence (112).

Table 2: *hCaNCOCa pulse sequence parameter.*

Pulse sequence element	Parameter	Pr	Pfr
H-C CP	t (μs)	2250	2200
	^1H (kHz)	88	92.5
	^{13}C (kHz)	70-87 ramp80100	70-87 ramp80100
Ca-N CP	t (μs)	7500	6500
	^{13}C (kHz)	14-17 ramp4555	14-17 ramp4555
	^{15}N (kHz)	46	48
N-CO CP	t (μs)	6000	6000
	^{13}C (kHz)	22-31 ramp70100	22-31 ramp70100
	^{15}N (kHz)	46	49
Bsh-CP	t (μs)	7000	7000
	^{13}C (kHz)	15-12 ramp10080	15-12 10080
CO-trim	t (μs)	3.25	3
	^{13}C (kHz)	50	50
XY-flip	t (μs)	5.47	5.47
	^{13}C (kHz)	50	50
CW	^1H	103	100
Spinal64	^1H	91	92.5
Waltz16	^{15}N	2	2

Additionally, 3D hNCaCb spectra were recorded with 8 dummy scans, 16 scans and 1024x72x64 complex points. Acquisition times were 17.2 ms in F1 (^{13}C), 3.6 ms in F2 (^{13}C) and 12.8 ms in F3 (^{15}N), respective spectral widths 2500 Hz (F1), 10000 Hz (F2) and 59524 Hz (F3). For the initial HN CP a constant ^1H rf-field of 64 kHz (69 kHz for Pfr) was applied, the rf-field on ^{15}N was ramped from 46 – 51 kHz (49 – 55 kHz for Pfr), the contact time was 400 μs (600 μs for Pfr). The NCa SPECIFIC CP(113) contact time was 5500 μs (7000 μs for Pfr), a constant rf-field of 48 kHz (51 kHz for Pfr) was applied on ^{15}N while the ^{13}C rf-field was ramped from 22 – 31 kHz. The DREAM(114) transfer contact time was 1800 μs (1700 μs for Pfr) the ^{13}C rf-field was ramped down from 10 – 8 kHz. ^1H CW decoupling between 90 and 105 kHz was applied during the CP transfers and 90 – 95 kHz ^1H Spinal64 decoupling was used during acquisition times. The

recycle delay was set to 4 s. The origin of slightly higher rf-fields required for the Pfr sample could be due to a modification of the hardware, as the probe unfortunately had been sent in for repair after the initial measurements on the Pr sample.

For the evaluation of the 3D spectra the CcpNmr Analysis Version 2 (115) Software was used.

2.2.7 Acquisition of DQ-SQ spectra

Incredible natural-abundance double-quantum transfer experiment (INADEQUATE) type spectra (116) with an SPC5 sequence (117) and cross polarisation were recorded to generate double quantum - single quantum (DQ-SQ) correlations. The pulse sequence is shown in Figure 15. The spectra were run with 15 composite SPC5 cycles, 8 dummy scans, 16 scans and 512x1048 complex points. Acquisition times were 6.4 ms in F1 (^{13}C) and 8.3 ms in F2 (^{13}C), respective spectral widths were 80000 Hz in F1 and 61728 Hz in F2. The CP contact time was 2.25 ms, the ^1H spin-lock rf-field was kept constant at 88 kHz and ^{13}C spin-lock pulse was ramped from ~ 70 to ~ 87 kHz. During acquisition 100 kHz Spinal64 heteronuclear decoupling was applied. The recycle delay was set to 4 s.

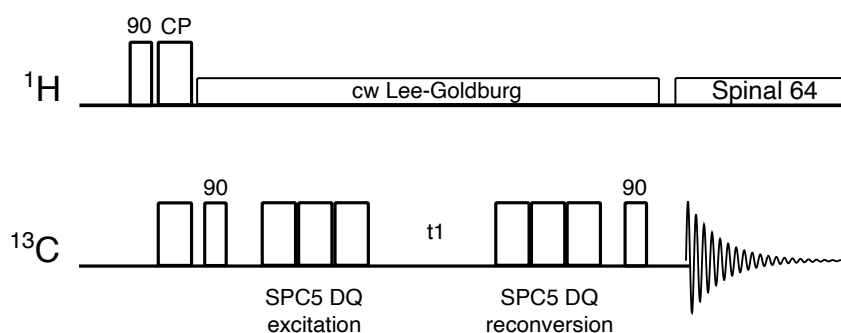


Figure 15: SCP5 pulse sequence used for the acquisition of carbon DQ-SQ spectra.

2.2.8 Acquisition of 1D hC-CP and 2D CC-DARR spectra for temperature comparison

A temperature dependence of the phycocyanobilin chromophore carbon signals was observed at the 800 MHz spectrometer with the 1.9 mm DNP probe and LT-MAS unit setup. Therefore, a sample with unlabelled Cph1 Δ 2 and uniformly ^{13}C -labelled phycocyanobilin was used. Temperatures compared were 291 K, 276 K, 261 K, 247 K and 229 K. CP conditions were similar for spectra recorded at temperatures from 276 K to 229 K. 1D hC-CP spectra were recorded with 1536 complex points, 16324 scans, an ^{13}C acquisition time of 15 ms and a spectral width of 81.5 kHz. A constant ^1H rf-field of 80 kHz was applied while the ^{13}C spin-lock pulse was ramped from 40 to 50 kHz. The CP contact time was set to 2000 μs . At 291 K a constant ^1H rf-field of 95 kHz was applied, ^{13}C spin-lock pulse and CP contact time were the same as for the lower temperature measurements. During acquisition 100 kHz Spinal64 proton decoupling was applied. The recycle delay was set to 2 ms.

A 2D carbon-carbon correlation (2D CC-DARR) was recorded at 264 K with 2048x160 complex points and 512 scans. Acquisition times were 2 ms in F1 (^{13}C) and 34 ms in F2 (^{13}C) respective spectral widths were 40000 Hz in F1 and 59523 Hz in F2. A constant ^1H rf-field of 75 kHz was applied while the ^{13}C spin-lock pulse was ramped from 40 to 50 kHz. The CP contact time was set to 1 ms. The DARR mixing time was set to 200 ms and ^1H DARR irradiation applied during mixing was 20 kHz. During acquisition, 73 kHz Spinal64 proton decoupling was applied. The recycle delay was set to 2 ms.

3 Results and Discussion

Figure 17 displays the backbone walk for residues Asp90 to Glu98. The 2-dimensional (^2D) ^1H ^{13}C strips are sections of ^{15}N planes extracted at different ^{15}N chemical shifts, which are indicated on the top of the strip. The $^{13}\text{C}_\alpha$ signals are positive, whereas the $^{13}\text{C}_\beta$ are negative, which is indicated with different colours: blue and rose in the HNCaCb spectrum and green and red in the $\text{HN}(\text{CO})\text{CaCb}$ spectrum, for positive and negative signals, respectively. The peaks connecting two sequential residues are linked with dotted lines.

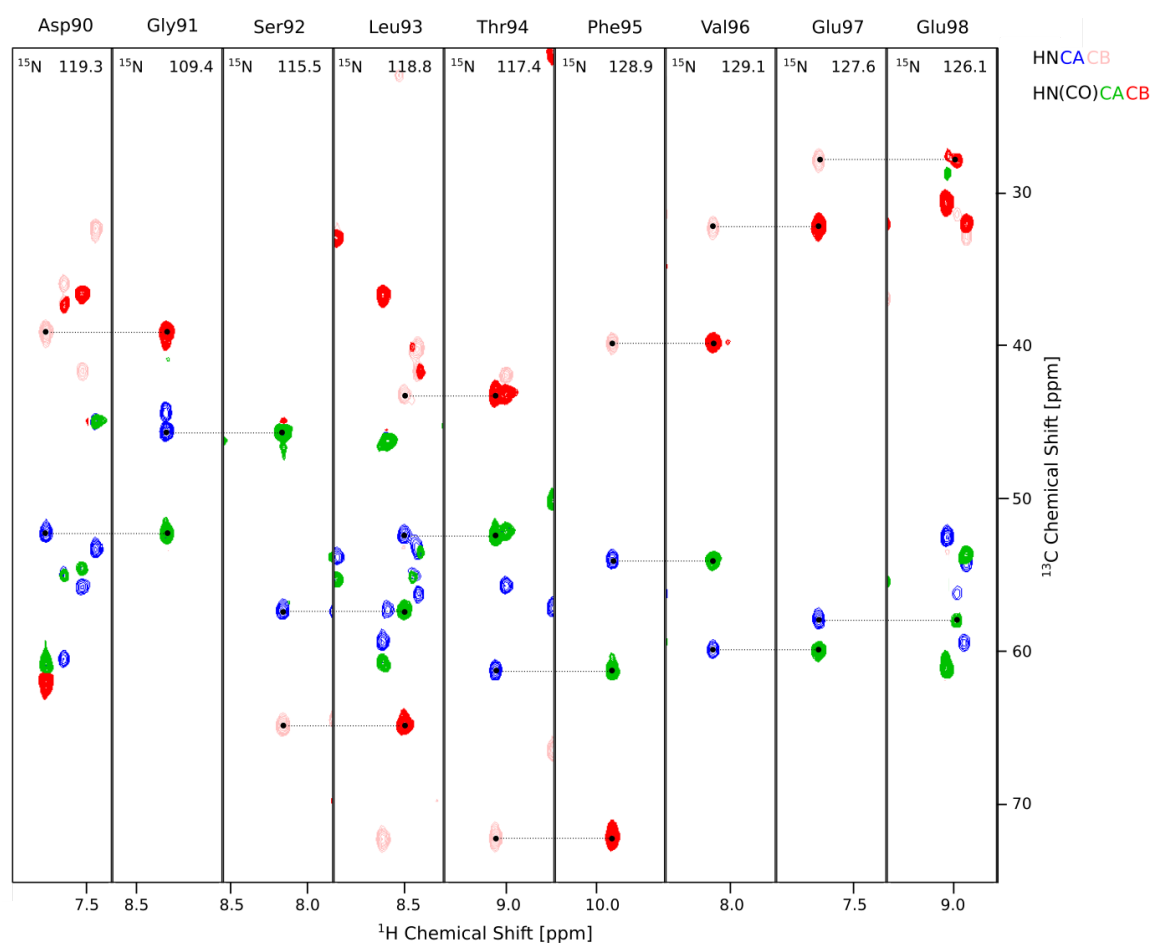


Figure 17: Backbone walk. Strip plots of 3-dimensional (3D) HNCaCb with peaks in blue ($^{13}\text{C}_\alpha$) and rose ($^{13}\text{C}_\beta$) and $\text{HN}(\text{CO})\text{CaCb}$ with peaks in green ($^{13}\text{C}_\alpha$) and red ($^{13}\text{C}_\beta$), extracted from spectra recorded on $\text{PsbO-}\beta$. The strips are aligned and illustrate the backbone assignments for residues Asp90-Glu98. Aligned resonances are connected with dotted lines.

For the assignment of the side chain carbon chemical shifts of glutamate and aspartate residues, ^{13}C -detected 3D CbCaCO experiments were employed. To be able to distinguish between side chain and backbone CO resonances, in particular for aspartates, backbone HNCO spectra were analysed in parallel for comparison. In this

way we were able to assign all 9 aspartate and 12 of the 13 glutamate side chain carboxyl groups unambiguously (see Figure 18). The sole exception with no carboxyl peaks assigned is Glu97.

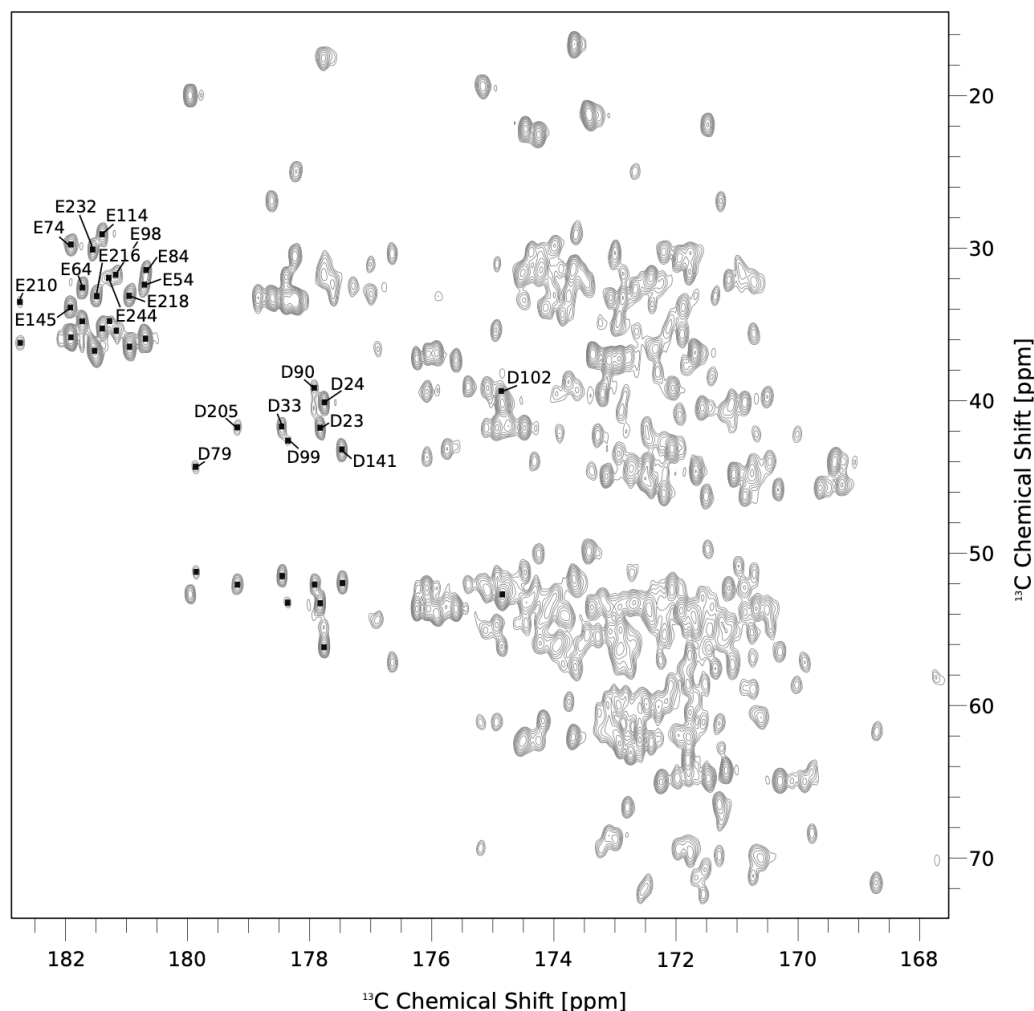


Figure 18: 2D projection of the 3D CbCaCO spectrum recorded at pH 6.6. The assignments are indicated for the glutamate $^{13}\text{C}_\beta$ - $^{13}\text{C}_\delta$ and aspartate $^{13}\text{C}_\beta$ - $^{13}\text{C}_\gamma$ cross peaks. Resonances marked with squares but without assignment are the corresponding glutamate $^{13}\text{C}_\gamma$ - $^{13}\text{C}_\delta$ and aspartate $^{13}\text{C}_\alpha$ - $^{13}\text{C}_\gamma$ peaks.

Figure 18 shows the 2D CC projection of the 3D CbCaCO spectrum recorded at pH 6.6. The annotated peaks are glutamate $^{13}\text{C}_\beta$ - $^{13}\text{C}_\delta$ and aspartate $^{13}\text{C}_\beta$ - $^{13}\text{C}_\gamma$ cross correlations, whereas the cross peaks marked with a square but no assignment represent glutamate $^{13}\text{C}_\gamma$ - $^{13}\text{C}_\delta$ and aspartate $^{13}\text{C}_\alpha$ - $^{13}\text{C}_\gamma$ cross correlations. The sidechain carboxyl peaks, with Asp102 being the only exception, have chemical shifts separated from the bulk of backbone ^{13}CO resonances, which simplifies their assignment. Using the 2D version of this type of spectrum in the titration experiment,

we can follow the chemical shifts changes of one carboxyl group with two distinct but coupled peaks that should shift uniformly upon pH changes. This is particularly helpful in ambiguous cases when peaks migrate into crowded areas with high peak overlap.

3.1.2 pK_a values of glutamic and aspartic acid carboxylate groups scatter widely around the model values

Proton affinities were determined by monitoring the $^{13}\text{C}_\gamma$ and $^{13}\text{C}_\delta$ chemical shifts of aspartate and glutamate residues, respectively. Therefore, 2D CbCaCO experiments were recorded at different pH values ranging from pH 1.6 to 11 and the chemical shift changes of the carboxyl carbon atoms were observed. The corresponding cross-peaks were well resolved which allowed for a precise interpretation of the chemical shift changes upon pH titration. An example is shown in Figure 19A, that depicts the change of the chemical shift of the $^{13}\text{C}_\gamma$ cross-peaks of aspartate residue 141(134) during the pH titration from 7.6 to 5.8 as indicated by the black arrow. Values within brackets indicate the amino acid numbering of the short construct. The $^{13}\text{C}_\beta$ chemical shift changes are rather small and can generally be neglected, and they will not be considered in the determination of pK_a values. They rather exemplify of how far the effect of de-/protonation events extends to the backbone and translates into chemical shift changes.

The chemical shift changes of 21 glutamic and aspartic residues were observed and translated into titration curves (see Figure 19C and D). The Henderson-Hasselbalch equation fits reasonably well for most of the titration curves, see for example Asp23(23) and Asp141(134). We therefore determined the pK_a values for a one-step proton-exchange mechanism using a nonlinear least-squares fit function. The resulting pK_a values are listed in

Table 3.

However, it turned out that this fitting function could less accurately describe the titration curves of some residues, Glu210(160), Glu218(169), Glu232(176) and Asp205(156). The experimental data deviates from the fit function primarily around the inflection point, which is an indication for the participation of additional sites at the proton exchange mechanism. A two-step exchange mechanism could be more suitable to describe the protonation process. When looking at the protein structure we can see that these specific residues are part of two clusters with shared protons through bifurcated hydrogen bonds. These clusters are formed by the residues Asp23(23)/Glu210(161)/Asp205(156) and Glu216(167)/Glu218(169)/Glu232(176) and could be the underlying reason for the deviations from the fit function (Figure 19B).

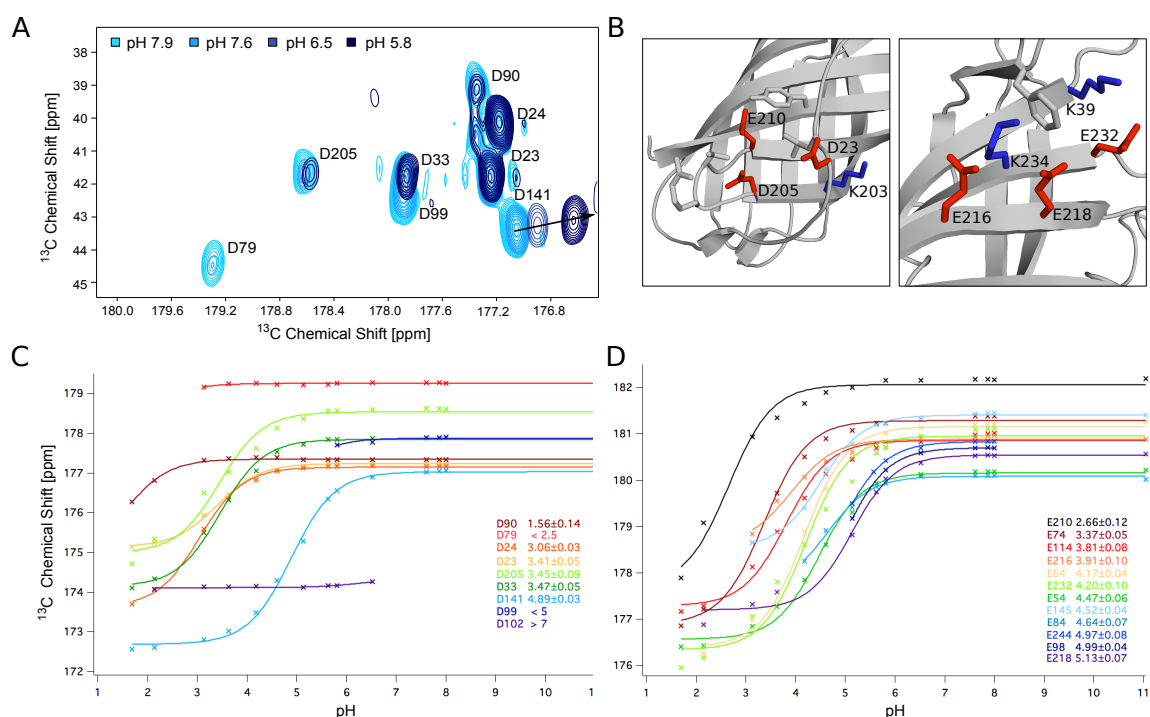


Figure 19: Titration experiments and analysis. (A) Cut-out of the 2D (CbCa)CO spectrum at different pH values from pH 5.8 (dark blue) to pH 7.9 (light blue). The black arrow indicates the shift of side chain carboxylate carbon of Asp141. (B) Side chain conformation of residues with titration curves that deviate from the Henderson-Hasselbalch fit shown on crystal structure of PsbO- β . (C) Titration curves of aspartic acid residues and corresponding pK_a values, errors are given as 95% confidence intervals. Curves are color-coded from high pK_a values in red to low pK_a values in blue. (D) Titration curves of glutamic acid residues and corresponding pK_a values, errors are given as 95% confidence intervals. Curves are color-coded from high pK_a values in red to low pK_a values in blue.

Apart from deviations from the fit function, a second complication for the determination of pK_a values are caused by spectral regions with heavily overlapping or vanishing peaks. For example, the cross-peaks of Asp79(72), Asp99(92) and Asp102(95) move through crowded areas or even vanish at specific pH values. Therefore, some of the titration curves are incomplete and the particular pK_a values can only be assessed as upper or lower boundary.

The standard pK_a value for glutamic acid in solution is 4.25 ± 0.05 , and 3.67 ± 0.04 for aspartic acid (118). The majority of glutamate residues have pK_a values that clusters around this value, the two exceptions are Glu74(67) and Glu210(161) which show are more acidic pK_a values of 3.37 ± 0.05 and 2.66 ± 0.12 , respectively. The aspartic acid residues show a broader distribution, with only three values (Asp23, Asp33 and Asp205) around the standard pK_a .

Table 3: pK_a values of aspartic acid and glutamic acid residues.

Asp residue no.	pK_a value	ProPka prediction	Glu residue no.	pK_a value	ProPka prediction
23	3.41 ± 0.05	2.19 ± 0.79	54	4.47 ± 0.06	4.90 ± 0.79
24	3.06 ± 0.03	3.92 ± 0.79	64	4.17 ± 0.04	4.64 ± 0.79
33	3.47 ± 0.05	2.84 ± 0.79	74	3.37 ± 0.05	3.95 ± 0.79
79	<2.5	1.65 ± 0.79	84	4.64 ± 0.07	4.66 ± 0.79
90	1.56 ± 0.14	2.43 ± 0.79	98	4.99 ± 0.04	3.93 ± 0.79
99	<5	3.31 ± 0.79	114	3.81 ± 0.08	3.98 ± 0.79
102	>7	3.82 ± 0.79	145	4.52 ± 0.04	4.06 ± 0.79
141	4.89 ± 0.03	4.00 ± 0.79	210	2.66 ± 0.12	4.19 ± 0.79
205	3.45 ± 0.09	3.39 ± 0.79	216	3.91 ± 0.10	4.67 ± 0.79
			218	5.13 ± 0.07	4.84 ± 0.79
			232	4.20 ± 0.10	3.66 ± 0.79
			244	4.97 ± 0.08	-

We have compared our results to pK_a values obtained with a ProPka 3.0-based prediction tool. Overall, we observed a reasonable conformity between predicted and measured pK_a values. The largest deviations, with more than 1 pH unit, are found for Asp23, Asp102, Glu98 and Glu210. Interestingly, the ProPka software identified the two residues Asp102 and Glu97 as coupled residues. These are also the residues with the highest score of being buried (Asp102 with 29% and Glu97 with 39%). This might provide an explanation why we only could determine the pK_a value for Asp102 as greater than 7 and could not obtain any result for Glu97, for which the software predicts a pK_a of 7.03. They likely share a proton and titrate together.

3.1.3 Chemical shift perturbations of backbone amide groups reveal flexibility in the luminal part of the beta-barrel

We were able to determine the chemical shift perturbations (CSP) values upon titration for all residues that showed backbone $^1H^{15}N$ correlations in HSQC spectra at pH values between 2 and 8. The superposition of the titration spectra is presented in Figure 20.

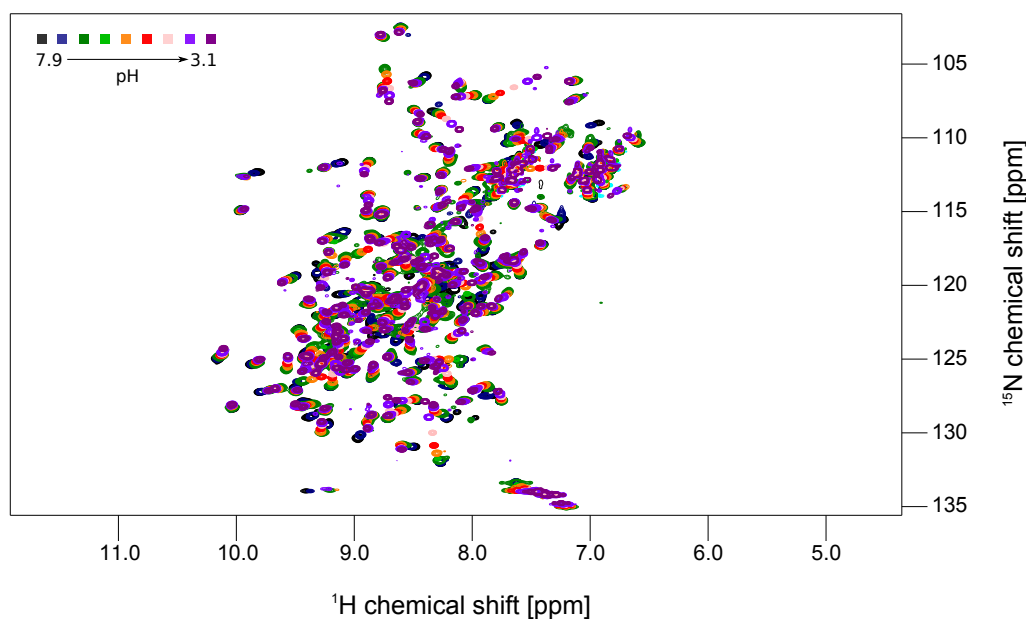


Figure 20: Superposition of ^{15}N - 1H HSQC titration spectra of PsbO- β recorded at pH values ranging from 7.9 in dark blue to 3.1 in purple.

The resulting CSP values are shown in Figure 21A. The cross peaks of the majority of residues displayed marginal changes between pH 2 and 8. However, for a small number of residues, a significant change upon titration was observed. The side chains of these residues are indicated on the X-ray structure of PsbO- β in Figure 21B. Residues with a CSP value higher than 0.2 are highlighted in dark blue, the ones with a CSP value between 0.17 and 0.2 in light blue. CSPs below 0.17 are considered as less significant and are not displayed. Looking at the overall distribution of the residues with strong shifts mapped on the structure, we observe a cluster on the loops of the luminal side of the barrel, with the largest effects observed for Glu114, Thr208 and Ala246. The latter residue is the C-terminal amino acid and thus has a less rigid backbone. Depicted in orange is the cyano-loop, a region conserved in cyanobacteria which mediates contacts between PSII dimers in the thylakoid membrane (119). Interestingly, this region is surrounded by residues with pH-sensitive backbone signals, hence conformational changes could modulate dimer contacts of PSII. A structural switch has been observed for the carboxylate dyad of residues Glu97 and Asp102 between pH 6 and 10, which should alter the protein backbone conformation in this region. Therefore, we would expect rigorous chemical shift changes for the backbone $^1\text{H}^{15}\text{N}$ correlations for this region. Surprisingly, we only observed an intermediate CSP value for Glu97, and Asp102 shows an even smaller CSP. However, a peak in the HSQC spectrum could unambiguously be assigned to Asp102 from pH 3.1 to 6.5. This leaves us with the possibility of Asp102 showing a moderate chemical shift change in this range and altering its position after the deprotonation at pH values higher than 6. This in turn would result in a large chemical shift change which is not traceable in the titration spectra. We notice that the PsbO remains folded over the course of the pK_a titration as we see a broad chemical shift distribution typical for a folded protein for all pH values measured. The beta-barrel is relatively rigid

and rather pH insensitive, whereas in the luminal loop region conformational rearrangements can be induced by pH changes.

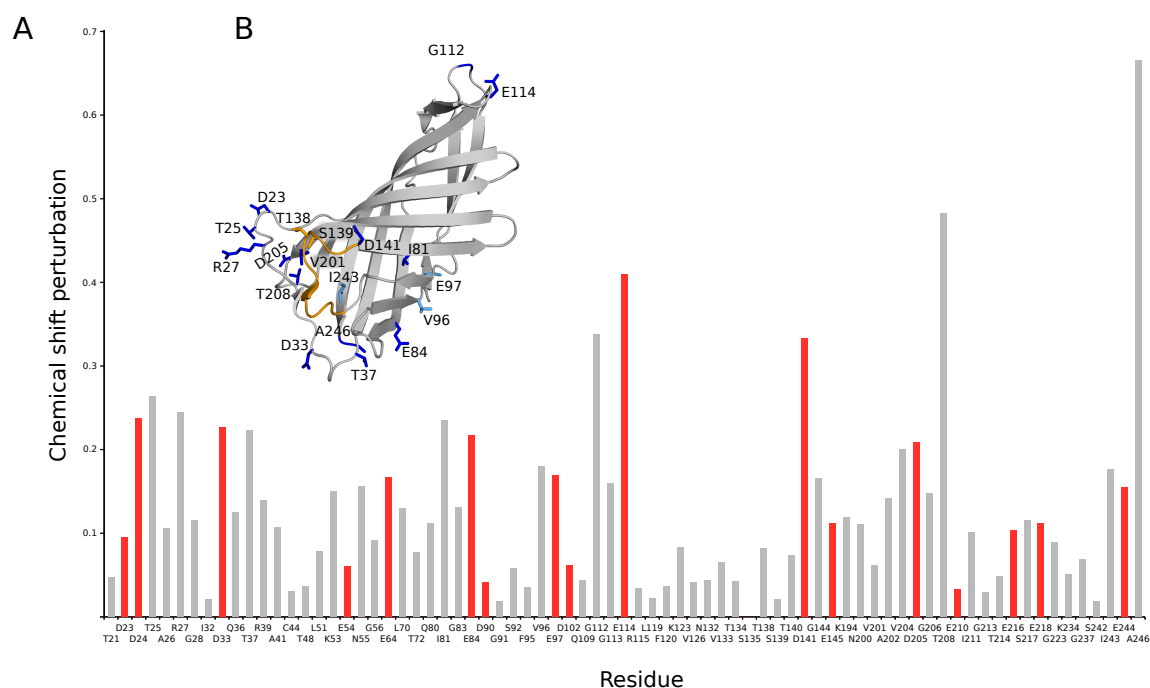


Figure 21: Chemical shift perturbations of PsbO backbone amide groups measured by 2D $^1\text{H}^{15}\text{N}$ correlation spectroscopy. (A) CSPs of all residues where data was assessable, acidic residues (Glu/Asp) are highlighted in red. CSP values were calculated according to the formula in the experimental section 2.1.4. Residues N55, G56 and G223 cannot be found in the original sequence of the long PsbO construct. They represent insertions that serve as loop replacements in PsbO- β . (B) Crystal structure of PsbO- β , the residues with the strongest CSP values colour-coded from high (>0.2 , dark blue) to intermediate values ($0.17 \leq \text{CSP} \leq 0.2$, light blue). In orange are residues that are part of the cyano-loop, T138 and S139 are involved in PSII dimer contacts and additionally depicted as sticks.

3.1.4 PsbO is equipped with a buffering capacity around pH 5 and pH-induced structural changes are accompanied by surface charge alterations

The pH of the thylakoid lumen has to be tightly controlled in the cells and is directly associated with the activity of PSII. A high proton motive force (PMF) needs to be established for ATP-synthesis to protect proteins from an acidic environment and to ensure for a functional photosynthesis.

High rates of photosynthesis can acidify the lumen towards a pH of 5. A drop below this value might inactivate the manganese complex and reduce the stability of PSII. Already at pH 4.6 the half-inhibition point of the water

oxidation reaction at PSII is reached (67), and values below will cause serious damage of the photosystem that can lead to its inactivation. On the other hand, a pH value higher than 5 is detrimental to the PMF. In that case, the transmembrane gradient would be reduced to a level that is too low to provide an adequate number of protons for ATP-synthesis. Taken together, this leaves only a small window for the luminal pH, hence it is obvious that photosynthetically active organisms need mechanisms to monitor and control the pH. PsbO is a suitable candidate to be part of this process, being favourably positioned within the PSII, with most of its beta barrel being exposed in the lumen and its loops (which are removed in our construct) reaching towards the OEC. While reaching far into the luminal space not all of the PsbO surface is solvent exposed. It interacts with PSII subunits CP43, CP47, D1, D2 and PsbU. Several charge-pair interactions have been proposed, particularly within the loops that have been cut in our sample, leaving the beta barrel with two interaction sites: residues Lys69 and Lys73 binding to D1 and Asp99 binding to CP43 (63). Besides the interaction with other subunits, PsbO exhibits contacts to its opposing PsbO unit, as was observed in a native-like dimeric PSII superstructure solved by X-ray. Residues Thr138 and Ser139 of the cyano-loop form hydrogen bonds to one another in the stacked crystal structure (119). For isolated proteins as observed in solution NMR, these interactions are not present but have to be considered when looking at the big picture.

We observed pK_a values on the surface of PsbO- β spanning a range from 1.56 to 5.13 and potentially even higher when we consider the pK_a value of Asp102 (>7), independent from the amino acid type. This is a surprisingly broad range compared to the standard values of 3.8 for aspartic acid and 4.25 for glutamic acid. In Figure 23C we present the distribution of pK_a values on the crystal structure of PsbO (PDB-ID: 5G39). The side chains of the negatively charged

residues are color-coded according to their pK_a values from low (dark red) to high (blue). When considering the orientation of PsbO within PSII (Figure 23D PDB-ID: 2AXT (120)) we observe a side specific distribution of pK_a values: in the lumen-exposed area of PsbO, residues with higher pK_a values are clustered, whereas at the part of PsbO facing PSII, we primarily find residues with lower pK_a values.

To be relevant for the buffering capacity in the thylakoid lumen the pK_a value of a residue has to be in the range from 4.3 to 5.1. Our studies show that eight of the 22 side chain carboxylate groups of the PsbO- β construct have pK_a values in this range. Most of them are located at the side which reaches into the lumen and is solvent accessible (Figure 23C and D). Considering the total protein density in and the size of the luminal space, PsbO- β with only eight carboxylate groups with suitable pK_a values has only a limited buffering capacity. Nevertheless, the localisation of these groups close to the potential proton release site is ideally suited for being part of a fast-acting regulation mechanism. In this way, these carboxylates would serve to bypass the initial seconds during luminal acidification before the activity of PSII is downregulated through the NPQ mechanisms.

To characterize PsbO's overall buffering capability we composed a mean value of all titration curves. The resulting curve was less steep around the inflection point at 4.1, which reflects an elongated transition from deprotonated to protonated state. The overall pK_a value of PsbO- β is thus below the pH of the thylakoid lumen. The titration curve is shown in Figure 22.

The pK_a values also reflect the electrostatic interactions of the surface of PsbO. In Figure 23A, a PsbO dimer extracted from the crystal structure of native-like PSII (PDB-ID: 4PJ0 (119)) is shown, with the surface charge-distribution color-coded from negative (red) to positive (blue) at pH 7.

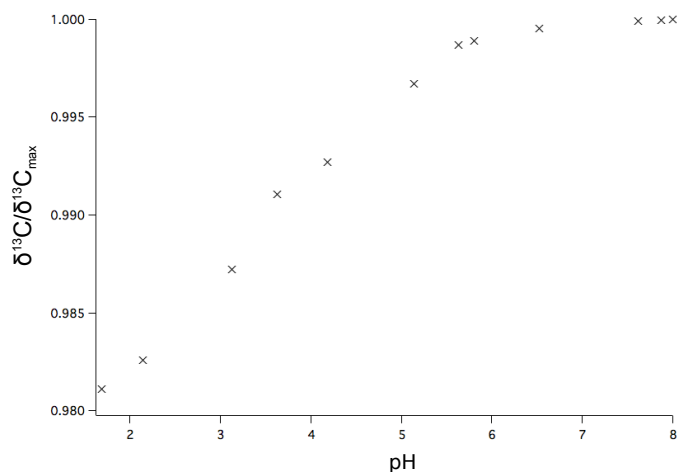


Figure 22: Overall pK_a titration curve of PsbO shows an inflection-point at 4.1.

From the top panel we can conclude that the interaction sites between the two PsbO units are small. A band of negative potential is created by residues Asp24, Asp23, Asp10, Asp205, Asp244 and Glu84 and forms a hemicycle around the dimer. Asp99, Glu98, Glu97 and Asp102 constitute a second band of negative potential that converges transversely towards the first band at residue Glu84. The negatively charged residues are - with the exception of Glu97 and Asp102, which are partially buried - exposed to the thylakoid lumen and none of them is interacting directly with other PSII subunits. Interestingly the residues of the two bands differ in their proton affinity. Asp24, Asp23, Glu210 and Glu205 have pK_a values that are between 2 and 4, they remain deprotonated independent from the PSII activity. Whereas the negative band including residues Asp99, Glu98, Glu97 and Asp102 show pK_a values just below 5 with Asp102 >7 being the exception. At pH values between 4.5 and 5 these residues become protonated which is accompanied by a change in surface charge. This band includes the residues of the carboxylate dyad (Glu97 and Asp102), that supposedly undergo a pH induced structural switch, which the change of surface charge distribution might promote. When comparing these results with the CSP data (see Figure 21), it is remarkable that the pH-dependent changes of backbone chemical shifts cluster in the luminal loop region that includes the negative band around the

carboxylate dyad, with residues Glu84, Val96 and Glu97 showing the largest CSPs.

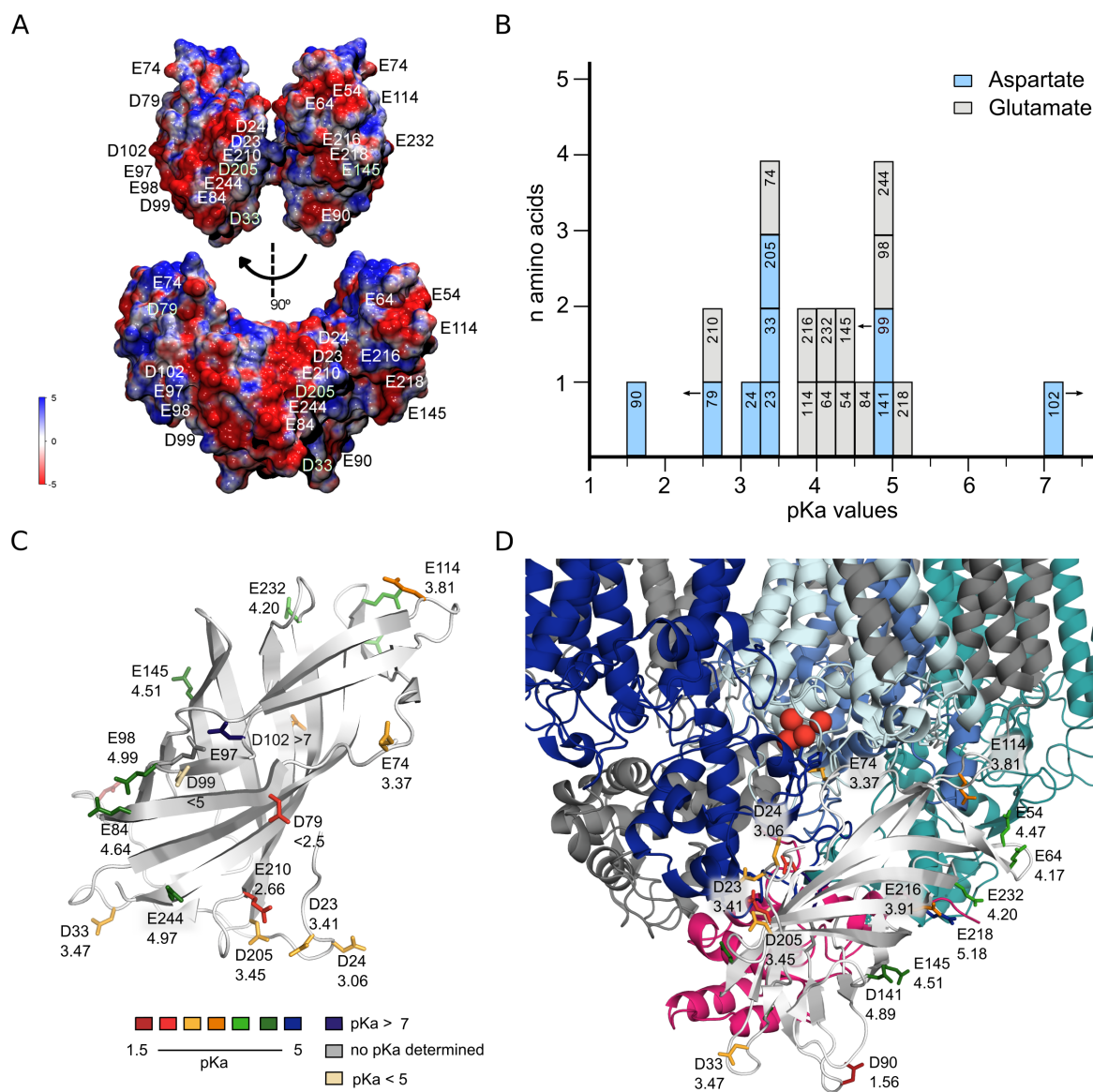


Figure 23: Electrostatic properties and distribution of pK_a values of $PsbO-\beta$ in the context of PSII. (A) The electrostatic potentials of the amino acid residues are plotted onto the surface of a dimeric structure of $PsbO-\beta$, which was created using van der Waals distances. The potentials are color-coded from negative (red) to positive (blue) at pH 7. (B) Distribution of pK_a values presented as histogram with the pK_a axis divided into units of 0.25. Aspartic acid residues are shown in blue glutamic acid residues in grey. Residues with arrows have pK_a values determined as upper or lower boundaries. Direction of the arrow indicates if these values are above or below the given pK_a . (C) Crystal structure of $PsbO-\beta$ (PDB-ID:5G39 (64)) depicted in light grey, side chain of glutamic acid and aspartic acid residues are shown as sticks color-coded according to their pK_a value. (D) Section of $PsbO-\beta$ (PDB-ID 5G38, light grey) in complex with PSII (PDB-ID: 2AXT (120)). Associated proteins D1 shown in pale blue, D2 in blue, CP43 in dark blue, CP47 in turquoise and PsbU in pink. OEC presented as red spheres. Residue numbers in this figure are according to the full-length construct of $PsbO$.

Changes in the backbone chemical shifts are a sign of structural rearrangements. Residues with strong CSP values accumulate predominantly in the loops and at beta-strand endings of the PsbO-barrel that are exposed to the lumen (Figure 21B). In this part we also find interaction sites with other PSII subunits, for example PsbU, hence it is conceivable that the structural changes modulate PsbOs interaction within the PSII system.

Unfortunately, we cannot study the function of PsbO in the context of a proton exit or water substrate pathway since we are missing essential residues, in this case Asp224 which is supposed to be a proton acceptor in the 'Cl-1 path'. This path is one of the four hydrogen-bond networks around the OEC involved in the evacuation of protons from the active centre (121). In our construct the loop which harbours Asp224 has been replaced by a short NG turn. We refrained from working with the full-length protein because the extended loop regions in the native protein are not stabilized by contacts with PSII subunits when working with the isolated protein in solution. This missing stability generates a high flexibility within these regions which would lead to signal loss in the NMR experiments. A suitable, though more complicated way to study the loop regions explicitly would be the analysis of fl-PsbO in PSII by solid-state NMR.

3.2. Defining NMR measurement conditions for Cph1Δ2

Different approaches exist to study proteins by NMR and the choice of a particular method largely depends on the sample condition. Small soluble proteins are usually studied with solution NMR methods. With the application of temperatures below the freezing point and/or protein sedimentation, ssNMR approaches become employable, especially when proteins are large (> 40 kDa). Microcrystals can also be studied by ssNMR, the sole prerequisite is the effective crystallization of the sample. It is thus relevant to determine the optimal measurement conditions for every individual biological system.

In this work we study the phytochrome Cph1Δ2 and the interaction with its chromophore phycocyanobilin (PCB, see Figure 25), and address the question if the ‘tongue’ region of the protein changes its secondary structure during photo-conversion. Since the phytochrome is a soluble protein, it would be intuitive to use a solution NMR approach. While different phytochromes have already been studied in solution (95,122,123), the Cph1Δ2 construct studied here (59 kDa) is at the upper size limit for solution NMR spectroscopy. Gustavsson *et al.* (123) have tried to observe the structural transition of the ‘tongue’ region in bacteriophytochrome *DrBphP*, but the NMR signals of this region have only been assigned in the Pfr state. Signals of the ‘tongue’ region in the Pr state could not be identified, which has been attributed to peak broadening due to structural heterogeneity of this region. Strauss *et al.* have as well observed peak broadening by chemical exchange in solution NMR, looking at carbon and nitrogen resonances of PCB in Cph1 (95). Cryogenic temperatures could be beneficial when working with phytochrome solutions to reduce protein dynamics and molecular motions. At temperatures between 100 and 200 K, protein dynamics are dominated by methyl group motions (124), whereas chemical exchange between different protein conformers is expected to become slow on the time

scale of measurement. In addition, at temperatures around 110 K, the protein can be maintained in a defined state (Pr or Pfr) over the course of measurement, as thermal reversion is slowed down and light-induced photo-conversion is prevented. In this study, a combination of sedimentation NMR (sedNMR) and high-field DNP is applied to study Cph1Δ2 in the Pr and Pfr state.

3.2.1 Phycocyanobilin ¹³C resonances are not subject to chemical exchange processes at 800 MHz and the application of sedNMR is optimal at 261 K

When investigating a soluble protein by ssNMR, cross-polarisation processes can only be successfully applied if the sample is immobilized to a large extent. One way to immobilize a soluble protein is by use of sedimentation NMR. Moreover, by using a combination of *ex situ* and *in situ* sedimentation, we can achieve a high protein concentration within the rotor. This is particularly important with regard to the low molecular weight-ratio of chromophore-to-protein (1:100) which generally impedes detection of chromophore resonances with a reasonable signal-to-noise ratio. Being interested in the phycocyanobilin (PCB) chromophore structure and its interactions within the binding pocket, it is useful to assess chemical exchange processes which would impede the observation of interactions. In the Cph1Δ2 sample only four types of amino acids (arginine, isoleucine, tryptophan and valine) are ¹³C labelled. Important contacts which can be monitored using this labelling pattern cover the interaction between R254 and the propionic acid group of PCB ring B, as well as the cooperative action of R222 and H260, two residues that are supposed to fix one or both propionic acid chains, supposedly in combination with water (89). The question whether these contacts remain in both the Pr and Pfr states, and which impact the ring D flip has on the residues and water molecules of the binding pocket will be addressed by ssNMR and DNP.

Previous DNP NMR measurements investigating the chromophore structure in the binding pocket of Pr have been performed at a relatively low field of 400 MHz (97). However, when trying to reproduce the results at a higher field of 800 MHz using similar conditions as the data recorded at 400 MHz, we were unfortunately not able to observe the peaks that have been assigned previously to PCB in a ^{13}C - ^{13}C correlation spectrum (see Figure 24).

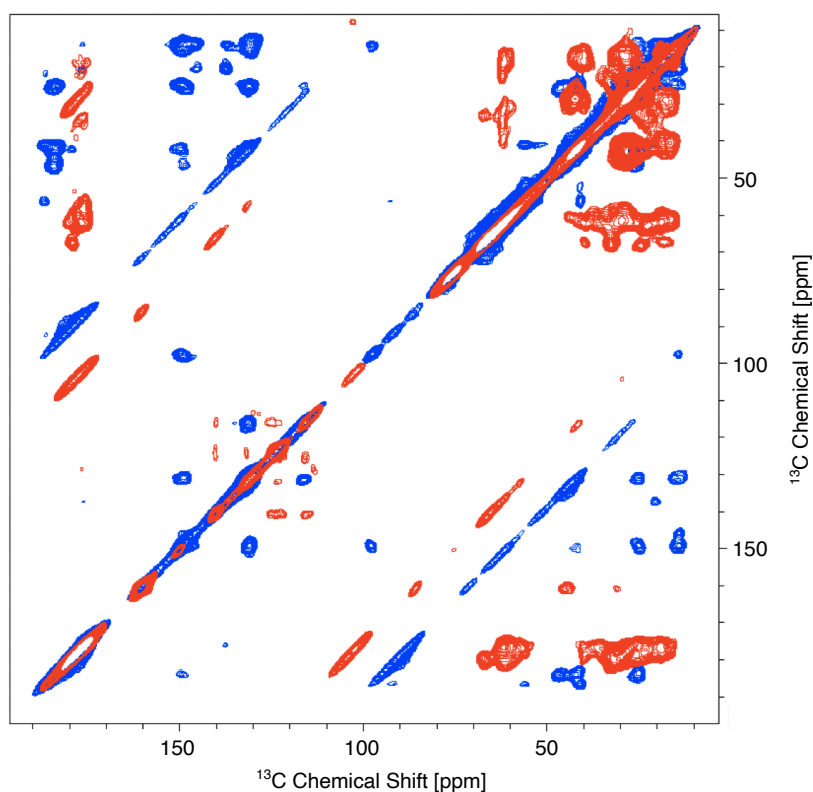


Figure 24: Comparison of Cph1 Δ 2 u- ^{13}C , ^{15}N]-PCB at 400 MHz in blue and selectively ^{13}C -WIRV u- ^{15}N labelled Cph1 Δ 2 u- ^{13}C , ^{15}N]-PCB at 800 MHz in red. Both spectra were DNP enhanced with bcTol-M serving as polarising agent. The spectra differ in DARR mixing time (25ms blue and 50 ms red).

The blue spectrum shows a ^{13}C - ^{13}C correlation of u- ^{13}C , ^{15}N]-PCB at 400 MHz within non-labelled Cph1 Δ 2, and the red spectrum a ^{13}C - ^{13}C correlation of u- ^{13}C , ^{15}N]-PCB within a ^{13}C WIRV, u- ^{15}N labelled Cph1 Δ 2 sample. We assume line broadening due to chemical exchange is causing the disappearance of the chromophore peaks at 800 MHz.

In the Pr state of Cph1 Δ 2, chemical exchange processes of the PCB chromophore have initially been observed by solution (95) and solid-state NMR (125). While

the solid-state study exclusively focussed on 1D ^{15}N spectra, line broadening effects have been observed in solution NMR 2D ^{13}C HMQC spectra. The latter spectra indicate a varying relaxation behaviour of the methyl group signals, to which local dynamics at their sites, and conformational exchange processes may contribute. These spectral observations can be explained by a certain mobility of the PCB chromophore in its binding pocket when the phytochrome is in the Pr state. While there is data from Raman spectroscopy suggesting a homogeneous Pr state of Cph1 Δ 2 (126), in the majority of phytochrome studies a heterogeneous Pr state is assumed (78,127,128). Song *et al.* describe in their solution NMR study two Pr states that show differences in proton contacts between chromophore and residue H260 and water molecules of the binding pocket (78). Hence, the chromophore appears to be not tightly fixed in its binding pocket, which leaves space for local motions. Structural heterogeneity of the phytochrome protein and chromophore could lead to line broadening due to exchange processes at reaction rates which are unfavourable at 800 MHz as compared to 400 MHz. We thus recorded 1D hC-CP spectra of PCB within Cph1 Δ 2 at different temperatures and 800 MHz field strength to characterize the assumed chemical exchange process, and to find suitable measurement conditions for the investigation of chromophore-protein contacts. In Figure 25, a 1D hC-CP spectrum of non-labelled Cph1 Δ 2 with u- $^{13}\text{C},^{15}\text{N}$ -labelled PCB is displayed. The chromophore ^{13}C resonances have been assigned according to Rohmer *et al.* (129), the skeletal formula of PCB is consecutively numbered just like the corresponding peaks in the spectrum. Even though the protein was initially in the Pr state, we observe peaks in the region of the methine carbon atoms (85-100 ppm), that are assigned to the Pfr state. This indicates an ongoing photo-conversion in the sample, likely induced by the standard MAS detector integrated in the probe

(maximum emission at 650 nm). This detector was replaced by an infrared detector for subsequent measurements (maximum emission at 950 nm).

The methine region is of special importance because there is no signal overlap from protein resonances: Even though the Cph1Δ2 itself is not labelled, we still observe background signals that originate from natural abundant ^{13}C nuclei in the protein.

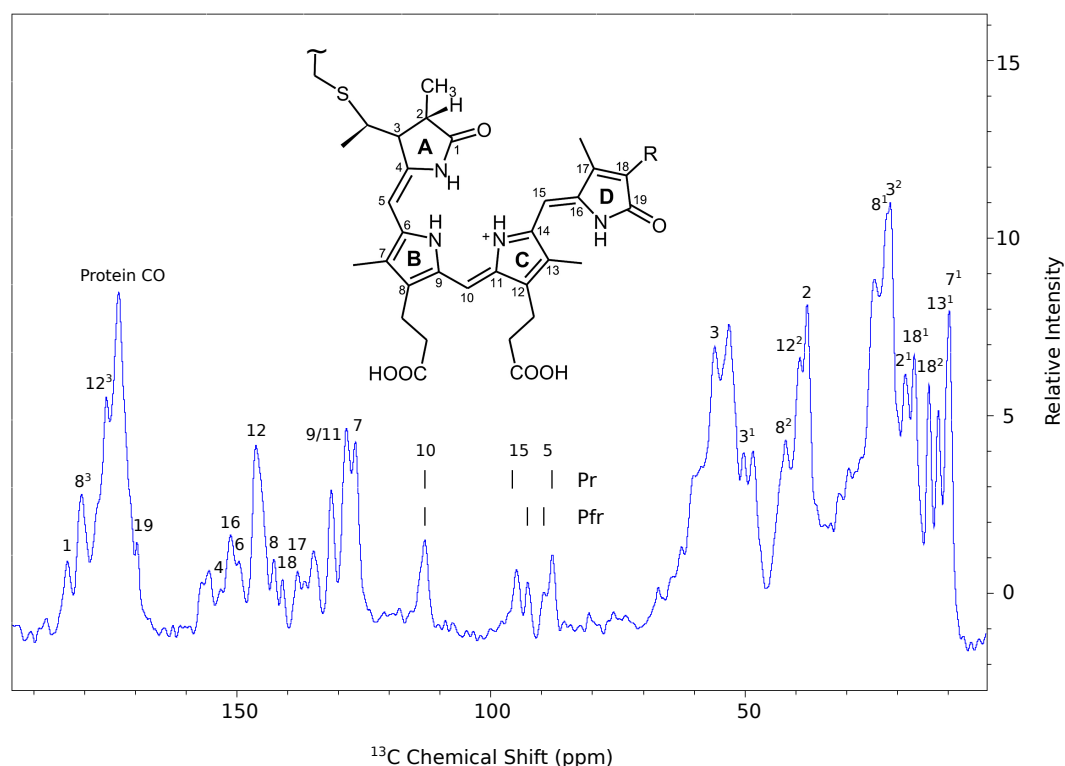


Figure 25: 1D hC-CP spectrum of Cph1Δ2 Pr state with u - $[^{13}\text{C},^{15}\text{N}]$ -labelled PCB, at 800 MHz and 261 K. Peaks are annotated according to the displayed PCB chromophore structure, where $R = \text{CH}_2\text{CH}_3$. Assignments were transferred from Rohmer et al. (129).

The intensity of these protein signals is relatively high compared to the chromophore peaks (see for instance carbonyl signals around 175 ppm, Figure 26) which can be explained by the large number of amino acids in the sample. As a consequence, protein resonances are present in the aliphatic region between 10 and 60 ppm that overlap with the chromophore signals. To avoid misinterpretations in the analysis of the temperature-dependent spectra, we concentrate on the methine resonances (85-100 ppm) as chromophore-specific

markers, since no protein resonances are expected in this spectral window (Figure 26, zoom on the right).

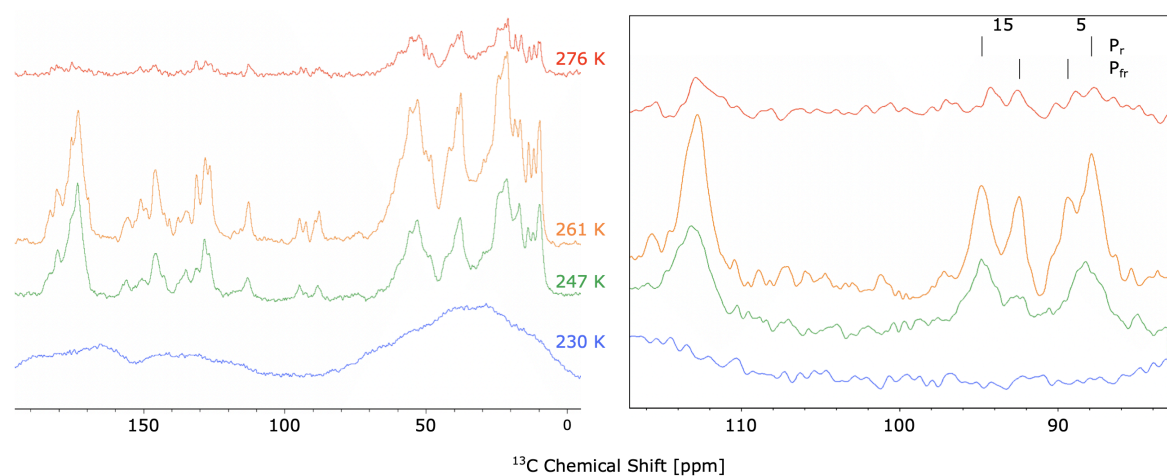


Figure 26: Temperature comparison at 800 MHz. 1D hC-CP spectra of Cph1Δ2 u-[^{13}C , ^{15}N]-PCB at temperatures above freezing temperature of the sample. Zoom into methine peak region, the assigned peaks for Pr and Pfr are in accordance to figure 25.

We analysed the signal intensities and line widths between 247 and 290 K. At temperatures below 230 K protein sample is frozen (see blue spectrum in Figure 26). The spectrum recorded at 261 K shows the smallest linewidth and highest signal intensity (see orange spectrum in Figure 26). At temperatures below, inhomogeneous line-broadening effects become dominant, as the sample freezing temperature is approached. This explains the less intense spectrum at 247 K. Raising the temperature to values above 261 K, the signal intensity is reduced which is demonstrated by the red spectrum recorded at 276 K (Figure 26). Comparing the signal intensity and linewidth, no difference between the signals of the chromophore methine carbons and protein signals is observed. In summary, there are no indications of a chemical exchange process taking place at the chromophore methine carbons.

From the temperatures compared we can conclude that a temperature around 261 K is optimal for recording experiments with PCB in Cph1Δ2 at 800 MHz. Monitoring chromophore-protein interactions requires the application of 2D

spectroscopy. 2D carbon-carbon correlations of u-[$^{13}\text{C},^{15}\text{N}$]-labelled PCB in Cph1 Δ 2 have been recorded at 264 K using different DARR mixing-times.

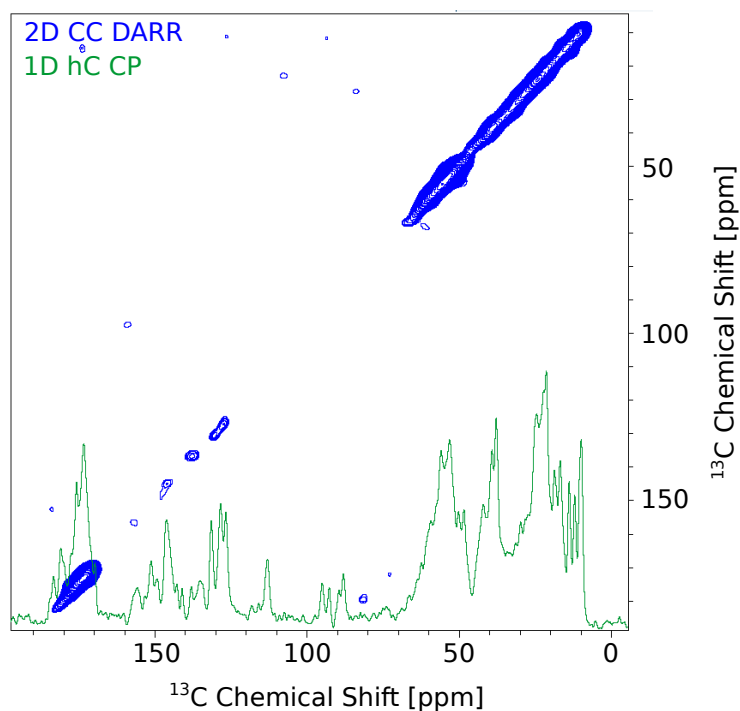


Figure 27: Superposition of 1D hC-CP in green with 2D ^{13}C - ^{13}C DARR spectrum in blue. 2D ^{13}C - ^{13}C DARR was recorded at 264 K, 20 ms mixing and 256 scans. 1D hC-CP was recorded at 261 K using 16 k scans.

Figure 27 shows the superposition of the 1D hC-CP experiment at 261 K in green with the 2D ^{13}C - ^{13}C correlation at 264 K in blue. Neither chromophore nor protein cross-peaks were observed, and even the diagonal peaks were missing in the chromophore specific area between 85 and 105 ppm (Figure 27, blue spectrum). This is not surprising as the 1D experiment contains less magnetisation transfers and is in general more sensitive. While the acquisition of more scans can help to overcome a lack in sensitivity, the measurement time of the 2D spectrum was 24h for 512 scans and 160 experiments, which would increase dramatically when using a multiple of the number of scans.

With the application of sedNMR at 261 K, we were able to record 1D ^{13}C spectra of the PCB chromophore. For the analysis of chromophore-protein interactions or structural changes in the ‘tongue’ region, the implementation of higher dimensional spectroscopy is essential. The sedNMR approach alone does not

provide enough sensitivity, even when applied at a temperature optimum. Hence, we decided to combine the sedNMR approach with high-field DNP.

3.2.2 Enhancements of M-TinyPol and bcTol-M are similar at 18.801 T

To prepare for the DNP measurements, we investigated the performance of two polarising agents, M-TinyPol and bcTol-M, at 800 MHz (18.8 T) (Figure 28).

For an optimal DNP efficiency, the chemical structure of the polarizing agents is crucial. In biradicals such as M-TinyPol and bcTol-M, the interaction between the unpaired electrons depends on their relative orientation and distance, which determines the performance of the biradical (130,131). The properties of the biradical systems can be characterized by EPR Spectroscopy. The EPR spectra of M-TinyPol and bcTol-M were recorded with an X-band continuous wave (9.4 GHz, CW) benchtop spectrometer by the group of Robert Bittl from the FU Berlin. The derivative-mode spectra are shown in Figure 28.

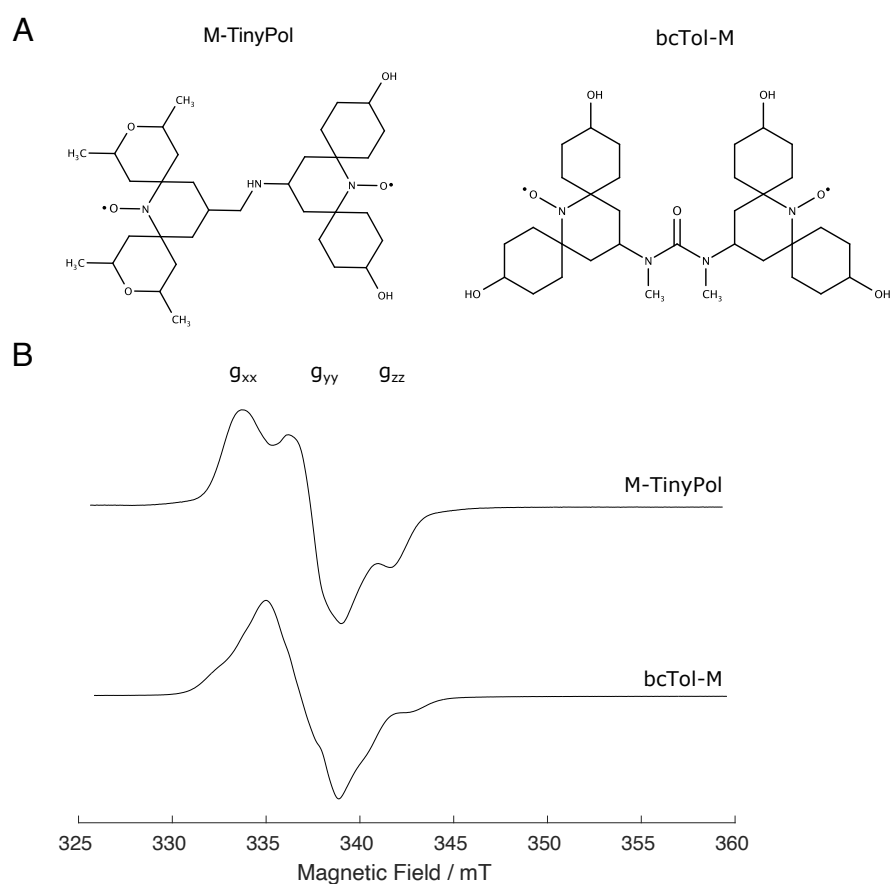


Figure 28: Structure (A) and X-band derivative EPR spectra (B) of M-TinyPol and bcTol-M at 100 K.

M-TinyPol and bcTol-M share a similar composition, the unpaired electrons of the nitroxide moieties are stabilised by bulky spiro compounds. bcTol-M has a more rigid and longer carbamide derivative linker, leading to a larger distance between the two free electrons. The shorter e-e distance in M-TinyPol results in the reduced depolarisation effect. In the presence of MAS spectral diffusion is induced which reduces the electron polarisation difference and leads to strong depolarisation effects (132). Strong electron-electron dipolar couplings can reduce the MAS dependency, as they facilitate electron-electron spin-exchange crossings. The exchange crossings contribute to the preservation of electron polarisation and a higher depolarisation factor (ϵ_{Depo}) of M-TinyPol (111), which is 0.65 compared to 0.5 (110) of bcTol-M.

M-TinyPol is an asymmetric biradical with a flexible linker that allows for rotations around the N-CH₂ bond, introducing different rotamers at 100 K (111). We see a broad central g_{yy} signal for both radicals in the derivative EPR spectra, with M-TinyPol showing distinct features in g_{xx} and g_{zz} which are a sign of electron-electron dipolar couplings and exchange interactions. The signal zero-crossing is at around 337 mT resulting in a g factor of 2.0099 for M-TinyPol and bcTol-M, the signal intensities of the two spectra are similar as well.

In preparation of the characterization of the DNP efficiency of both radicals at 800 MHz NMR proton frequency, field profiles covering a B_0 range from 18.805 to 18.787 Tesla were recorded with proline samples doped with M-TinyPol and bcTol-M. This is a narrow field profile centred around the expected maximum of positive enhancement of M-TinyPol, which was already known from previous work of the group of Anne Lesage (111). When recording a field profile, the microwave frequency is kept constant while the B_0 field is changed looking for the combination of MW and B_0 field which leads to the highest enhancement (see chapter 1.1.2).

Two different types of one dimensional ^{13}C spectra were compared, hC-CP and carbon direct-excitation spectra. The ^{13}C carbon direct-excitation spectra reflect enhancements resulting from the direct interaction between radical and proline without being mediated by the polarized proton network of the spin bath (direct DNP mechanism) (133). The field profiles generated from carbon direct-excitation spectra are shown in Figure 29. Enhancements were calculated as reduced Boltzmann enhancements ε_B as described in (37). The depolarisation effect of a radical is included in the Boltzmann enhancement, which makes these values comparable for different radicals.

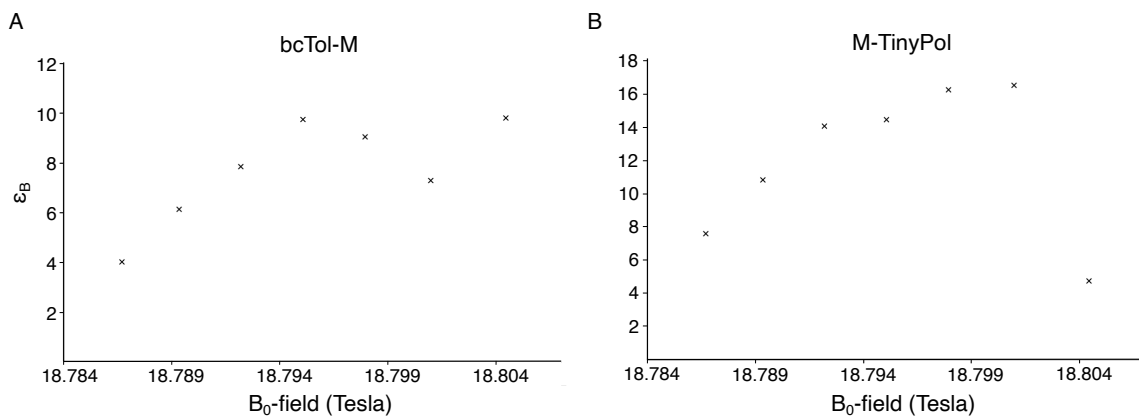


Figure 29: DNP field profiles of carbon direct excitation spectra of bcTol-M (A) and M-TinyPol (B).

The curve of bcTol-M peaks at 18.795 T with an ε_B of 9.8. The high ε_B value observed at 18.804 T is attributed to a very low initial MW-off signal. If instead the average value of the MW-off signal intensities is used as reference for ε_B at 18.804 T, a value of 6.6 is obtained (compared to 9.8) which we consider more reasonable. All spectra recorded with microwaves switched off vary to some extent in signal intensity, which was unexpected as the B_0 field itself should not have an influence on the peak intensity. Particularly at the high- and low-field limit of the field profile series we observe a significant difference: in the bcTol-M series, the signal intensity is drastically reduced at 18.804 T, whereas in the M-TinyPol series a reduction of the signal intensity is observed at 18.787 and 18.789 T. The corresponding 1D spectra of the bcTol-M doped sample are shown in

Figure 30. M-TinyPol has the highest Boltzmann enhancement with 16.5 at 18.801 T. Likewise, in this data series we observe a slight variation in the signal intensity of the spectra recorded without MW irradiation (see Figure 31), which, however, has only minor effect on the field profile. Comparing the direct excitation field profiles of the two PAs we conclude that M-TinyPol outperforms bcTol-M by far with an ϵ_B max of 16.5 compared to 9.8, and that they peak at different B_0 field strengths.

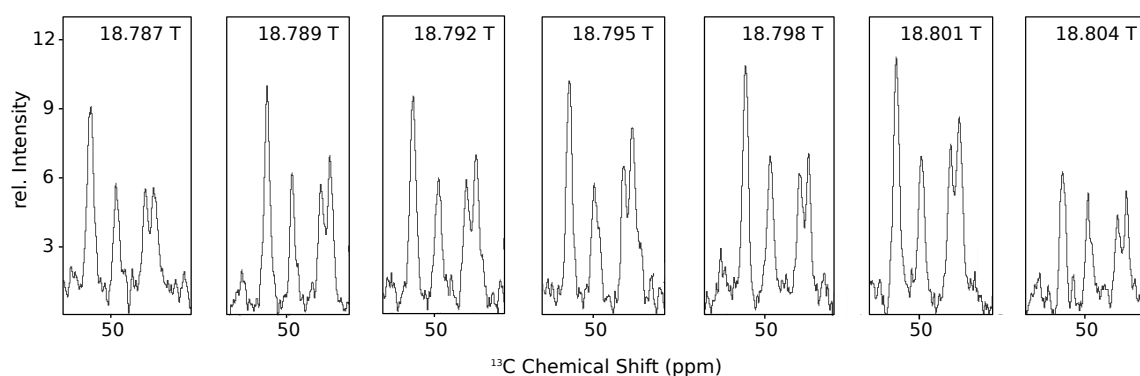


Figure 30: Aliphatic region of proline sample bcTol-M doped. Carbon direct excitation spectra recorded at different field strengths without microwave irradiation.

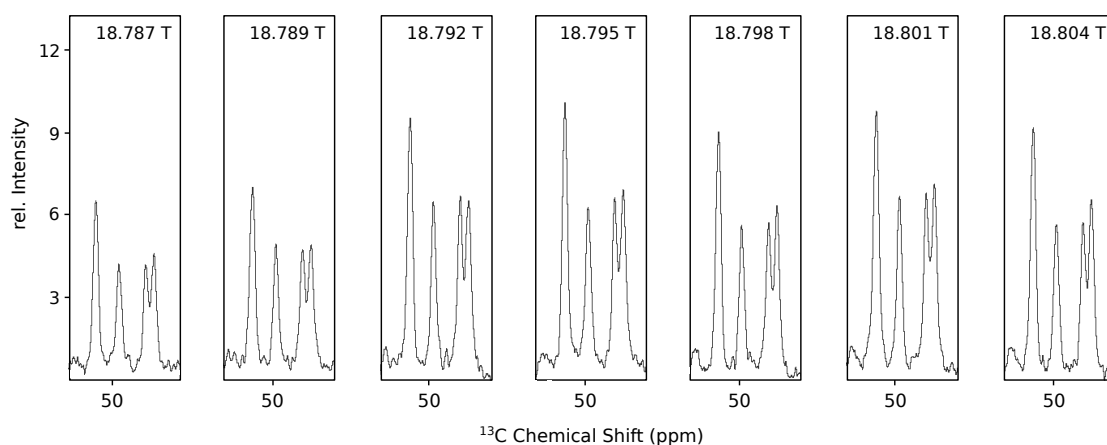


Figure 31: Aliphatic region of M-TinyPol doped proline sample. Carbon direct excitation spectra recorded at different field strengths recorded without MW irradiation.

It is more common to use CP-based experiments, in which case the polarisation is first distributed via proton spin-diffusion and then transferred to the nucleus of interest, here ^{13}C , via cross-polarization (hC-CP). The fast mechanism of proton spin-diffusion, higher ^1H dipolar coupling and e-n coupling and a more

homogeneous distribution of protons throughout the sample reduce the DNP build up time significantly and enables a faster repetition of experiments (134). The enhancements of M-TinyPol and bcTol-M proline samples, determined from hC-CP experiments, are shown in Figure 32. The measurement conditions - sample temperature, microwave irradiation frequency, spinning speed and concentration of proline and the respective radical - were similar for both samples. bcTol-M shows a maximum Boltzmann enhancement of 43.7 at 18.801 T, whereas M-TinyPol shows an enhancement of 42.4 at 18.801 T. The outlier of the bcTol-M proline sample at 18.789 T is due to a smaller spectral width, 61.7 kHz compared to 200 kHz, which was chosen accidentally.

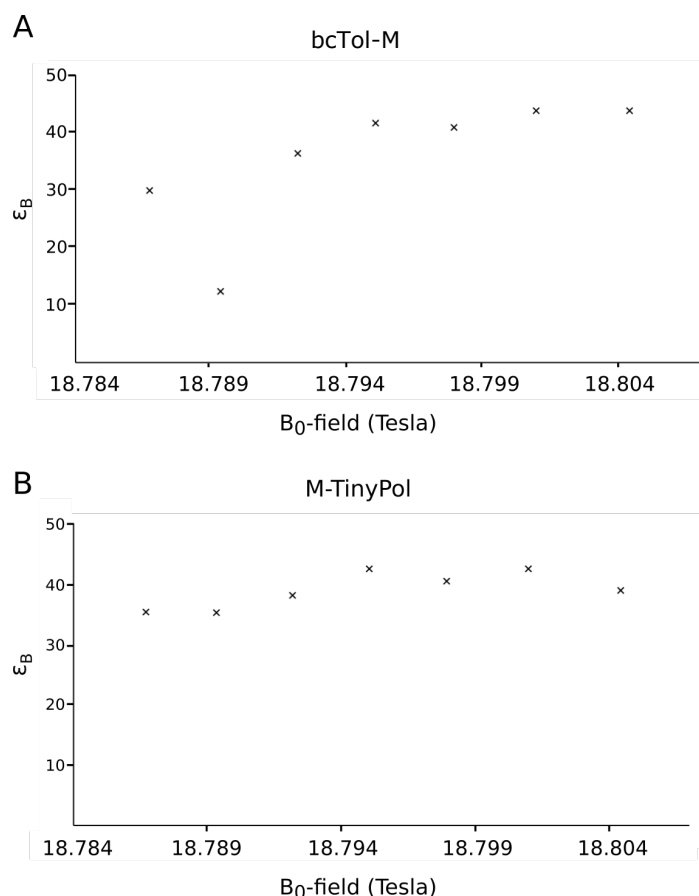


Figure 32: Field profiles of bcTol-M and M-TinyPol. (A) Boltzmann enhancement of bcTol-M, calculated from hC-CP spectra, versus magnetic field strength. (B) Boltzmann enhancement of M-TinyPol, calculated from hC-CP spectra, versus magnetic field strength.

Both curves show a comparable progression with lower ϵ_B at low B_0 field values. Comparing the enhancement of carbon direct-excitation and hC-CP experiments

we conclude that the maxima differ for the bcTol-M sample, with 18.795 T and 18.804 T for the carbon direct excitation and hC-CP experiments, respectively. For M-TinyPol the results coincide, in both cases we report the highest enhancements at a B_0 field of 18.801.

To determine the sensitivity factor κ we also determined $^{10\text{min}}\text{SNR}$ values from carbon direct-excitation and hC-CP experiments. The values of κ , reduced Boltzmann enhancements ε_B and traditional enhancement ε for both types of spectra are listed in Table 4 (bcTol-M) and Table 5 (M-TinyPol). The κ values calculated from the data of the hC-CP spectra are shown for the sake of completeness. A reliable $^{10\text{min}}\text{SNR}$ could not be determined since the spectra did not contain large enough areas of random white noise, and the distortions in the noise were rather similar for all spectra.

Table 4: DNP enhancement and sensitivity factor of proline bcTol-M.

		bcTol-M							
		B_0 (T)	18.787	18.789	18.792	18.795	18.798	18.801	18.804
hC-CP	κ	74.6	52.9	54.7	70.3	59.3	66.4	60.5	
	ε_B	29.9	12.4	36.3	41.7	40.8	43.7	43.7	
	ε	59.8	24.8	72.7	83.3	81.7	87.5	87.5	
C direct	κ	4.2	7.3	8.3	8.0	8.9	7.4	5.6	
	ε_B	4.0	6.2	7.9	9.8	9.1	7.3	9.8	
	ε	8.1	12.3	15.7	19.5	18.1	14.6	19.6	

Table 5: DNP enhancement and sensitivity factor of proline M-TinyPol.

		M-TinyPol							
		B_0 (T)	18.787	18.789	18.792	18.795	18.798	18.801	18.804
hC-CP	κ	51.0	57.0	60.8	58.2	48.2	58.6	50.7	
	ε_B	35.4	35.3	38.1	42.4	40.4	42.4	38.8	
	ε	54.4	54.2	58.6	65.3	62.2	65.3	59.8	
C direct	κ	10.7	12.2	15.7	18.7	21.7	23.8	14.2	
	ε_B	7.6	10.8	14.0	14.4	16.3	16.5	4.7	
	ε	11.7	16.7	21.6	22.2	25	25.4	7.3	

When comparing the efficiency of the two PAs, the sensitivity factor κ of the carbon direct-excitation spectra is 2 to 3 times higher for the M-TinyPol

doped sample. This is due to a higher $^{10\text{min}}\text{SNR}$ of the sample resulting from either a difference in the proline concentration of the two rotors or a more efficient direct DNP mechanism of M-TinyPol, which implies a more even distribution of the radical within the sample or a stronger e-n interaction with proline.

In the course of our measurements we observed that M-TinyPol degraded after about three weeks. Also, when comparing the performance of the two radicals on the phytochrome Cph1 Δ 2 sample at 18.798 T, we again noticed a degradation of the M-TinyPol doped sample. In Figure 33 the signal enhancement of bcTol-M and M-TinyPol in a biological preparation of Cph1 Δ 2 is shown, as well as the enhancement ε and reduced Boltzmann enhancement ε_B . While the glycerol concentration of these samples was reduced to a final concentration of $\sim 10\%$, the enhancements were similar compared to the proline samples. The proline samples contained 60 % glycerol, which is the standard concentration used in DNP experiments. These findings show that in sedimented or highly concentrated protein solutions the glycerol content can be decreased without significant loss of enhancement to prevent sample degradation.

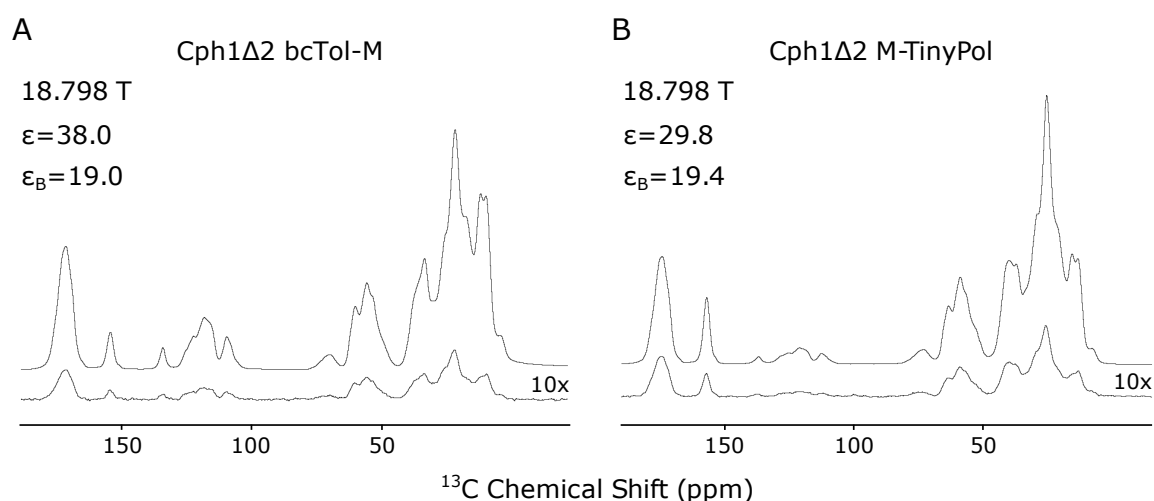


Figure 33: Comparison of bcTol-M and M-TinyPol on biological sample Cph1 Δ 2 at 18.789 T. (A) BcTol-M doped sample, the ^{13}C -CP spectra are shown with MW on and off. The MW off spectrum is enlarged by a factor of 10. (B) M-TinyPol doped sample. The ^{13}C -CP spectra are shown with MW on and off, the MW off spectrum is enlarged by a factor of 10.

Since the performance of bcTol-M and M-TinyPol was comparable, and to avoid problems due to the lower stability of M-TinyPol, we decided to continue to use the bcTol-M sample at a B_0 field strength of 18.801 T for further studies of Cph1 Δ 2.

3.3 Structural transitions in phytochromes upon light absorptions

The cyanobacterial phytochrome Cph1 Δ 2 can adopt two photo-interconvertible states: an inactive red-light absorbing (Pr) and an active far red-light absorbing state (Pfr). Structural differences between the two forms will be characterized by ssNMR. The focus is set on a short region of the Phy domain, the ‘tongue’ region, which seals the chromophore binding pocket in the Pr state and is expected to undergo structural changes when transitioning to the Pfr state.

From the reception of an external light signal to an internal output, phytochromes provide a mechanism for plants and bacteria to sense and react to various light conditions. Structural rearrangements in the chromophore binding pocket, happening at picosecond timescale (135), have been shown to be the origin of the signal transduction process, inducing further conformational changes in the protein (79,85). Most of the existing structures of the chromophore-bearing photo-sensory module of phytochromes stem from bacteriophytochromes and show the Pr state (136). The β -sheet to α -helix conversion of the ‘tongue’ region has been exclusively shown in *Dr*BphP using a combination of time resolved X-ray scattering, X-ray crystallography and molecular dynamics simulation (91). X-ray crystallography can provide structural information at high resolution, but it requires well diffracting crystals and suffers from radiation damage. In phytochromes a high X-ray radiation dose can lead to chromophore deprotonation or rupture of the thioether linkage between protein and chromophore (137,138). An additional problem that emerges when working with the Cph1 variant is the destruction of crystals when irradiated by light. Therefore, Cph1 crystals cannot be recycled and the analysis of structural changes in the protein by X-ray crystallography requires the separate preparation of Pr and Pfr Cph1. While an X-ray structure of Pr Cph1 Δ 2 has been published

more than 10 years ago, the Pfr state remains elusive as well diffracting crystals of this Cph1Δ2 form have not been obtained. The application of ssNMR offers the possibility to analyse structural transitions in phytochromes upon light irradiation within one sample, which can be measured in both states consecutively.

3.3.1 Efficient labelling reduces peak overlap in Cph1Δ2 spectra

To reduce the number of peaks in our spectra in favour of improved resolution, a specific labelling scheme was chosen with only arginine, isoleucine tryptophan and valine ^{13}C labelled. The resulting NMR response has several benefits: the expected C_α and C_β chemical shifts of the particular amino acids differ from one another and the individual amino acids show significant chemical shift differences when situated in an alpha-helix or beta-sheet (139). Moreover and importantly, these amino acids which constitute a consecutive sequence in the ‘tongue’ region a unique IVR motif, are not overrepresented in the rest of the construct or prone to scrambling. In addition, tryptophan is included in the labelling scheme, because W450 and W476 of the ‘tongue’ region are vis-à-vis when a beta-sheet is formed and this proximity is broken when an alpha-helix is formed. With this approach, a total number of 105 residues are labelled, 36 of which are within pairs or triplets. Figure 34A shows histograms of the chemical shift distribution of arginine, valine and isoleucine C_α resonances, to illustrate the significant chemical shift difference with respect to the secondary structure. Combining the information of C_α and C_β resonances of the IVR motif, it should be possible to identify the secondary structure of the ‘tongue’ region. This is demonstrated in Figure 34B, where simulated carbon-carbon correlations of arginine, isoleucine and valine C_α and C_β are presented, color-coded depending on the structural motif. An important requirement for using this strategy to successfully characterize the structural motif of the ‘tongue’ region is that the spectral

linewidth is small enough to visualise the chemical shift differences in the spectrum, which is not trivial when measuring under DNP conditions. At cryogenic temperatures the spectral quality suffers from inhomogeneous line-broadening.

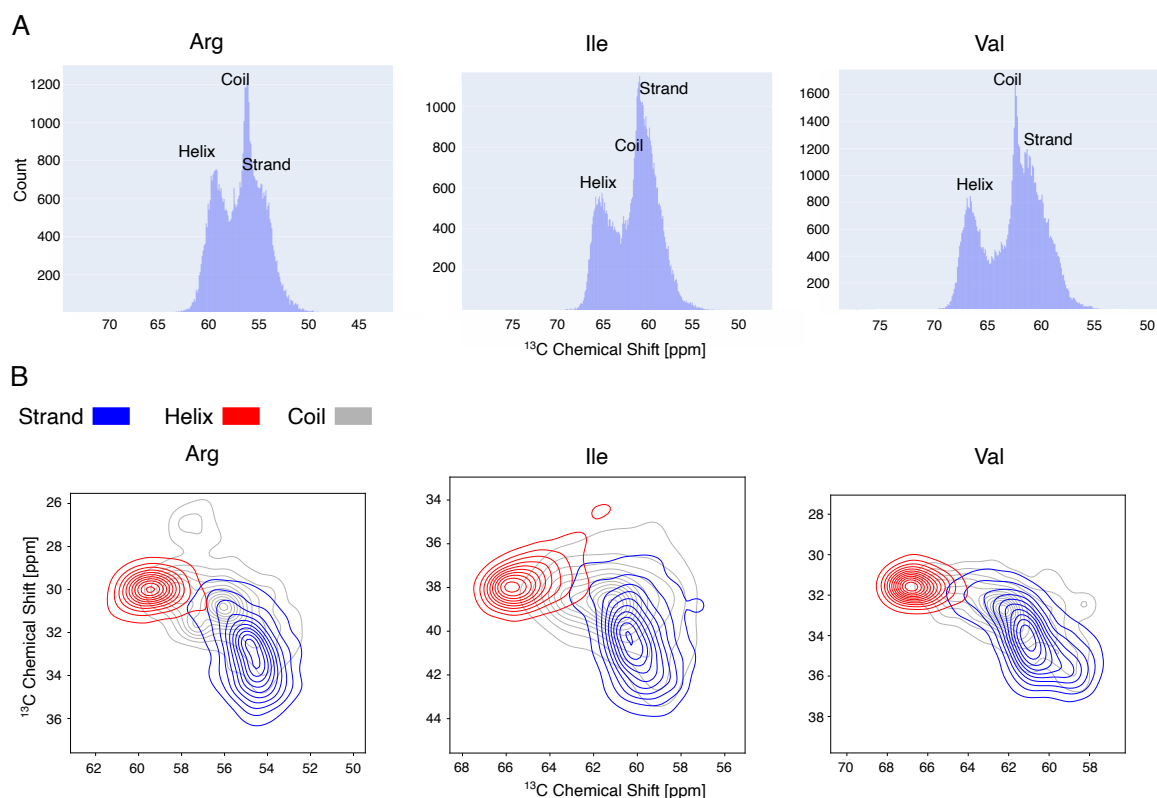


Figure 34: Chemical shift distribution of arginine, isoleucine and valine C_α and C_β resonances. (A) Histogram of the distribution of C_α resonances of arginine isoleucine and valine with the structural motif indicated. Plots modified from BMRB (140). (B) Simulated 2D carbon-carbon correlation of C_α and C_β resonances of an amino acid pair of the same type. Color-coding according to structural motif: α -helical peaks in red, peaks within a β -strand in blue and random coil in grey. PACSY NMR chemical shift database was implemented in a script of Miguel Arbesú to generate the 2D plots (141).

3.3.2 Signals with α -helical chemical shift pattern assigned to the ‘tongue’

IVR triplet are present in 3D hCaNCOCa Pfr Cph1Δ2

The state of the protein was monitored by recording UV-Vis spectra from 800 to 350 nm, before the insertion of the rotor into the magnet. Figure 35A shows an exemplary UV-Vis spectrum of Pr Cph1Δ2 in A, which we assume to be pure as it shows one single absorption maximum at 654 nm. In Figure 35B we see the spectrum of a mixture of Cph1Δ2 in the Pr and Pfr state showing a maximum

at 654 nm (Pr absorption) with a shoulder at 709 nm (Pfr absorption). The feature observed at 600 nm is an artefact that has been observed in UV-Vis spectra of other samples as well.

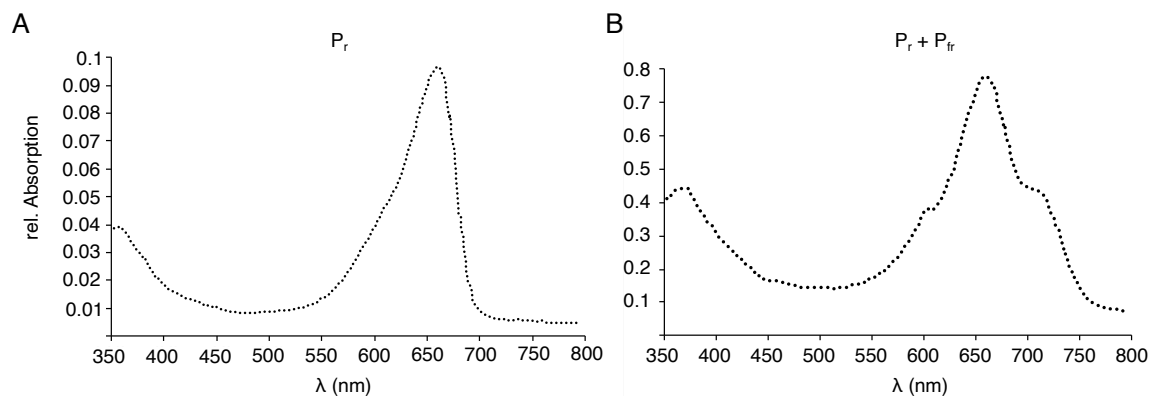


Figure 35: UV-Vis spectra of Pr sample in (A) and Pfr sample in (B).

We recorded 1D hC-CP as well as 2D hNCa, hNCO and hCC DARR spectra of the Cph1Δ2 phytochrome in pure Pr state. The spectra show reasonable linewidths that were promising for the analysis of the 3D spectra. Figure 36 shows some of the pre-experiments recorded on Pr state Cph1Δ2 under DNP conditions. In Figure 36A an hCC DARR spectrum is shown. The top right panel shows a zoom-in of the C_α-C_β region and the bottom right of the aromatic region, illustrating that it is feasible to resolve areas with peaks that are fingerprints of specific types of amino acids. Especially the C_α-C_β resonances of isoleucine (I) and valine (V) residues are well separated from the bulk signal in the carbon-carbon correlation, whereas arginine (R) and tryptophan (W) C_α-C_β peaks are overlapping (indicated with W/R, top right panel). The aromatic region between 110 and 140 ppm contains some well-resolved peaks of tryptophan side chain carbons (bottom right). The significance of the tryptophan side chain resonances will be subject of the discussion later on (see Figure 39).

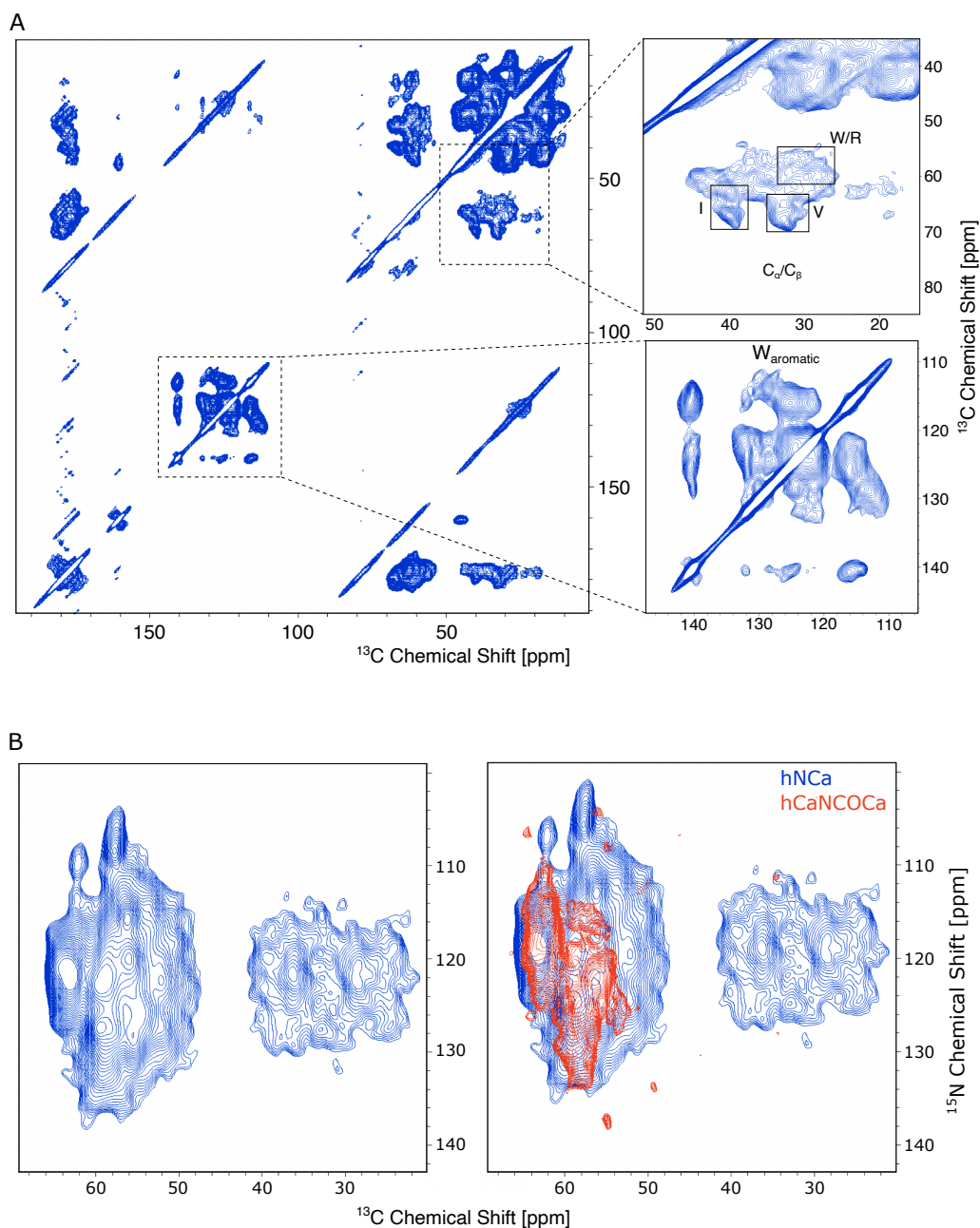


Figure 36: Spectra of *Cph1Δ2* in the *Pr* state recorded under DNP conditions. (A) hCC DARR spectrum (20 ms mixing time, 100 K) with zoom into C_{α}/C_{β} region (top right) and aromatic region (bottom right). Spectral regions with peaks of specific amino acids are highlighted by squares and labelled. (B) $hNca$ spectrum and superposition of $hNca$ and the 2D NC projection of an $hCANCOCa$ spectrum.

Using experiments that are standard for assignment strategies under DNP conditions, for instance a combination of $hNcaCb$ and $hN(CO)CaCb$ spectra, would result in spectra with strong overlap for the labelled residues. This becomes evident when looking at the $hNca$ spectrum shown in Figure 36B on the left. In this spectrum one peak for every labelled amino acid residue is expected. A

significant peak overlap dominates the C_α -region of the spectrum between 65 and 50 ppm, rendering the assignment of single peaks impossible. Additionally, the NCa-transfer was not specific enough, so that resonances between 40 and 28 ppm were observed, originating from N- C_β correlations.

We thus decided to use a hCaNCOCa pulse sequence, as described in section 2.2.6, where a correlation is only expected between the C_α of two consecutive residues if both residues are ^{13}C , ^{15}N labelled. With the labelling scheme employed, this should result in a total number of 22 peaks in the spectrum. In Figure 36B on the right, the superposition of the hNCa spectrum with a 2D N-C projection generated from the 3D hCaNCOCa spectrum is depicted (both of Cph1 Δ 2 in the Pr state). Comparing the two spectra in signal intensity and peak quantity, it is obvious that the hCaNCOCa spectrum contains a reduced number of signals, approximately 50 % less than those observed in the hNCa spectrum. This results in less peak overlap and a better resolution of the C_α -region. The specificity of the hCaNCOCa spectrum derives from the pulse sequence, which prevents a magnetisation transfer to C_β . Undesired N- C_β resonances are suppressed and a higher amount of magnetisation is transferred to the C_α .

A set of 3D hCaNCOCa and NCaCb spectra of Cph1 Δ 2 in the Pr and Pfr state was recorded and then compared with regard to differences. Here it is important to note that the Pfr state of Cph1 Δ 2 is not pure, but consists of a mix of Pr and Pfr states (see UV-Vis spectrum, Figure 35). The hCaNCOCa spectra are thus expected to show similarities for both samples due to the persistence of Pr after the photo-conversion to Pfr. Additional resonances of the ‘tongue’ IVR residues should appear in the spectrum of Pfr Cph1 Δ 2, especially when these residues are in different secondary structural elements in the two states.

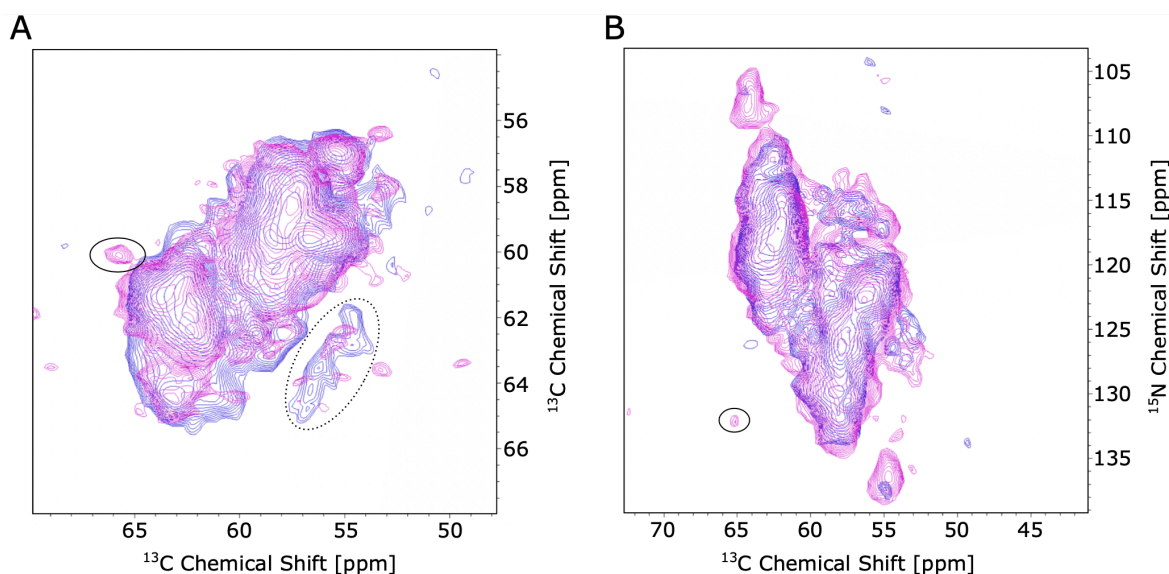


Figure 37: Comparison of 2D projections of hCaNCOCa spectra recorded on Cph1Δ2 in the Pr state in blue and in the Pfr state in pink. (A) ^{13}C - ^{13}C projection (B) ^{15}N - ^{13}C projection. The encircled peak can be assigned to the VR resonance of IVR motif in ‘tongue’ region.

In Figure 37 the 2D ^{13}C - ^{13}C (A) and ^{15}N - ^{13}C (B) projections the hCaNCOCa spectra of Pr (blue) and Pfr Cph1Δ2 (pink) are superimposed. As expected we observe additional peaks in the Pfr spectrum. Amongst them is the encircled resonance which corresponds to a C_α - C_α correlation of a helical valine arginine (VR) pair. In addition, an isolated set of peaks (encircled by dotted line) is observed in the ^{13}C - ^{13}C projection of the Cph1Δ2 Pr spectrum, with only partially overlapping signals of the Cph1Δ2 Pfr spectrum. This was unexpected, and can be a result of different conformations present in the Pr state of Cph1Δ2. With the segmentation of the 3D spectra in the nitrogen dimension, two peaks in the Pfr spectrum have been identified which can be assigned to the IVR-sequence of the ‘tongue’ region. In Figure 38, such two ^{13}C - ^{13}C planes of Pr (blue) and Pfr Cph1Δ2 (pink) hCaNCOCa spectra and Pfr hNCaCb spectrum (black) are shown, extracted from the 3D spectrum at the nitrogen frequencies indicated at the bottom right. The schemes below the spectra illustrate the respective magnetisation transfers for the hCaNCOCa pulse sequence. With their help, it may be appreciated that the nitrogen polarisation originates from the arginine residue in the left plane and from the valine in the right plane. The dotted black

lines mark the spectral region of the hNCaCb spectrum where the C_β resonances of the arginine (left plane) and valine (right plane) residues are located. The C_β information can be used to clearly distinguish a valine from an isoleucine residue. Whilst the C_α chemical shifts of valines and isoleucine are similar their C_β resonances differ, with average shifts of 38.6 ppm and 32.7 ppm, for Ile and Val, respectively (see Figure 34).

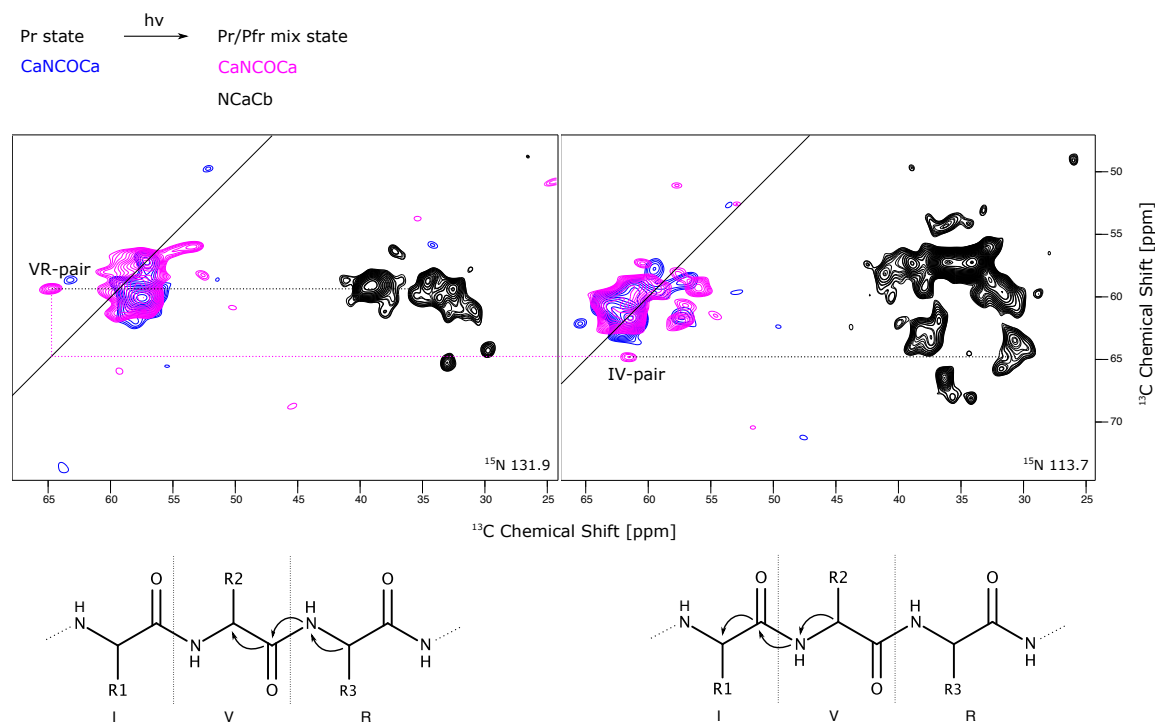


Figure 38: Assignment of the IVR region. Superposition of ^{13}C - ^{13}C slices extracted at different ^{15}N frequencies from hCaNCOCa spectra of Cph1Δ2 in Pr (blue) and Pfr state (pink) with Pfr state hNCaCb spectrum in black. ‘VR-pair’ in the left top panel indicates the correlation of arginine C_α with valine C_α . The magnetisation transfer is indicated by arrows in the skeletal formula at the bottom left. ‘IV-pair’ in the top right panel indicates the C_α - C_α correlation of a valine and an isoleucine residue. The magnetisation transfer is pointed out by the arrows in the skeletal formula at the bottom right.

The C_α - C_α correlation labelled ‘VR-pair’ is exclusively present in the Cph1Δ2 Pfr spectrum, the same holds for the ‘IV-pair’. The ‘VR-pair’ resonance shows chemical shifts which are specific for an alpha-helical arginine C_α (60 ppm) and an alpha-helical valine C_α (64 ppm). The C_α chemical shifts of the ‘IV-pair’ resonance also indicate that the corresponding residues are in an alpha-helix. With the information of the C_β chemical shift from the hNCaCb, we can unambiguously assign the C_α chemical shift at 65 ppm to a valine residue. The

C_{α} chemical shift at 63 ppm is either assigned to an isoleucine or a valine, the ‘IV’-pair resonance could also correspond to a ‘VV’-pair. In addition, the two peaks have to originate from a sequential triplet, as they share the C_{α} resonance at 65 ppm which is assigned to a valine residue, indicated by the pink dotted lines connecting the two signals. These signals can thus be either assigned to a VVR or an IVR triplet. To distinguish between the two possibilities, we benefit from the fact that only one IVR triplet is present in the protein sequence but no VVR triplet occurs. Hence, the two peaks are assigned to the IVR motif of the ‘tongue’ region. As they show an α -helical chemical shift pattern we conclude that the tongue region forms an α -helix in the Pfr state.

Unfortunately, it was not possible to assign the IVR triplet in the Pr state of Cph1 Δ 2. The expected ^{13}C chemical shifts of the beta-sheet residues are either hidden by overlapping peaks in the bulk, or are not present at all in this spectrum. A possible explanation is a higher flexibility concomitant with the heterogeneity of the tongue region in the Pr state, which has been proposed by Gustavsson *et al.* (123). The authors were not able to assign backbone resonances of ‘tongue’ region in the dark-adapted Pr state when performing solution NMR experiments on the bacterial phytochrome *DrBphP*. They assume the heterogeneity of this region is of functional relevance for the signalling process in this phytochrome (123). When recording ssNMR spectra of Pr state Cph1 Δ 2 under DNP conditions, the presence of different, but in this case not flexible, conformations leads to sample heterogeneity which can induce peak broadening below the detection limit. While it is difficult to attribute missing signals in the hCaNCOCa spectrum a significance, we consider the structural heterogeneity of the ‘tongue’ region in the Pr state a potential explanation for the absence of NMR signals.

During the segmented analysis and comparison of the 3D hCaNCOCa spectra several isolated peaks are observed in the Pr spectrum which are not present in the Pfr spectrum and vice versa. This suggests that not only the ‘tongue’ region is affected by structural rearrangements, but that also other parts of the protein are in a different chemical environment upon light absorption. The assignment of the IVR-sequence in the ‘tongue’ region is based on the appearance of two NMR signals. One of them, the IV-pair resonance shows a signal intensity which is just above the noise level and clearly weaker than the rest of the resonances in the bulk (see Figure 38, right plane). Regardless of how well the spectral data supports the assignment of the two signals, the acquisition of further experiments would be helpful to confirm the data and rule out that these two signals match by chance. However, the resolution of spectra acquired under DNP conditions is not high enough to implement other pulse sequences which are commonly used for the assignment of backbone resonances. We therefore decided to prepare another Cph1Δ2 sample with a reduced labelling scheme RV-¹³C,¹⁵N (see section 4.1) and reproduce the spectra. The persistence of the resonance labelled ‘VR’ with the simultaneous disappearance of the ‘IV’ signal in the Pfr hCaNCOCa spectrum will be considered as confirmation of the assignment. A complete set of spectra of the Pr state RV-¹³C,¹⁵N sample has already been acquired, but is not included in this work, as the recording of the Pfr state data not finished yet. Another means to shed light on the structural transition upon light reception is the analysis of tryptophan resonances. In total, the Cph1Δ2 sequence comprises 7 tryptophan residues, two of them (W450 and W478) are within the ‘tongue’ region. Figure 39B shows the superposition of the crystal structure of Pr Cph1Δ2 (PDB: 2VEA) in grey with a homology modelled structure of Cph1Δ2 in cyan, which is based on the bathy phytochrome from *Agrobacterium fabrum* in the Pfr state (PDB: 6G1Y).

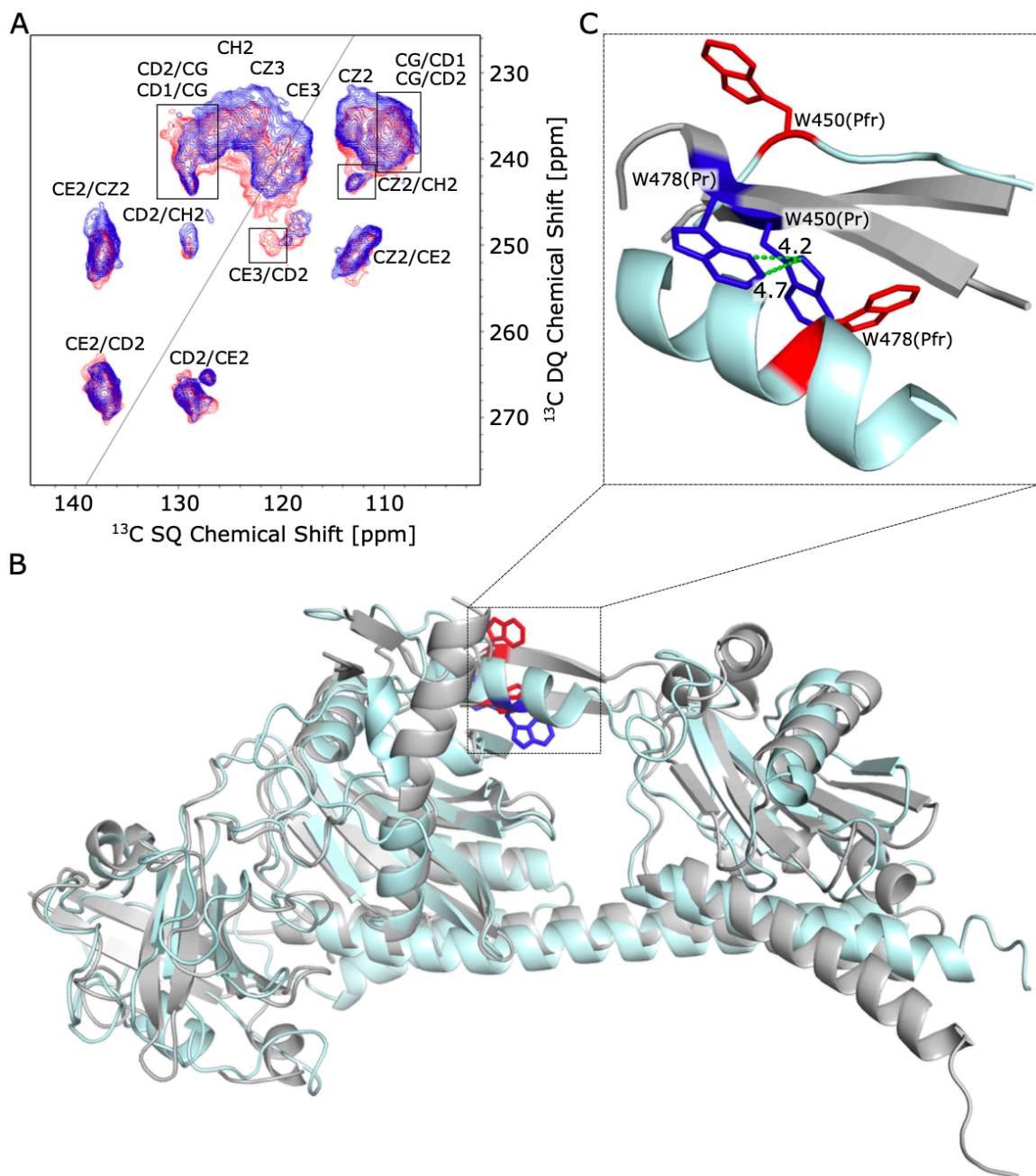


Figure 39: Comparison of tryptophan residues in Pr and Pfr state. (A) Aromatic region of SQ-DQ spectrum of Pr (blue) and Pfr (red) Cph1Δ2, the diagonal is delineated in grey. The specific peak regions are labelled according to the BMRB. The region comprising CH2, CZ3 and CE3 resonances cannot be further divided into specific peaks. (B) Superposition of the crystal structure of Cph1Δ2 in Pr state (PDB:2VEA) in grey with a predicted structure of Cph1Δ2 in cyan, generated by I-TASSER (142) homology modelling based on *Agrobacterium fabrum* phytochrome in the Pfr state (PDB:6G1Y). (C) Zoom into the ‘tongue’ region with tryptophan residues highlighted in blue (Pr) and red (Pfr state), in a different orientation. Dotted lines indicate distances between the closest carbon side chain atoms of the two tryptophan residues in the Pr state.

Having a closer look at the location of the two tryptophan residues, W450 and W478, in the zoom (see Figure 39C), it becomes apparent that these residues are face-to-face in the antiparallel beta-sheet formed in the Pr state (blue coloured

side chain). The situation is different in the Pfr state where W478 is located in a helical structure element and W450 in a loop. The proximity between W450 and W478 is broken and the chemical environment of these residues has changed, as shown in Figure 39C (red coloured side chain). This change of chemical environment should be visible in ^{13}C SQ-DQ NMR spectra. In this spectrum we observe cross correlations of adjacent backbone and side chain carbon atoms within a residue. Resonances originating from the two tryptophan residues in the ‘tongue’ region will show different chemical shifts in the Pfr state spectrum compared to the Pr state. The superposition of the aromatic region in the SQ-DQ spectra of the Pr form (in blue) and the Pfr form (in red) is shown in Figure 39A. This region is particularly suitable for the analysis, because it only consists of tryptophan side chain ^{13}C resonances. The various regions where correlations between the different carbon resonances of tryptophan side chain typically appear are indicated in the spectrum. The two spectra are relatively similar, with some differences in the peak-shapes. Nevertheless, the region around 120 ppm in the SQ dimension and 250 ppm in the DQ dimension, comprising CE3/CD2 correlations, shows cross-peaks that are clearly only present in the Pfr spectrum. In the Pfr state, at least one of the 7 tryptophan residues present in the protein resides in a different chemical environment which is reflected by the additional signals in the corresponding spectrum. Based on our data it is not possible to distinguish between resonances of the different tryptophan residues. Although the additional resonances in the DQ-SQ Pfr spectrum cannot be assigned to one of the residues in the ‘tongue’ region (W450/W478), this data promotes the idea of a structural rearrangement in this region.

The assignment of tryptophan side chain resonances with NC correlations is difficult using ssNMR. Due to the additional line broadening under DNP conditions, the resolution might be too low to assign these resonances. An

alternative approach could be the successive mutation of W450 and W478 to phenylalanine and subsequent analysis of the SQ-DQ spectrum to identify which signals are missing upon mutation in comparison to the wildtype spectra.

Additionally, using a W-labelled sample, one could also use the distance between the tryptophan side chain nitrogen atoms as indication for the ‘tongue’ rearrangement. Recording 2D proton-mediated homonuclear ^{15}N correlation (NHHN) or ^{15}N - ^{15}N proton assisted recoupling (PAR) (143) spectra, one expects a cross-correlation connecting two side chain tryptophan residues if the nitrogen atoms are in close proximity to one another. This would be the case for W450 and W478 in the Pr state (*cf.* Figure 39C, blue W residues, the N_W - N_W distance is $\sim 8 \text{ \AA}$). In the Pfr state, the two tryptophan nitrogen atoms would be too far apart from another to enable a magnetisation transfer and no correlation would be observed (Figure 39C, red W residues, their N_W - N_W distance is $\sim 15 \text{ \AA}$). With 7 residues labelled, and only two pairs of tryptophan residues (W450/W478 and W439/W489) that are spatially close, the resolution of the spectrum should be good enough to identify the ‘tongue’ resonances in particular because this resonance is expected to be the only one that depends on the state of the protein.

The presented data gives evidence for the formation of an alpha helix in the ‘tongue’ region upon light reception, further confirmation will be obtained by repeating the experiments with a RV- ^{13}C , ^{15}N labelled sample.

4 Conclusion and Future

Perspectives

4.1 Verification of structural rearrangements of the ‘tongue’ region using a RV-labelled Cph1Δ2

Phytochromes are challenging biological systems, especially when it comes to the application of NMR. Being too large for solution NMR with a molecular weight of around 60 kDa or more, but not immobile enough for ssNMR. It is thus important to find the right measurement conditions for the scientific question addressed. For the observation of structural changes in Cph1, DNP was the most promising method. The application of DNP is in general accompanied by the loss of spectral resolution due to significant line broadening. A reduced labelling pattern, with only four amino acids W,I,R and V ¹³C labelled, was applied to counteract on the loss of resolution. Surprisingly, the spectral quality was not good enough to resolve resonances in spectra recorded on the Pr state of the protein. Changing the labelling scheme from WIRV to RV reduces the total number of labelled amino acids from 105 to 67 and reduces the number of consecutively labelled amino acids by a factor of two. This will significantly increase the resolution of the NMR spectra and in the best-case could lead to the complete assignment of the tongue’s VR pair in both protein states.

Previous solution NMR experiments on the PSM of *DrBphP* failed to resolve the ‘tongue’ region in the Pr state. The authors therefore suppose a structural heterogeneity in the micro-to-millisecond time regime for this region (123). When working at cryogenic temperatures the different conformations are ‘frozen out’, which leads to peak broadening. Together with inhomogeneous line broadening, which is associated with the application of cryogenic temperatures, this can result in peak loss. Hence, it is not surprising for the ‘tongue’ resonances to be absent in the spectra recorded on Pr state Cph1Δ2.

In the hCaNCOCa spectrum, which is used for the assignment of residues located in the ‘tongue’ region, cross-correlations of C_α carbon atoms of two consecutive

amino acids are observed. The assignment of the Pr state signals is simplified with the change of labelling scheme. The sequence of the Cph1Δ2 construct comprises two VR-pairs, one is located in the ‘tongue’ region, the other one is part of a VRR-triplet (residues 166 to 168), and as such can be distinguished from the ‘tongue’ VR-pair. The resonances of the five RV-pairs of the Cph1Δ2 sequence will not appear in the same region of the hCaNCOCa spectrum, which prevents signal overlap. The identification of the type of amino acid is simplified in spectra recorded on the RV sample as the two amino acids have significantly different C_{α} chemical shifts (see Figure 30).

This work will benefit from the possibility to generate a 80 % pure Pfr state of Cph1Δ2 in the lab of Jon Hughes, which was unfortunately not taken into advantage when working with the WIRV sample. This will in addition reduce spectral overlap in the Pfr spectra and help to unambiguously identify Pfr peaks as such. By combining the information gathered from spectra recorded on the WIRV sample with the RV sample it is possible to either verify or exclude the assignment of the ‘tongue’ region in the Pfr state. In the hCaNCOCa spectrum of the RV sample, the resonance labelled ‘VR’-pair should persist, while the resonance corresponding to the ‘IV’-pair is expected to disappear if the assignment is correct. First measurements with the RV sample have already been conducted, but are not included in this work.

4.2 Characterization of protonation dynamics in the binding-pocket of Cph1 Δ 2

Structural traits, environmental fluctuations and exchange processes of the chromophore are key factors impacting light reception in phytochromes. In Cph1 the structure of phycocyanobilin (PCB) and its interactions with protein residues and water molecules in the binding pocket directly affect the saturating wavelength of the chromophore. This is reflected in the red-shift of PCBs absorption maximum in the active Pfr state. In the binding pocket an extensive hydrogen bond network between water molecules, PCB and Cph1 side chain residues exists stabilizing the chromophore conformation (89). Protonation dynamics of the hydrogen-bond network of the binding pocket not only have an impact on the light absorbing chromophore, but are further relayed to the protein as part of the signalling process. Comparing the protein in its inactive and active state, is a key to understand how these differences translate to the signalling output.

The binding pocket of various phytochromes from different organisms, has been studied using structural biology tools, from X-ray crystallography and time resolved serial femtosecond crystallography (SFX) to Fourier Transformation Infrared spectroscopy (FTIR) and solution and solid-state NMR. The chromophore is surrounded by several conserved residues which are important for the photo-conversion. Histidine 260 is located between the B and C ring and is involved in a hydrogen-bond network with the nitrogen atoms of pyrrole ring A to C, the pyrrole water and a conserved aspartic acid (D207) (144). This network is assumed to be maintained in both photo-states. Recent SFX experiments of bacteriophytochromes revealed a strong difference electron density at the A-ring, Asp207 and the pyrrole water, which was interpreted as photo-dissociation or photo-ejection of this water (135,145). Histidine 260 seems

to be crucial for phytochrome photo-conversion, as mutants lacking this residue are not able to achieve conversion to the photo-active state.

Another conserved residue is H290, which stabilizes the chromophore D-ring in Pr and shows hydrogen-bonds to the propionate group of the C-ring in Pfr (144). The photoactivation in phytochromes starts with the Z to E isomerisation of chromophore ring D, changes in the hydrogen-bonds between PCB and H290 accompany this rotation and might involve de- and re-protonation of PCB. The interaction of His260 and His290 with PCB and the proton network surrounding these residues, can be studied by ssNMR using a ^{13}C HY selective Cph1 labelling scheme with u- $^{13}\text{C},^{15}\text{N}$ -PCB. The role of the pyrrole water throughout the photocycle, and differences in its hydrogen bond network between Pr and Pfr state can be directly observed by proton NMR spectroscopy.

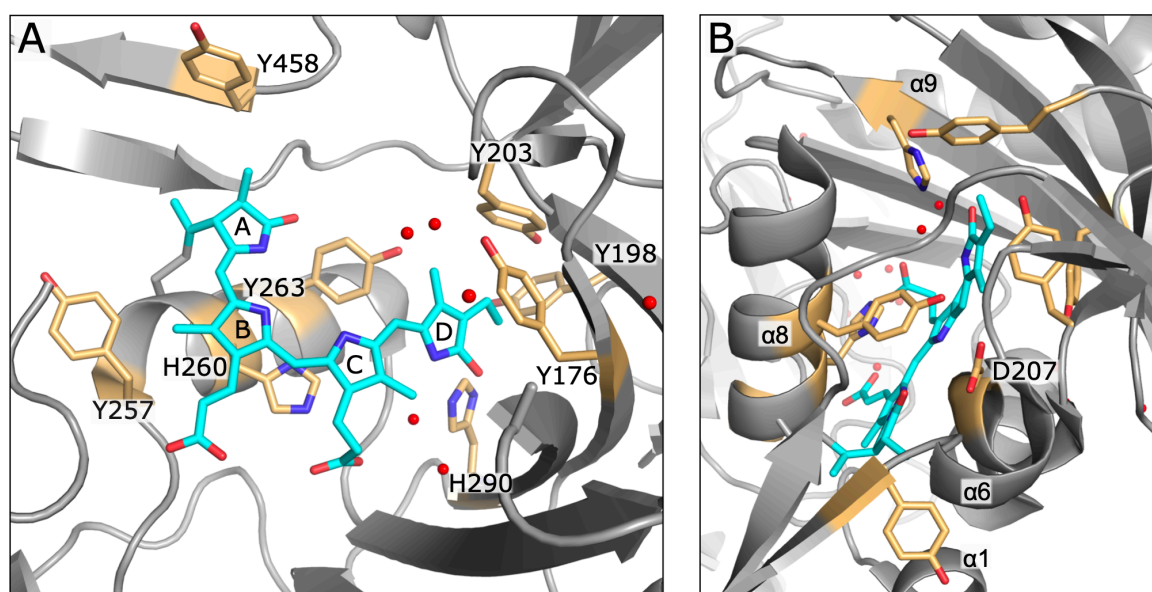


Figure 40: Binding-pocket of Cph1. (A) The PCB chromophore is depicted in cyan with the surrounding histidine and tyrosine residues in gold. For clarity, the α_6 -helix of the GAF domain, including residue D207, has been omitted. Water molecules are shown as red spheres. (B) Complete binding pocket with surrounding helices labelled for orientation.

Three tyrosine residues (Y176, Y203 and Y263) are surrounding ring D and form together with Val186 and Pro204 a hydrophobic sub-pocket. Y176 and Y263 seem to be essential for the formation of Pfr in plants as mutants fail to photoconvert (89). Y458, which is part of the ‘tongue’ region, is involved in the

shielding of the thioether linkage from the solvent, together with Leu 469-Pro 471. In Figure 40 the chromophore binding pocket is shown with the above-mentioned histidine and tyrosine residues highlighted. The role of the tyrosine residues concerning the photo-conversion their involvement in the hydrogen-bond network can also be addressed with HY-labelled Cph1 Δ 2. The protein sequence contains 18 histidine and 13 tyrosine residues, which is reasonably sparse.

The application of NMR, in comparison to other spectroscopic methods, provides the opportunity to detect protons directly. Proton relocation processes can be monitored over time and chemical exchange reactions with water molecules observed by ^1H - ^1H exchange spectroscopy (146–148). Proton-detected experiments are accompanied by an improved spectral quality, i.e. a better resolution and an increased sensitivity. Using proton-detected ultrafast (100 kHz) MAS NMR experiments, hydrogen contacts between chromophore and protein residues can be observed directly and monitored during photo-conversion. Information about the hydrogen-bond network of the chromophore binding pocket and the pyrrole water in both, the inactive and active state, will help to understand the molecular mechanism of phytochrome photoreceptors mode of action.

Bibliography

1. Levitt MH. Spin dynamics: basics of nuclear magnetic resonance. John Wiley & Sons; 2001. 740 p.
2. Keeler J. Understanding NMR Spectroscopy. John Wiley & Sons; 2010. 526 p.
3. Duer M. Introduction to Solid-State NMR Spectroscopy. John Wiley & Sons; 2004. 368 p.
4. Takegoshi K, Nakamura S, Terao T. ^{13}C - ^1H dipolar-assisted rotational resonance in magic-angle spinning NMR. *Chem Phys Lett.* 2001;344(5–6):631–7.
5. Delaglio F, Walker GS, Farley K, Sharma R, Hoch J, Arbogast L, et al. Non-uniform sampling for all: More NMR spectral quality, less measurement time. *Am Pharm Rev.* 2017;20(4).
6. Hyberts SG, Arthanari H, Wagner G. Applications of non-uniform sampling and processing. *Top Curr Chem.* 2012;316:125–48.
7. Hartmann SR, Hahn EL. Nuclear double resonance in the rotating frame. *Physical Review.* 1962;128(5):2042–53.
8. Overhauser AW. Polarization of Nuclei in Metals. *Physical Review.* 1953;4(3):411–5.
9. Lilly Thankamony AS, Wittmann JJ, Kaushik M, Corzilius B. Dynamic nuclear polarization for sensitivity enhancement in modern solid-state NMR. *Prog Nucl Magn Reson Spectrosc.* 2017;102–103:120–95.
10. Liao SY, Lee M, Wang T, Sergeyev I v., Hong M. Efficient DNP NMR of Membrane Proteins: Sample Preparation Protocols, Sensitivity, and Radical Location. *J Biomol NMR.* 2016;64(3):223–37.
11. Andreas LB, Barnes AB, Corzilius B, Chou JJ, Miller EA, Caporini M, et al. Dynamic nuclear polarization study of inhibitor binding to the M2 18–60 proton transporter from influenza A. *Biochemistry.* 2013;52(16):2774–82.
12. Berruyer P, Björgvinsdóttir S, Bertarello A, Stevanato G, Rao Y, Karthikeyan G, et al. Dynamic Nuclear Polarization Enhancement of 200 at 21.15 T Enabled by 65 kHz Magic Angle Spinning. *Journal of Physical Chemistry Letters.* 2020;11(19):8386–91.

-
13. Jagtap AP, Geiger MA, Stöppler D, Orwick-Rydmark M, Oschkinat H, Sigurdsson ST. BcTol: A highly water-soluble biradical for efficient dynamic nuclear polarization of biomolecules. *Chemical Communications*. 2016;52(43):7020–3.
 14. Hall DA, Maus DC, Gerfen GJ, Inati SJ, Becerra LR, Dahlquist FW, et al. Polarization-enhanced NMR spectroscopy of biomolecules in frozen solution. *Science* (1979). 1997;276(5314):930–2.
 15. Kane SN, Mishra A, Dutta AK. Preface: International Conference on Recent Trends in Physics (ICRTP 2016). *J Phys Conf Ser*. 2016;755(1).
 16. Matsuki Y, Idehara T, Fukazawa J, Fujiwara T. Advanced instrumentation for DNP-enhanced MAS NMR for higher magnetic fields and lower temperatures. *Journal of Magnetic Resonance*. 2016;264:107–15.
 17. Hu KN, Song C, Yu HH, Swager TM, Griffin RG. High-frequency dynamic nuclear polarization using biradicals: A multifrequency EPR lineshape analysis. *Journal of Chemical Physics*. 2008;128(5):1–17.
 18. van den Brandt B, Bunyatova EI, Hautle P, Konter JA. DNP with the free radicals deuterated TEMPO and deuterated oxo-TEMPO. *Nucl Instrum Methods Phys Res A*. 2004;526(1-2 SPEC. ISS.):53–5.
 19. Sauvée C, Rosay M, Casano G, Aussenac F, Weber RT, Ouari O, et al. Highly efficient, water-soluble polarizing agents for dynamic nuclear polarization at high frequency. *Angewandte Chemie - International Edition*. 2013;52(41):10858–61.
 20. Corzilius B. Paramagnetic metal ions for dynamic nuclear polarization. *eMagRes*. 2018;7(4):179–94.
 21. Jeffries CD. Polarization Of Nuclei by Resonance Saturation in Paramagnetic Crystals. *Physical Review*. 1957;106(1):164.
 22. Kessenikh A, Manenkov A, Pyatnitskii G. On explanation of experimental data on dynamic polarisation of protons in irradiated polyethylenes. *Soviet Phys-Solid State (English Transl)*. 1964;6.
 23. Wollan DS. Dynamic nuclear polarization with an inhomogeneously broadened ESR line. II. Experiment. *Phys Rev B*. 1976;13(9):3686–96.
 24. Hwang CF, Hill DA. Phenomenological Model for the New Effect In Dynamic Polarisation. *Phys Rev Lett*. 1967;19(18):1–4.
 25. Hwang CF, Hill DA. New Effect in Dynamic Polarisation. *Phys Rev Lett*. 1967;18(4):5–7.

-
26. Wind RA, Duijvestijn MJ, van der Lugt C, Manenschijn A, Vriend J. Applications of dynamic nuclear polarization in ^{13}C NMR in solids. *Prog Nucl Magn Reson Spectrosc.* 1985;17(C):33–67.
 27. Can T V., Caporini MA, Mentink-Vigier F, Corzilius B, Walish JJ, Rosay M, et al. Overhauser effects in insulating solids. *Journal of Chemical Physics.* 2014;141(6):1–8.
 28. Pylaeva S, Ivanov KL, Baldus M, Sebastiani D, Elgabarty H. Molecular Mechanism of Overhauser Dynamic Nuclear Polarization in Insulating Solids. *Journal of Physical Chemistry Letters.* 2017;8(10):2137–42.
 29. Lelli M, Chaudhari SR, Gajan D, Casano G, Rossini AJ, Ouari O, et al. Solid-State Dynamic Nuclear Polarization at 9.4 and 18.8 T from 100 K to Room Temperature. *J Am Chem Soc.* 2015;137(46):14558–61.
 30. Perras FA, Reinig RR, Slowing II, Sadow AD, Pruski M. Effects of biradical deuteration on the performance of DNP: Towards better performing polarizing agents. *Physical Chemistry Chemical Physics.* 2016;18(1):65–9.
 31. Barnes AB, De Paëpe G, Van Der Wel PCA, Hu KN, Joo CG, Bajaj VS, et al. High-field dynamic nuclear polarization for solid and solution biological NMR. *Appl Magn Reson.* 2008;34(3–4):237–63.
 32. Hovav Y, Feintuch A, Vega S. Theoretical aspects of dynamic nuclear polarization in the solid state - The solid effect. *Journal of Magnetic Resonance.* 2010;207(2):176–89.
 33. Hu KN. Polarizing Agents for High-Frequency Dynamic Nuclear Polarization - Development and Applications. Massachusetts Institute Of Technology; 2006.
 34. Corzilius B. High-Field Dynamic Nuclear Polarization. *Annu Rev Phys Chem.* 2020;71(7).
 35. Prisner T, Prandolini MJ. Dynamic Nuclear Polarization (DNP) at High Magnetic Fields. Vol. 128, Multifrequency Electron Paramagnetic Resonance: Theory and Applications. 2011. 161–173 p.
 36. Hu KN, Bajaj VS, Rosay M, Griffin RG. High-frequency dynamic nuclear polarization using mixtures of TEMPO and trityl radicals. *Journal of Chemical Physics.* 2007;126(4).

-
37. Hediger S, Lee D, Mentink-Vigier F, de Paëpe G. MAS-DNP enhancements: Hyperpolarization, depolarization, and absolute sensitivity. Vol. 7, eMagRes. 2018. 105–116 p.
 38. Mentink-Vigier F, Akbey Ü, Oschkinat H, Vega S, Feintuch A. Theoretical aspects of Magic Angle Spinning - Dynamic Nuclear Polarization. *Journal of Magnetic Resonance*. 2015;258:102–20.
 39. Mentink-Vigier F, Paul S, Lee D, Feintuch A, Hediger S, Vega S, et al. Nuclear depolarization and absolute sensitivity in magic-angle spinning cross effect dynamic nuclear polarization. *Physical Chemistry Chemical Physics*. 2015;17(34):21824–36.
 40. Bertini I, Luchinat C, Parigi G, Ravera E. SedNMR: On the edge between solution and solid-state NMR. *Acc Chem Res*. 2013;46(9):2059–69.
 41. Bertini I, Engelke F, Luchinat C, Parigi G, Ravera E, Rosa C, et al. NMR properties of sedimented solutes. *Physical Chemistry Chemical Physics*. 2012;14(2):439–47.
 42. Bertini I, Luchinat C, Parigi G, Ravera E, Reif B, Turano P. Solid-state NMR of proteins sedimented by ultracentrifugation. *Proc Natl Acad Sci USA*. 2011;108(26):10396–9.
 43. Wiegand T, Lacabanne D, Torosyan A, Boudet J, Cadalbert R, Allain FHT, et al. Sedimentation Yields Long-Term Stable Protein Samples as Shown by Solid-State NMR. *Front Mol Biosci*. 2020;7(February):1–8.
 44. Chandrasekhar S. Stochastic Problems in Physics and Astronomy. *Rev Mod Phys*. 1943;15(1).
 45. Mereghetti P, Wade RC. Atomic detail brownian dynamics simulations of concentrated protein solutions with a mean field treatment of hydrodynamic interactions. *Journal of Physical Chemistry B*. 2012;116(29):8523–33.
 46. Bain AD. Chemical exchange in NMR. *Prog Nucl Magn Reson Spectrosc*. 2003;43(3–4):63–103.
 47. Dhiel P, Fluck E, Kosfeld R. Dynamic NMR spectroscopy In *NMR, Grundlagen und Fortschritte*. 15th ed. Berlin, Heidelberg, New York; 1978. 214 p.
 48. Bányai I. Dynamic NMR for coordination chemistry. *New Journal of Chemistry*. 2018;42(10):7569–81.

-
49. Hasselbalch K. Die Berechnung der Wasserstoffzahl des Blutes aus der freien und gebundenen Kohlensäure desselben, und die Sauerstoffbindung des Blutes als Funktion der Wasserstoffzahl. *Biochem Z.* 1916;78:112–44.
 50. Reijenga J, van Hoof A, van Loon A, Teunissen B. Development of methods for the determination of pKa values. *Anal Chem Insights.* 2013;8(1):53–71.
 51. Bezençon J, Wittwer MB, Cutting B, Smieško M, Wagner B, Kansy M, et al. PKa determination by ¹H NMR spectroscopy - An old methodology revisited. *J Pharm Biomed Anal.* 2014;93:147–55.
 52. Farrell D, Miranda ES, Webb H, Georgi N, Crowley PB, McIntosh LP, et al. Titration DB: Storage and analysis of NMR-monitored protein pH titration curves. *Proteins: Structure, Function and Bioinformatics.* 2010;78(4):843–57.
 53. Castañeda CA, Fitch CA, Majumdar A, Khangulov V, Schlessman JL, García-Moreno BE. Molecular determinants of the pKa values of Asp and Glu residues in staphylococcal nuclease. *Proteins: Structure, Function and Bioinformatics.* 2009;77(3):570–88.
 54. Webb H, Tynan-Connolly BM, Lee GM, Farrell D, O'Meara F, Søndergaard CR, et al. Remeasuring HEWL pKa values by NMR spectroscopy: Methods, analysis, accuracy, and implications for theoretical pKa calculations. *Proteins: Structure, Function and Bioinformatics.* 2011;79(3):685–702.
 55. Onufriev A, Case DA, Ullmann GM. A novel view of pH titration in biomolecules. *Biochemistry.* 2001;40(12):3413–9.
 56. Pace CN, Fu H, Fryar KL, Landua J, Trevino SR, Schell D, et al. Contribution of hydrogen bonds to protein stability. *Protein Science.* 2014;23(5):652–61.
 57. Englander SW, Kallenbach NR. Hydrogen exchange and structural dynamics of proteins and nucleic acids. *Q Rev Biophys.* 1983;16(4):521–655.
 58. Girame H, Garcia-Borràs M, Feixas F. Changes in Protonation States of In-Pathway Residues can Alter Ligand Binding Pathways Obtained From Spontaneous Binding Molecular Dynamics Simulations. *Front Mol Biosci.* 2022;9:922361.

-
59. Dastvan R, Fischer AW, Mishra S, Meiler J, McHaourab HS. Protonation-dependent conformational dynamics of the multidrug transporter EmrE. *Proc Natl Acad Sci USA*. 2016;113(5):1220–5.
 60. Schönichen A, Webb BA, Jacobson MP, Barber DL. Considering protonation as a posttranslational modification regulating protein structure and function. *Annu Rev Biophys*. 2013;42(1):289–314.
 61. Johnson MP. Photosynthesis. *Essays Biochem*. 2016;60(3):255–73.
 62. Barber J. A mechanism for water splitting and oxygen production in photosynthesis. *Nat Plants*. 2017;3(April):1–5.
 63. Bricker TM, Roose JL, Fagerlund RD, Frankel LK, Eaton-Rye JJ. The extrinsic proteins of Photosystem II. *BBA - Bioenergetics*. 2012;1817:121–42.
 64. Bommer M, Bondar AN, Zouni A, Dobbek H, Dau H. Crystallographic and Computational Analysis of the Barrel Part of the PsbO Protein of Photosystem II: Carboxylate-Water Clusters as Putative Proton Transfer Relays and Structural Switches. *Biochemistry*. 2016;55(33):4626–4635
 65. Gabdulkhakov A, Guskov A, Broser M, Kern J, Müh F, Saenger W, et al. Probing the Accessibility of the Mn₄Ca Cluster in Photosystem II: Channels Calculation, Noble Gas Derivatization, and Cocrystallization with DMSO. *Structure*. 2009;17(9):1223–34.
 66. de Grotthuss CJT. Sur la décomposition de l'eau et des corps qu'elle tient en dissolution a l'aide de l'électricité galvanique. *Ann Chim (Paris)*. 1806;(58):54–73.
 67. Zaharieva I, Wichmann JM, Dau H. Thermodynamic limitations of photosynthetic water oxidation at high proton concentrations. *Journal of Biological Chemistry*. 2011;286(20):18222–8.
 68. Zaks J, Amarnath K, Sylak-Glassman EJ, Fleming GR. Models and measurements of energy-dependent quenching. *Photosynth Res*. 2013;116(2–3):389–409.
 69. Müller P, Li XP, Niyogi KK. Non-photochemical quenching. A response to excess light energy. *Plant Physiol*. 2001;125(4):1558–66.
 70. Müller P, Li XP, Niyogi KK. Non-photochemical quenching. A response to excess light energy. *Plant Physiol*. 2001;125(4):1558–66.

-
71. Ruban A v. Nonphotochemical chlorophyll fluorescence quenching: Mechanism and effectiveness in protecting plants from photodamage. *Plant Physiol.* 2016;170(4):1903–16.
 72. Shutova T, Klimov V V., Andersson B, Samuelsson G. A cluster of carboxylic groups in PsbO protein is involved in proton transfer from the water oxidizing complex of Photosystem II. *Biochim Biophys Acta Bioenerg.* 2007;1767(6):434–40.
 73. De Las Rivas J, Barber J. Analysis of the structure of the PsbO protein and its implications. *Photosynth Res.* 2004;81(3):329–43.
 74. Bondar AN, Dau H. Extended protein/water H-bond networks in photosynthetic water oxidation. *Biochim Biophys Acta Bioenerg.* 2012;1817(8):1177–90.
 75. del Val C, Bondar AN. Charged groups at binding interfaces of the PsbO subunit of photosystem II: A combined bioinformatics and simulation study. *Biochimica et Biophysica Acta (BBA) - Bioenergetics.* 2017;1858(6):432–41.
 76. Pardi SA, Nusinow DA. Out of the Dark and Into the Light: A New View of Phytochrome Photobodies. *Front Plant Sci.* 2021;12(August):1–15.
 77. Sharrock RA. The phytochrome red/far-red photoreceptor superfamily. *Genome Biol.* 2008;9(8).
 78. Song C, Psakis G, Lang C, Mailliet J, Gärtner W, Hughes J, et al. Two ground state isoforms and a chromophore D-ring photoflip triggering extensive intramolecular changes in a canonical phytochrome. *PNAS.* 2011;108(10):3842–7.
 79. Ulijasz AT, Cornilescu G, Cornilescu CC, Zhang J, Markley JL, Vierstra RD. Structural basis for the photoconversion of a phytochrome to the far-red light-absorbing form. *Nature.* 2010;463(7278):250–4.
 80. Yeh KC, Wu SH, Murphy JT, Lagarias JC. A cyanobacterial phytochrome two-component light sensory system. *Science (1979).* 1997;277(5331):1505–8.
 81. Nagano S. From photon to signal in phytochromes: similarities and differences between prokaryotic and plant phytochromes. *J Plant Res.* 2016;129(2):123–35.

-
82. Legris M, Ince YÇ, Fankhauser C. Molecular mechanisms underlying phytochrome-controlled morphogenesis in plants. *Nat Commun.* 2019;10(1).
 83. Bongards C, Gärtner W. The role of the chromophore in the biological photoreceptor phytochrome: An approach using chemically synthesized tetrapyrroles. *Acc Chem Res.* 2010;43(4):485–95.
 84. Escobar FV, von Stetten D, Günther-Lütken M, Keidel A, Michael N, Lamparter T, et al. Conformational heterogeneity of the Pfr chromophore in plant and cyanobacterial phytochromes. *Front Mol Biosci.* 2015;2(JUL):1–13.
 85. Rockwell NC, Su YS, Lagarias JC. Phytochrome structure and signaling mechanisms. *Annu Rev Plant Biol.* 2006;57(26):837–58.
 86. Burgie ES, Vierstra RD. Phytochromes: An atomic perspective on photoactivation and signaling. *Plant Cell.* 2014;26(12):568–4583.
 87. Ahmad M, Jarillo JA, Smirnova O, Cashmore AR. The CRY1 blue light photoreceptor of *Arabidopsis* interacts with phytochrome a in vitro. *Mol Cell.* 1998;1(7).
 88. Yeh KC, Lagarias JC. Eukaryotic phytochromes: Light-regulated serine/threonine protein kinases with histidine kinase ancestry. *Proc Natl Acad Sci U S A.* 1998;95(23):13976–81.
 89. Essen LO, Mailliet J, Hughes J. The structure of a complete phytochrome sensory module in the Pr ground state. *PNAS.* 2008;105(38):14709–14.
 90. Oka Y, Matsushita T, Mochizuki N, Suzuki T, Tokutomi S, Nagatani A. Functional analysis of a 450-amino acid N-terminal fragment of phytochrome B in *Arabidopsis*. *Plant Cell.* 2004;16(8):2104–16.
 91. Takala H, Björling A, Berntsson O, Lehtivuori H, Niebling S, Hoernke M, et al. Signal amplification and transduction in phytochrome photosensors. *Nature.* 2014;509(7499):245–8.
 92. Rüdiger W, Thümmler F, Cmiel E, Schneider S. Chromophore structure of the physiologically active form (Pfr) of phytochrome. *PNAS.* 1983;80(20):6244–8.
 93. Sivaprakasam S, Mani V, Balasubramanian N, Abraham DR. Cyanobacterial Phytochromes in Optogenetics. In: Anwar M, Farooq Z, Rather RA, Tauseef M, Heinbockel T, editors. *Epigenetics to Optogenetics - A New Paradigm in the Study of Biology.* London; 2021.

-
94. Chernov KG, Redchuk TA, Omelina ES, Verkhusha V v. Near-Infrared Fluorescent Proteins, Biosensors, and Optogenetic Tools Engineered from Phytochromes. *Chem Rev.* 2017;117(9):6423–46.
 95. Strauss HM, Hughes J, Schmieder P. Heteronuclear solution-state NMR studies of the chromophore in cyanobacterial phytochrome Cph1. *Biochemistry.* 2005;44(23):8244–50.
 96. Song C, Essen LO, Gärtner W, Hughes J, Matysik J. Solid-state NMR spectroscopic study of chromophore-protein interactions in the Pr ground state of plant phytochrome A. *Mol Plant.* 2012;5(3):698–715.
 97. Stöppler D, Song C, van Rossum BJ, Geiger MA, Lang C, Mroginiski MA, et al. Dynamic Nuclear Polarization Provides New Insights into Chromophore Structure in Phytochrome Photoreceptors. *Angewandte Chemie - International Edition.* 2016;55(52):16017–20.
 98. Anders K, Daminelli-Widany G, Mroginiski MA, von Stetten D, Essen LO. Structure of the cyanobacterial phytochrome 2 photosensor implies a tryptophan switch for phytochrome signaling. *Journal of Biological Chemistry.* 2013;288(50):35714–25.
 99. Velázquez Escobar F, Buhrke D, Michael N, Sauthof L, Wilkening S, Tavraz NN, et al. Common Structural Elements in the Chromophore Binding Pocket of the Pfr State of Bathy Phytochromes. *Photochem Photobiol.* 2017;93(3):724–32.
 100. Yang X, Kuk J, Moffat K. Crystal structure of *Pseudomonas aeruginosa* bacteriophytochrome: Photoconversion and signal transduction. *PNAS.* 2008;105(38):14715–20.
 101. Bellini D, Papiz MZ. Structure of a bacteriophytochrome and light-stimulated protomer swapping with a gene repressor. *Structure.* 2012;20(8):1436–46.
 102. Marley J, Lu M, Bracken C. A method for efficient isotopic labeling of recombinant proteins. *J Biomol NMR.* 2001;20(1):71–5.
 103. Olsson MHM, SØndergaard CR, Rostkowski M, Jensen JH. PROPKA3: Consistent treatment of internal and surface residues in empirical pK_a predictions. *J Chem Theory Comput.* 2011;7(2):525–37.
 104. SØndergaard CR, Olsson MHM, Rostkowski M, Jensen JH. Improved treatment of ligands and coupling effects in empirical calculation and rationalization of pK_a values. *J Chem Theory Comput.* 2011;7(7):2284–95.

-
105. Awoonor-Williams E, Rowley CN. Evaluation of Methods for the Calculation of the pKa of Cysteine Residues in Proteins. *J Chem Theory Comput.* 2016;12(9):4662–73.
 106. Dolinsky TJ, Nielsen JE, McCammon JA, Baker NA. PDB2PQR: An automated pipeline for the setup of Poisson-Boltzmann electrostatics calculations. *Nucleic Acids Res.* 2004;32(WEB SERVER ISS.):665–7.
 107. Williamson MP. Using chemical shift perturbation to characterise ligand binding. *Prog Nucl Magn Reson Spectrosc.* 2013;73:1–16.
 108. Thurber KR, Tycko R. Measurement of sample temperatures under magic-angle spinning from the chemical shift and spin-lattice relaxation rate of ^{79}Br in KBr powder. *J Magn Reson.* 2009;196(1):84–7.
 109. Ernst RR, Bodenhausen G, Wokaun A. Principles of Nuclear Magnetic Resonance in One and Two Dimensions. London/New York: Oxford Univ. Press; 1987. 610pp p.
 110. Mentink-Vigier F, Dubroca T, van Tol J, Sigurdsson ST. The distance between g-tensors of nitroxide biradicals governs MAS-DNP performance: The case of the bTurea family. *Journal of Magnetic Resonance.* 2021;329.:107026
 111. Lund A, Casano G, Menzildjian G, Kaushik M, Stevanato G, Yulikov M, et al. TinyPols: A family of water-soluble binitroxides tailored for dynamic nuclear polarization enhanced NMR spectroscopy at 18.8 and 21.1 T. *Chem Sci.* 2020;11(10):2810–8.
 112. Chevelkov V, Shi C, Fasshuber HK, Becker S, Lange A. Efficient band-selective homonuclear CO-CA cross-polarization in protonated proteins. *J Biomol NMR.* 2013;56(4):303–11.
 113. Baldus M, Petkova AT, Herzfeld J, Griffin, Robert G. Cross polarization in the tilted frame: assignment and spectral simplification in heteronuclear spin systems. *Mol Phys.* 1998;95(6):1197–207.
 114. Verel R, Ernst M, Meier BH. Adiabatic dipolar recoupling in solid-state NMR: The DREAM scheme. *Journal of Magnetic Resonance.* 2001;150(1):81–99.
 115. Vranken WF, Boucher W, Stevens TJ, Fogh RH, Pajon A, Llinas M, et al. The CCPN data model for NMR spectroscopy: Development of a software pipeline. *Proteins: Structure, Function and Genetics.* 2005;59(4):687–96.

-
116. Cadars S, Sein J, Duma L, Lesage A, Pham TN, Baltisberger JH, et al. The refocused INADEQUATE MAS NMR experiment in multiple spin-systems: Interpreting observed correlation peaks and optimising lineshapes. *Journal of Magnetic Resonance*. 2007;188(1):24–34.
 117. Hohwy M, Rienstra CM, Jaroniec CP, Griffin RG. Fivefold symmetric homonuclear dipolar recoupling in rotating solids: Application to double quantum spectroscopy. *Journal of Chemical Physics*. 1999;110(16):7983–92.
 118. Thurlkill RL, Grimsley GR, Scholtz JM, Pace CN. pK values of the ionizable groups of proteins. *Protein Science*. 2006;15(5):1214–8.
 119. Hellmich J, Bommer M, Burkhardt A, Ibrahim M, Kern J, Meents A, et al. Native-like Photosystem II Superstructure at 2.44 Å Resolution through Detergent Extraction from the Protein Crystal. *Structure*. 2014;22(11):1607–15.
 120. Loll B, Kern J, Saenger W, Zouni A, Biesiadka J. Towards complete cofactor arrangement in the 3.0 Å resolution structure of photosystem II. *Nature*. 2005;438(7070):1040–4.
 121. Nagao R, Ueoka-Nakanishi H, Noguchi T. D1-Asn-298 in photosystem II is involved in a hydrogen-bond network near the redox-active tyrosine YZ for proton exit during water oxidation. *Journal of Biological Chemistry*. 2017;292(49):20046–57.
 122. Isaksson L, Gustavsson E, Persson C, Brath U, Vrhovac L, Karlsson G, et al. Signaling Mechanism of Phytochromes in Solution. *Structure*. 2021;29(2):151–60.
 123. Gustavsson E, Isaksson L, Persson C, Mayzel M, Brath U, Vrhovac L, et al. Modulation of Structural Heterogeneity Controls Phytochrome Photoswitching. *Biophys J*. 2020;118(2):415–21.
 124. Vugmeyster L, Ostrovsky D, Ford JJ, Lipton AS. Freezing of dynamics of a methyl group in a protein hydrophobic core at cryogenic temperatures by deuterium NMR spectroscopy. *J Am Chem Soc*. 2010;132(12):4038–9.
 125. Rohmer T, Strauss H, Hughes J, de Groot H, Gartner W, Schmieder P, et al. ¹⁵N MAS NMR studies of Cph1 phytochrome: Chromophore dynamics and intramolecular signal transduction. *Journal of Physical Chemistry B*. 2006;110(41):20580–5.

-
126. Spillane KM, Dasgupta J, Lagarias JC, Mathies RA. Homogeneity of Phytochrome Cph1 Δ Vibronic Absorption Revealed by Resonance Raman Intensity Analysis. *J Am Chem Soc.* 2009;131(17):13946–13948.
 127. Rydzewski J, Walczewska-Szewc K, Czach S, Nowak W, Kuczera K. Enhancing the Inhomogeneous Photodynamics of Canonical Bacteriophytochrome. *Journal of Physical Chemistry B.* 2022;126(14):2647–57.
 128. Kim PW, Rockwell NC, Martin SS, Lagarias JC, Larsen DS. Dynamic inhomogeneity in the photodynamics of cyanobacterial phytochrome cph1. *Biochemistry.* 2014;53(17):2818–26.
 129. Rohmer T, Lang C, Hughes J, Essen LO, Gärtner W, Matysik J. Light-induced chromophore activity and signal transduction in phytochromes observed by¹³C and¹⁵N magic-angle spinning NMR. *Proc Natl Acad Sci USA.* 2008;105(40):15229–34.
 130. Perras FA, Sadow AD, Pruski M. In Silico Design of DNP Polarizing Agents: Can Current Dinitroxides be Improved? *ChemPhysChem.* 2017;Aug 18;18(16)2279-2287.
 131. Hu KN, Song C, Yu HH, Swager TM, Griffin RG. High-frequency dynamic nuclear polarization using biradicals: A multifrequency EPR lineshape analysis. *Journal of Chemical Physics.* 2008;128(5).
 132. Mentink-Vigier F, Vega S, de Paëpe G. Fast and accurate MAS-DNP simulations of large spin ensembles. *Physical Chemistry Chemical Physics.* 2017;19(5):3506–22.
 133. Maly T, Miller AF, Griffin RG. In situ high-field dynamic nuclear polarization-direct and indirect polarization of ¹³C nuclei. *ChemPhysChem.* 2010;11(5):999–1001.
 134. Leavesley A, Jain S, Kamniker I, Zhang H, Rajca S, Andrzej R, et al. Maximizing NMR signal per unit time by facilitating the e-e-n cross effect DNP rate. *Phys Chem Chem Phys.* 2018;176(20):139–48.
 135. Claesson E, Wahlgren WY, Takala H, Pandey S, Castillon L, Kuznetsova V, et al. The primary structural photoresponse of phytochrome proteins captured by a femtosecond x-ray laser. *Elife.* 2020;9:1–18.
 136. Takala H, Edlund P, Ihalainen JA, Westenhoff S. Tips and turns of bacteriophytochrome photoactivation. *Photochemical and Photobiological Sciences.* 2020;19(11):1488–510.

-
137. Yang X, Stojković EA, Kuk J, Moffat K. Crystal structure of the chromophore binding domain of an unusual bacteriophytochrome, RpBphP3, reveals residues that modulate photoconversion. *Proc Natl Acad Sci USA*. 2007;104(30):12571–6.
 138. Li F, Burgie ES, Yu T, Héroux A, Schatz GC, Vierstra RD, et al. X-ray radiation induces deprotonation of the bilin chromophore in crystalline D. Radiodurans phytochrome. *J Am Chem Soc*. 2015;137(8):2792–5.
 139. Zhang H, Neal S, Wishart DS. RefDB: A database of uniformly referenced protein chemical shifts. *J Biomol NMR*. 2003;25(3):173–95.
 140. Ulrich EL, Akutsu H, Doreleijers JF, Harano Y, Ioannidis YE, Lin J, et al. BioMagResBank. *Nucleic Acids Res*. 2008;36:D402–8.
 141. Lee W, Markley JL. PACSY database, a relational database management system for Protein structure and nuclear Magnetic Resonance chemical shift analysis. *Proceedings - 2012 IEEE International Conference on Bioinformatics and Biomedicine Workshops, BIBMW 2012*. 2012;930–2.
 142. Yang J, Yan R, Roy A, Xu D, Poisson J, Zhang Y. The I-TASSER suite: Protein structure and function prediction. *Nat Methods*. 2014;12(1):7–8.
 143. Lewandowski JR, de Paëpe G, Eddy MT, Griffin RG. ¹⁵N- ¹⁵N proton assisted recoupling in magic angle spinning NMR. *J Am Chem Soc*. 2009;131(16):5769–76.
 144. Burgie ES, Zhang J, Vierstra RD. Crystal Structure of Deinococcus Phytochrome in the Photoactivated State Reveals a Cascade of Structural Rearrangements during Photoconversion. *Structure*. 2016;24(3):448–57.
 145. Carrillo M, Pandey S, Sanchez J, Noda M, Poudyal I, Aldama L, et al. High-resolution crystal structures of transient intermediates in the phytochrome photocycle. *Structure*. 2021;29(7):743-754.
 146. Friedrich D, Brüning FN, Nieuwkoop AJ, Netz RR, Hegemann P, Oschkinat H. Collective exchange processes reveal an active site proton cage in bacteriorhodopsin. *Commun Biol*. 2020;3(1):1–9.
 147. Aluas M, Tripon C, Griffin JM, Filip X, Ladizhansky V, Griffin RG, et al. CHHC and ¹H-¹H magnetization exchange: Analysis by experimental solid-state NMR and 11-spin density-matrix simulations. *Journal of Magnetic Resonance*. 2009;199(2):173–87.
 148. Brown SP, Lesage A, Benedicte E, Emsley L. Probing Proton-Proton Proximities in the Solid State: High-Resolution Two dimensional ¹H-¹H

Double Quantum CRAMPS NMR Spectroscopy. *J. Am. Chem. Soc.* 2004;(126):13230–13231.

List of publications

Gerland, L.; Friedrich, D.; Hopf, L.; Donovan, E.J.; Wallmann, A.; Erdmann, N.; Diehl, A.; Bommer, M.; Buzar, K.; Ibrahim, M.; Schmieder, P.; Dobbek, H.; Zouni, A.; Bondar, A.-N.; Dau, H.; Oschkinat, H.; pH-Dependent Protonation of Surface Carboxylate Groups in PsbO Enables Local Buffering and Triggers Structural Changes. *ChemBioChem* **2020**, 21, 1597-1604